Design and Synthesis of Ion-Conducting Covalent Organic Frameworks

TAO Shanshan

Doctor of Philosophy

Department of Structural Molecular Science

School of Physical Sciences

SOKENDAI (The Graduate University for Advanced Studies)

June 2017

CONTENTS

Chapter 1

General Introduction

1.1 Covalent Organic Frameworks

Chemistry is a central science that enables the design and synthesis of new molecules and elucidates molecular origins of various physicochemical properties and functions at different structural levels.

Crystalline polymers are a class of unique materials that have ordered structures and could serve as a molecular platform for exploring new properties and functions. Organic polymers linked by covalent bonds hardly achieve simultaneously the precisely ordered primary and high-order structures; this situation marks a sharp contrast to biological polymers with well-defined primary and high-order structures.[1-4] Despite the fact of a great progress in polymer chemistry over the past decades, synthetic organic polymers are still difficult to be designed and synthesized with orderings at both primary and high-order structural levels.[5]

Covalent organic frameworks (COFs) are a class of fully pre-designable polymer in which the skeleton can be designed using a topology diagram. This design principle is totally different from those of linear polymers, hyper-branched polymers, cross-linked polymers and biopolymers, increasing the ability of designing both primary and high-order structures. Moreover, COFs generate confined molecular space and interface that control the interplays with photons, excitons, electrons, holes, spins, and molecules, offering a unique molecular system for structural design and functional development. Progress in COFs has continuously raised the freedom of molecular design and has shifted the research focus from structural design to functional design in recent years.

1.1.1 Design and Synthesis

1.1.1.1 Reversible covalent reactions

Synthetic polymers are usually prepared by kinetic reactions in which the covalent bonds are formed via irreversible reactions. Different from the conventional covalent bonds, reversible reaction contains error-checking and proof-reading properties can result in well-defined structures (Figure 1).[6] By introducing the reversible covalent bonding systems to the synthesis of covalent porous networks, the reaction system has

the chance of producing crystalline polymers. At the same time, the self-healing process greatly decreases the occurrence of structural defects and enhances the structural homogeneity. As a result, the porous polymers constitute long-range ordered structures and own excellent thermodynamic stability. These basic concepts offer the chemical basis of designing COFs.

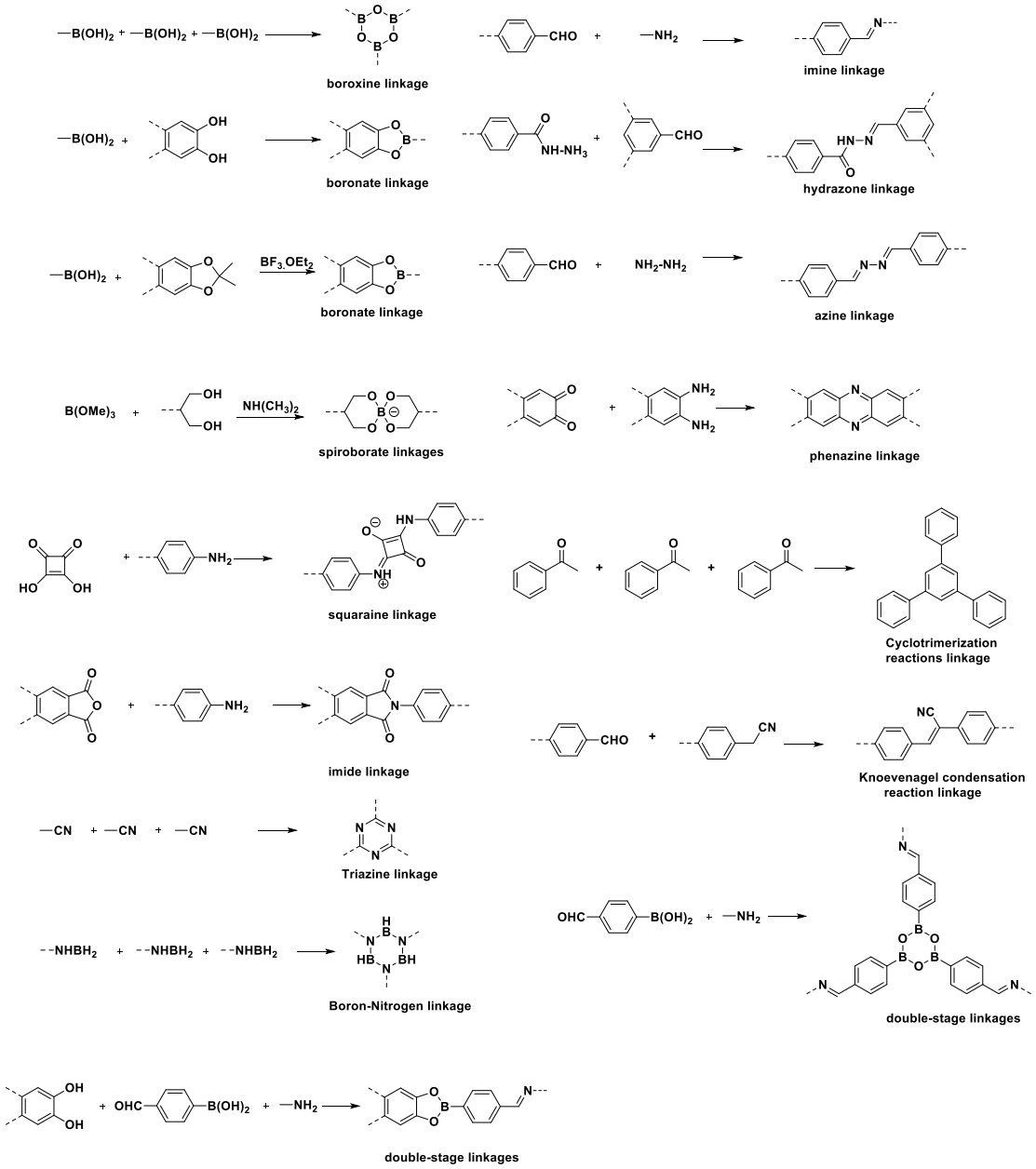

Figure 1. Chemical reactions used to synthesize COFs.

1.1.1.2 Structure Diversity of Building Blocks

COFs can be designed by using reticular chemistry based on topology diagrams; this design principle enables the generation of different skeletons and pores and offers the basis of their structural diversity. In the topology diagram, the geometry matching of monomers is essential (Figure 2). The building blocks usually have π-backbones and rigid conformation to assume topology-directed bond formation and maintain the 2D planarity of the extended polygons. Indeed, besides geometry, monomers have been explored to show a broad diversity of structures, including different sizes, docking sites, reactive groups, chiral centers, and redox-active, catalytic, and photoactive groups. Since the structural diversity is highly relied on the availability of monomers, 3D COFs have less structural diversity that is limited by the availability of T_d-symmetric nodes. Nevertheless, 3D COFs are unique because they have a great potential for expanding their library by developing various π-units as linkers for the condensation with the T_d-symmetric monomers.

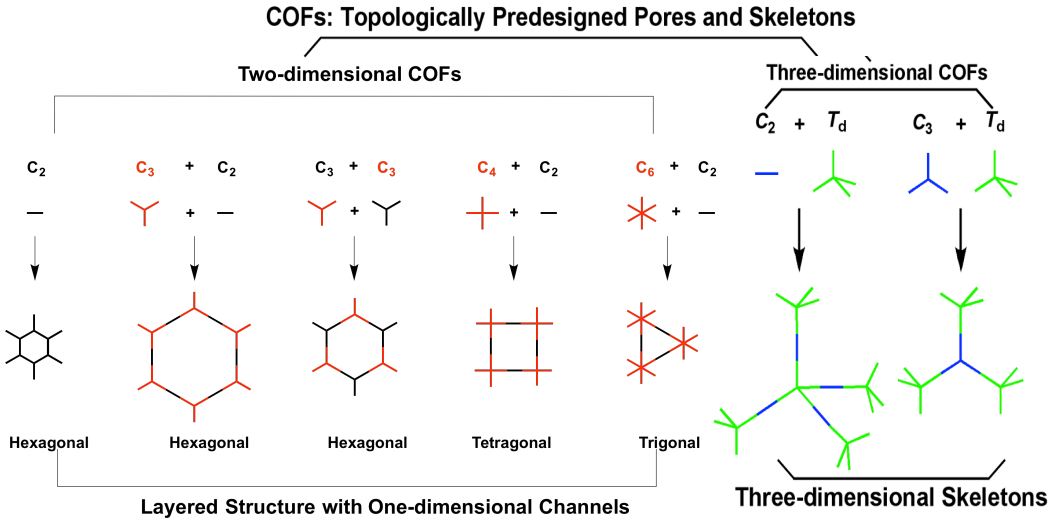

Figure 2. Design principle of COFs based on different topology diagrams.

As shown in Figure 2, the structure of COFs is determined by geometry of the building blocks. Thus, the combinations, such as $T_d + T_d$, $T_d + C_2$, or $T_d + C_3$, would yield different 3D COFs. Equally, the combinations of 2D blocks, such as $C_2 + C_3$, $C_3 + C_3$ or $C_2 + C_4$ can produce 2D COFs with desired skeletons and pores.

Figure 3 shows the typical structures of organic building blocks with backbones and reactive units. The monomer skeleton ranges from benzene to simple arenes, heterocycles, and macrocycles and can be designed to have different geometries from C_2 to C_3, C_4, C_6, and T_d. Over hundreds of different monomers have been designed and synthesized up to date.

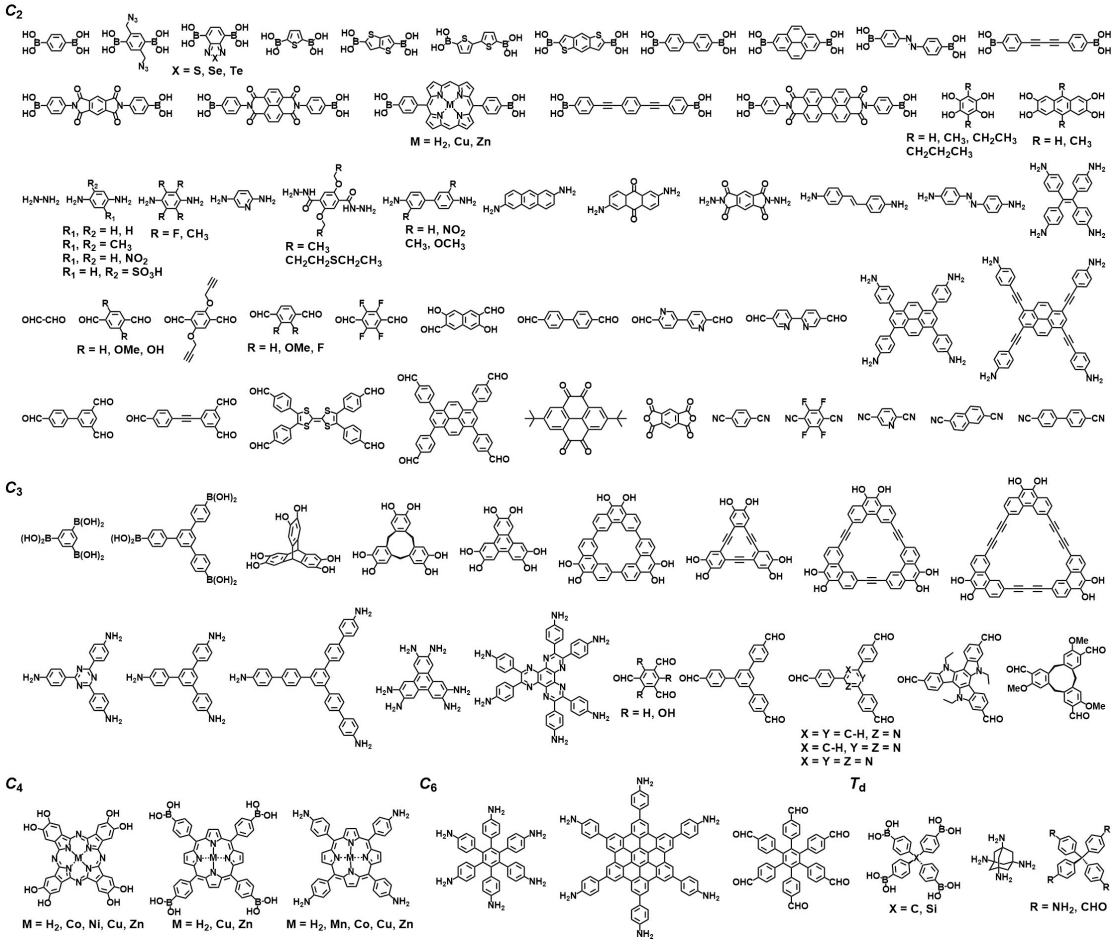

Figure 3. Typical C_2, C_3, C_4, C_6, and T_d-symmetric building blocks with different backbones and reactive units.

1.1.1.3 Synthetic Methods

Synthesis of organic compounds usually requires to control kinetic reactions to form chemical bonds.[7] In contrast, reversible reaction is benefit for correcting structural errors and has a chance of forming ordered structures.[8] Especially, in the polycondensation systems, reversible reactions can generate thermodynamically stable polymer structures.[9] For COFs, the topology design diagram connects the

organic units by covalent bonds in an ordered and predesigned fashion. Moreover, to obtain extended polygon structures, the reactions occur at multiple reactive sites. These characteristics require the use of reversible covalent bond formation reactions for the synthesis of COFs.[10,11,24]

1.1.1.3.1 Solvothermal Synthesis

Most COFs were synthesized under solvothermal environment in which reaction conditions have to be tuned according to the solubility and reactivity of building blocks and the reversibility of the reactions. Especially, the reaction time, temperature, the solvents, and the catalytic concentration were also the most important factors in the solvothermal route to successfully prepare crystalline porous COFs. In a typical solvothermal synthesis, the monomers, solvents, and catalyst were mixed in a Pyrex tube with suitable size. The mixture was sonicated for a few seconds, degased via freeze-pump-thaw cycles, sealed with gas burner and kept at suitable temperature for a certain period. After a certain reaction period, the system was cooled down. The precipitate was collected and washed with appropriate solvents or by Soxhlet extraction. The product was dried under vacuum and kept under suitable conditions. By using this solvothermal method, some COFs could be prepared in large scales. For example, TPT-COF-1 has been prepared in a gram scale from the polycondensation reaction of TPT-NH_2 and TPT-CHO.[12]

1.1.1.3.2 Microwave Synthesis

Solvothermal reactions usually require long reaction period to obtain crystalline porous structures. In this sense, microwave method is unique because it can prompt the synthesis of certain COFs. Up to now, microwave method has been successfully used for the preparation of boronate-ester linked COF-5, COF-102,[13,14] and imine-linked TpPa-COF,[15] Besides, three covalent triazine frameworks, CTFs (P1M, P2M and P4M) have been prepared by using microwave method.[16] This general method is shown below. Monomers in a suitable solvent were sealed in a microwave tube under nitrogen and the resulting mixture was heated with stirring at a designated temperature; then the following treatment was the same as that of solvothermal

method. The microwave route shows the advantages over the solvothermal method the resulting COFs usually have a high porosity.

1.1.1.3.3 Ionothermal Synthesis

For constructing triazine-linked frameworks, many different monomers are available; but most frameworks are amorphous. As special examples, CTF-1 and CTF-2, prepared by ionothermal conditions are crystalline porous materials.[17,18] The monomer and $ZnCl_2$ were degassed, sealed in an ampoule and kept at 400 °C for a certain period. After the mixture was cooled down, it was ground, washed with water and stirred in a diluted HCl solution. Recently, CTF-1 has also been prepared by using a strong acid such as *p*-toluenesulfonic acid as a catalyst under microwave conditions.[16]

1.1.1.3.4 Mechanochemical Synthesis

Solvothermal and microwave reactions require complicated experimental devices; a simple synthetic method is helpful. In this sense, mechanochemical synthesis could overcome these setup limitations. As a general method, the monomers were mixed in a mortar and ground for a certain period to yield COFs.[19,20,25] To enhance the full possibility of this method, a liquid-assisted mechanochemical method has been developed. During the ground process, adding a small amount of catalyst solution to the mortar could enhance the reaction rate through accelerating the homogeneity of reactants. This method could also improve the crystallinity of the COFs in some cases.[21,22,23,26]

1.1.2 Structural Study

Unlike 3D COFs with limited members,[27-30] 2D COFs can be designed by using a variety of different topologies; both regular (conventional topologies) and irregular (unconventional topologies) polygon skeletons have been developed for the design of COFs. In each case, the lattice structure is highly ordered and the pore is discrete. The topological diversity provides the basis of structural diversity of 2D COFs. Behind each topology, huge members of different COFs have been designed and synthesized.

Topology diagram enables different combinations of monomers to design COFs with different skeletons and pores, imparting different structural orderings to the

frameworks.[31-33,34] For example, the scheme of $C_3 + C_2$ yields hexagonal COFs, whereas those $C_2 + C_2 + C_2$ and $C_3 + C_3$ diagrams also form hexagonal COFs but they have different structural orderings and pore sizes. A desymmetrization of the C_3-symmetric vertices generates COFs with heterogeneous pore structures.[35] Tetragonal COFs have been synthesized by using the $C_4 + C_2$ and $C_4 + C_4$ combinations. Moreover, the topology diagram predesigns the pore size. For example, using $C_2 + C_2 + C_2$ and $C_4 + C_4$ schemes has a possibility of preparing microporous COFs, whereas using $C_3 + C_2$, $C_3 + C_3$ and $C_4 + C_2$ diagrams would yield mesoporous structures. Finally, the topology diagram also controls the π-density of the resulting skeletons. Recently, the development of $C_6 + C_2$ topology diagram opens a way to COFs with the highest density of π-skeletons.[37]

An effective way to multiple-pore COF has been achieved by using desymmetrized vertex.[35] The dissymmetry units bear arms of different lengths; upon condensation with C_2-symmetric edges, these dissymmetric vertices form HP-COF-1 and HP-COF-2 that possess different shape of two hexagonal pores and sizes. As a powerful tool for constructing heterogonous porous structures in one COF skeleton, the multiple-component strategy has been developed.[37] Recently, condensation of the TPE knots with two aldehydes of different lengths at a 1/1 molar ratio leads to the synthesis of two triple-pore COFs.[36]

1.1.3 Functions and Properties

Owing to the topological design ability and synthetically controllability of both skeletons and pores, the properties and functions of COFs can be designed and tuned. In the aspect of porous structures, COFs can be designed and control the pore shape, pore size and pore environment; these porous parameters are important for gas sorption, molecular separation, catalysis, and many other properties. On the other hand, the different combinations of edge, knot, and linkage units enable the construction of a variety of different frameworks with multiple functionalities, ranging from semiconducting to charge separation, energy storage, and energy conversion. Moreover, in many cases, the complementary design of both pores and skeletons provides a broad way to trigger a synergistic effect between skeletons and

pore in order to achieve a specific functionality.[37] In this section, the functions of COFs were summarized.

1.1.3.1 Gas Adsorption and Storage

The high porosity and designable porous structures of COFs make them promising as a pre-designable porous medium for the adsorption of various gases. Adsorption of hydrogen (H_2), methane (CH_4), and ammonia (NH_3) with porous materials is interesting and has been investigated for different COFs. The architecture of porous walls with specific open binding sites is important for NH_3. On the other hand, the skeletons and pore walls of COFs play the same important roles in carbon dioxide (CO_2) adsorption. Besides pure gas adsorption, COFs are capable of designing specific structures for selective adsorption that is important for the separation of gas mixtures. Especially, enhancement of surface area, increment of pore volume, and adjustment of appropriate pore size are facile for COFs, which pave a way to simultaneously improving adsorption capacity and selectivity. Both theoretical simulations and separation experiments suggest that COFs are a novel class of porous media for gas adsorption and separation.[38,39]

1.1.3.1.1 Hydrogen

The hydrogen uptake capacities for 3D COFs was predicted to be 2.5 – 3 times larger than 2D COFs, because of larger free volume and surface area.[40] For instance, 3D COF-102 (Figure 4) has a pore size of 1.2 nm and a surface area 3620 $m^2\ g^{-1}$ and exhibits the highest H_2 adsorption capacity of 72.4 mg g^{-1} (7.24 wt%) at 77 K.[41] By contrast, 2D COF-10 (SBET = 1760 $m^2\ g^{-1}$, pore size = 3.2 nm) exhibits a H_2 adsorption capacity of 39.2 mg g^{-1} (3.92 wt%) under otherwise same conditions. [42]

Interestingly, bowl-shaped cyclotricatechylene (CTC) can serve as the vertices to yield a 2D CTC-COF with an excellent uptake of hydrogen at low pressure.[43] CTC-COF owns a pore size of 2.26 nm, a surface area of 1710 $m^2\ g^{-1}$. The H_2 uptake by CTC-COF at 800 mm Hg and 77 K is 1.12 wt%, which is higher than that of 3D COF-10 and is comparable to those of 3D COF-102/103. Enhanced H_2 uptake ability is attributed to the additional adsorption in the bowl-shaped CTC cavity. Remarkably, a triptycene-knotted 2D TDCOF-5 has a surface area of 2497 $m^2\ g^{-1}$, reaches a

capacity of 1.6 wt% at 1 bar and 77 K. COF-JLU2 has a surface area of 415 m^2 g^{-1} and shows the highest capacity among all the investigated 2D and 3D COFs at 1 bar and 77 K.[44,45]

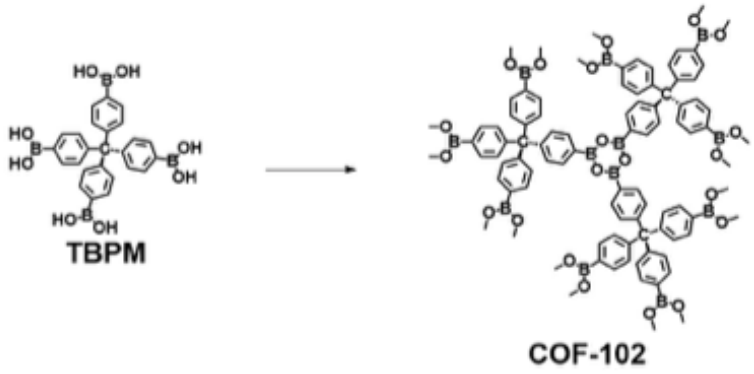

Figure 4. Skeleton design of 3D COFs from the T_d-symmetric building blocks for the boroxine-linked COF-102.

1.1.3.1.2 Methane

3D COFs are superior to 2D COFs with respect to the CH_4 adsorption. The 3D COF-102 and COF-103 exhibited remarkable high-pressure CH_4 uptake capacity of 187 mg g^{-1} (18.7 wt%) and 175 mg g^{-1} (17.5 wt%), respectively, at 35 bar and 298 K, which are the highest among COFs.[46] On the contrary, 2D COF-5 showed a CH_4 uptake capacity of 89 mg g^{-1} (8.9 wt%) under the same conditions, which is the highest among 2D COFs. At low pressure, such as 1 bar, 2D COFs with small pores including ILCOF-1, ACOF-1, and COF-JLU2 exhibited uptake capacity of 0.9, 1.15 and 3.8 wt%, respectively, at 273 K.[47-49]

1.1.3.2 Proton Conduction

Developing materials with high proton conductivity is quite important for fuel cells.[50,51] The pentafluorinated sulfonic acid functionalized polyelectrolyte, Nafion, is a criterion material. Because of its morphology and structure, Nafion has a good conductivity (e.g. 10^{-1} S cm^{-1}) under 98% RH.[52] However, it shows a low efficiency at higher operating temperature (120–200 °C). Thus, designing suitable proton-conducting materials is required for high-temperature fuel cells.

Porous materials possessing inherent pores are attractive for ion conduction across their nanopores. COFs can combine well-defined structure, tunable porosity and functionality, and excellent thermal and chemical stabilities, which are hardly obtained by using other porous materials. Recent advances have shown that COFs can provide a new platform for designing proton conducting materials.[52-54] Especially, the long-range ordered one-dimensional channels of 2D COFs are suitable as proton conveyer and are important for improving the proton conductivity.

Likewise, under humid and anhydrous conditions, phosphoric acid (H_3PO_4, PA) loaded Tp-Azo-COF (Figure 5) has been studied for proton conduction condition at temperatures ranging from 295 to 415 K.[55] Under anhydrous condition at 340 K, the proton conductivity of PA@Tp-Azo COF with a 5.4 wt% PA content was 6.7×10^{-5} S cm^{-1}. However, PA@Tp-Stb COF (2.8 wt% PA) without azo groups did not show any conductivity under otherwise same conditions. With increasing humidity, the conductivity of both COFs systems was further enhanced. For example, under 98% RH, at 332 K, PA@Tp-Az showed a conductivity of 9.9×10^{-4} S cm^{-1}, while PA@Tp-Stb COFs showed a conductivity of 2.3×10^{-5} S cm^{-1}. The different manners of azo (–N=N–) and non-azo (–C=C–) clearly demonstrated that the existence of azo group plays a role in proton conductivity. The formation of hydrogen-bonding networks through azo protonation under humid conditions promotes proton conduction. A similar route for TpBpy-ST COF and TpBpy-MC COF (ST and MC stand for solvothermal and mechanochemical synthesis, respectively) was employed and the proton conductivity was enhanced to 1.98×10^{-3} S cm^{-1} for PA@TpBpy-ST and 2.5×10^{-3} S cm^{-1} for PA@TpBpy-MC at 393 K under 0% RH.[56] The high proton conductivity of PA@TpBpy COF was ascribed to the existence of PA immobilized bipyridine sites, hydrogen-bonded phosphoric acid networks in the channels and low activation energy (0.11 – 0.12 eV) for proton hoping. Similarly, the cationic EB-COF:PW_{12} (PW_{12} stands for polyoxomethalates (POM) showed a proton conductivity of 3.32×10^{-3} S cm^{-1} under 97% RH at room temperature, which was much larger than that of analogous cationic EB-COF:Br (2.82×10^{-6} S cm^{-1}).[57] This

result suggests that POM in the long-range ordered one-dimensional channels promotes the proton hoping, thus facilitating proton conduction in EB-COF:PW_{12}.

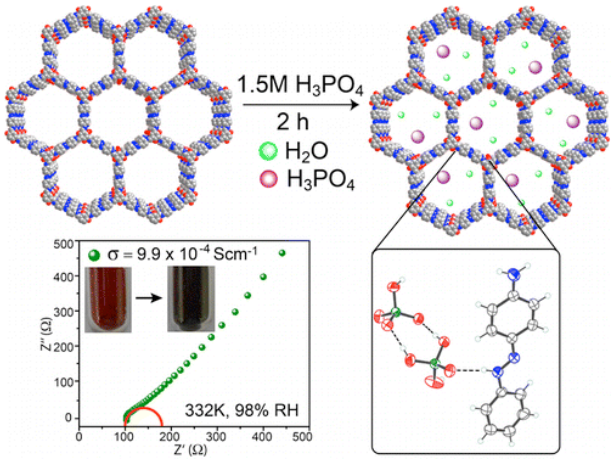

Figure 5. Schematic of PA@Tp-Azo.

Intrinsic and extrinsic proton conductivities of COFs have been studied (Figure 6) under anhydrous condition.[58] At 298 K the proton conductivity of the sulfonyl-functionalized TpPa-SO_3H COF was 1.2×10^{-5} S cm^{-1}. The conductivity was enhanced for phytic acid@TpPa-SO_3H COF to a level of 7.5×10^{-5} S cm^{-1}. The phytic acid@TpPa-Py COF at 393 K displayed a proton conductivity of 3.0×10^{-4} S cm^{-1}, which is larger than that of the phytic acid@TpPa-SO_3H COF, as a result of the fixation of phytic acid on the pyridine centers. Particularly, the phytic acid@TpPa-(SO_3H-Py) at 393 K showed a high proton conductivity of 5.0×10^{-4} S cm^{-1}, due to the coexistence of intrinsic and extrinsic proton conduction pathways.

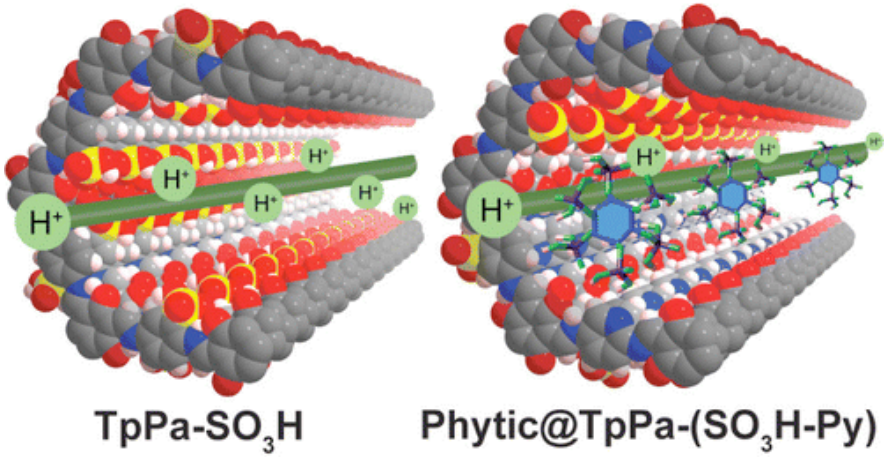

Figure 6. Schematic of TpPa-SO_3H COF and phytic acid@TpPa-SO_3H.

Under 97% RH at 25 °C, the proton conductivity of NUS-9(R) (TpPa-SO_3H COF elsewhere) accommodating monosulfonyl group-functionalized edge units was assessed to be 1.24×10^{-2} S cm^{-1}.[59] The conductivity was improved to 3.96×10^{-2} S cm^{-1} for NUS-10(R) containing bi-functionalized ($(-SO_3H)_2$) edge units under otherwise identical conditions. Notably, NUS-10(R) showed prominent stability at 298 K and 97% RH without significant loss of conductivity even after continuous operation over 15 days. Clearly, the increment in conductivity was ascribed to the existence of the water guests and their enhanced interactions with hydrophilic sulfonic acid groups in establishing the pathways for efficient proton conduction. The NUS-9(R) and NUS-10(R) COFs have the ability of constituting composite membranes by mixing COFs with nonconductive PVDF (polyvinylidene fluoride) via a solution-casting process. Among the various membranes with different loading contents of COFs, NUS-9(R)@PVDF-50 and NUS-10(R)@PVDF-50 have shown the best proton conductivity upon direct soaking COFs membrane with ultrapure water. For example, NUS-9(R)@PVDF-50 at 298 K showed high conductivity of 2.06×10^{-3} S cm^{-1}. More significantly, NUS-10(R)@PVDF-50 exhibited an increased conductivity of 5.16×10^{-3} S cm^{-1}. The activation energy of NUS-9(R)@PVDF-50 and NUS-10(R)@PVDF-50 membranes are 0.2 and 0.21 eV, respectively, indicating the Grotthuss hopping mechanism in these systems. The proton conduction is mediated by the hydrogen-bonding networks between the sulfonic acid groups and water molecules.

1.1.3.3 Ion Conduction

Unlike conventional boronates, spiroborates own high resistance toward hydrolysis. Spiroborate acts as the linkage for COFs that have the potential in ion conductive. Recently, ICOF-2 (Figure 7) consisting of Li^+ was observed to function as a Li^+ solid-state electrolyte,[60] which showed a Li^+ conductivity of 3.05×10^{-5} S cm^{-1}. Preferred direction in COFs with the array of columnar pores is benefit for the mass transport in the channels of the COFs.[61] COF-5 and TpPa-1 COF were introduced with 1M $LiClO_4$/THF to reach a content of 3.77 mol% Li^+. Their ionic conductivities are 0.26 and 0.15 mS cm^{-1} at room temperature, respectively. The pellet without Li^+

salt did not display any ion conductivity. From the linear Arrhenius plots, the ionic activation energy was calculated to be 0.037 eV for COF-5. This small activation energy indicates that the ion conduction is not relied on the temperature.

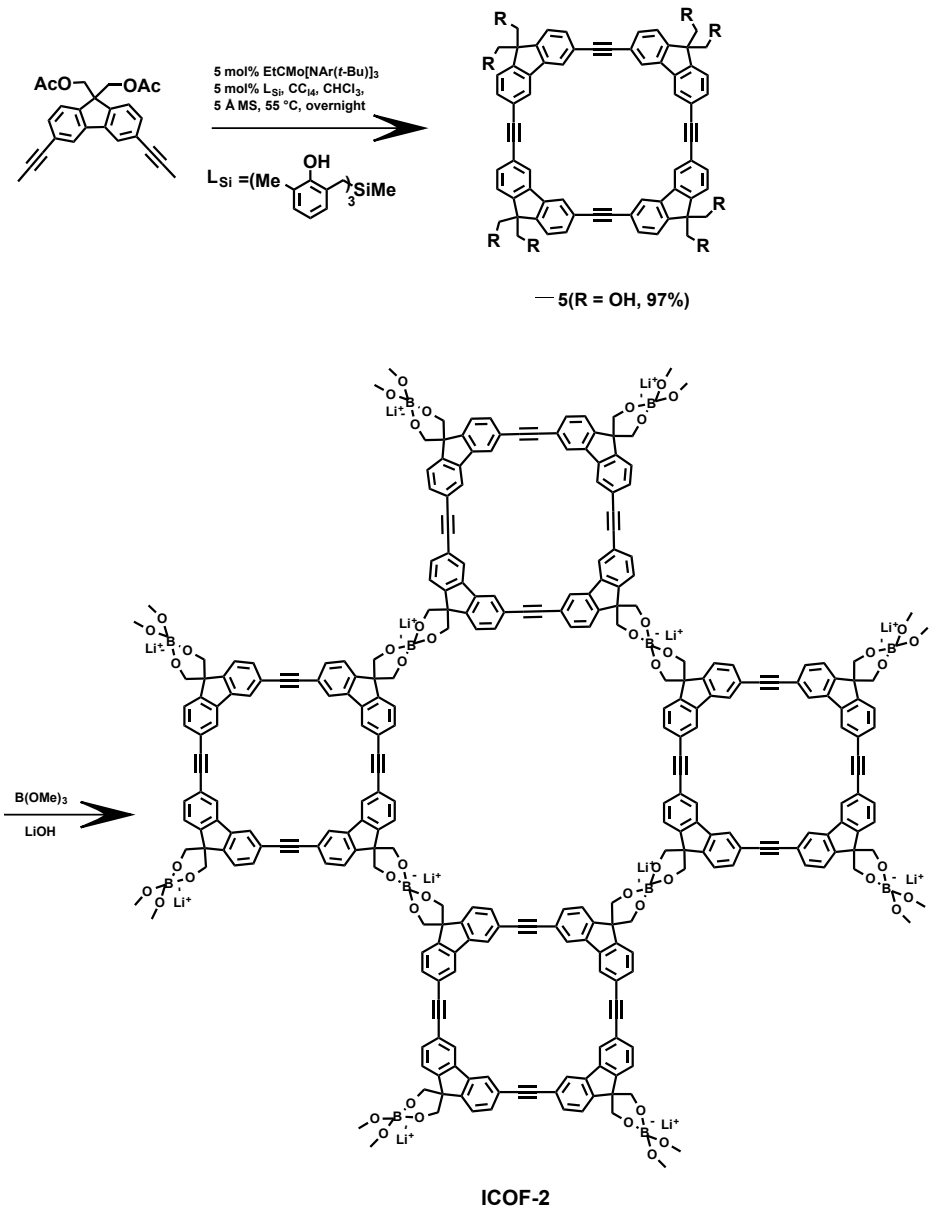

Figure 7. Schematic of ICOF-2.

1.2 Scope of This Thesis

The geometry and dimensions of the building blocks can be designed and controlled to guide the topological evolution of structural periodicity. The diversity of the building blocks and topology schemes make COFs a promising materials platform for structural and functional designs. Because of these features, COFs have shown

promising applications in different fields,[62-64] such as metal ion separation, battery, and semiconductor. Because of their high thermal, chemical and mechanical stabilities, COFs can be employed as promising membranes in fuel cells for ion conduction. In order to elucidate the molecular design principle and potential for ion-conducting COFs, I systematically designed and synthesized a series of COFs with large pores and specific pore walls.

The development of COFs in recent years was reviewed in chapter 1, including topology diagrams, synthetic reactions, and preparation methods and conditions. The properties of gas adsorption and proton conduction were also summarized.

A highly stable, crystalline mesoporous TPB-DMTP-COF was designed and synthesized in chapter 2. The crystallinity, porosity, and chemical and thermal stabilities were investigated.

The proton conduction was investigated by introducing heterocyclic organic compounds including triazole and imidazole to the channels of mesoporous TPB-DMTP-COF and these results were summarized in chapter 3.

In order to achieve excellent proton conductivity, I chose H_3PO_4 (PA) as proton carriers and introduced PA to the pores of two COFs, including TPB-DMTP-COF and TPB-DMPTA-COF. I observed that the proton conductivity was mainly governed by the amount of the PA proton carriers in the COFs, leading to the establishment of a design principle for proton conduction by using COFs with large pore and high pore volume. These results are summarized in chapter 4.

To clarify the relationship between the pore environment (pore size and pore shape such as hexagonal and Kagome channels) and the proton conduction, large pore TAPB-TMDPDA-COF and TMQPDA-PyTTA-COF were designed and synthesized. Their proton conduction was investigated in chapter 5.

To show the potential of anion conduction with COFs, the pore walls of COFs were systematically functionalized with polyelectrolytes in chapter 6. The polyelectrolyte controls the hydroxyl anion conduction across the channels of COFs.

I summarized the results of each chapter and showed the perspectives of COFs for ion conduction in chapter 7.

In this thesis, structural calculations were carried out by co-workers. Prof. Stephan Irle at Nagoya University carried out structural optimization using DFTB methods. Dr. Jia Gao, Dr. Hong Xu and Dr. Qiuhong Chen in our group contributed to the PXRD pattern simulations.

1.3 References

[1] Fautrez, J.; Pisi, E.; Cavalli, G. *Nature* **1955**, 176, 311.

[2] Powner, M. W.; Gerland, B.; Sutherland, J. D. *Nature* **2009**, 459, 239.

[3] Kouwer, P. H. J.; Koepf, M.; Le Sage, V. A. A.; Jaspers, M.; van Buul, A. M.; Eksteen-Akeroyd, Z. H.; Woltinge, T.; Schwartz, E.; Kitto, H. J.; Hoogenboom, R.; Picken, S. J.; Nolte, R. J. M.; Mendes, E.; Rowan, A. E. *Nature* **2013**, 493, 651.

[4] Gardel, M. L. *Nature* **2013**, 493, 618.

[5] Kricheldorf, H. R. *Angew. Chem. Int. Ed.* **2006**, 45, 5752.

[6] Rowan, S. J.; Cantrill, S. J.; Cousins, G. R. L.; Sanders, J. K. M.; Stoddart, J. F. *Angew. Chem. Int. Ed.* **2002**, 41, 898.

[7] Zhang, K. D.; Matile, S. *Angew. Chem. Int. Ed.* **2015**, 54, 8980.

[8] Wilson, A.; Gasparini, G.; Matile, S. *Chem. Soc. Rev.* **2014**, *43*, 1948.

[9] Rowan, S. J.; Cantrill, S. J.; Cousins, G. R. L.; Sanders, J. K. M.; Stoddart, J. F. *Angew. Chem. Int. Ed.* **2002**, 41, 898.

[10] Jin, Y.; Yu, C.; Denman, R. J.; Zhang, W. *Chem. Soc. Rev.* **2013**, 42, 6634.

[11] Jin, Y.; Wang, Q.; Taynton, P.; Zhang, W. *Acc. Chem. Res.* **2014**, 47, 1575.

[12] Xu, L. Q.; Ding, S. Y.; Liu, J. M.; Sun, J. L.; Wang, W.; Zheng, Q. Y. *Chem. Commun.* **2016**, 52, 4706.

[13] Campbell, N. L. C., R.; Ritchie, L. K.; Cooper, A. I. *Chem. Mater.* **2009**, 21, 204.

[14] Ritchie, L. K.; Trewin, A.; Reguera-Galan, A.; Hasell, T.; Cooper, A. I. *Microporous Mesoporous Mater.* **2010**, 132, 132.

[15] Wei, H.; Chai, S. Z.; Hu, N. T.; Yang, Z.; Wei, L. M.; Wang, L. *Chem. Commun.* **2015**, 51, 12178.

[16] Ren, S.; Bojdys, M. J.; Dawson, R.; Laybourn, A.; Khimyak, Y. Z.; Adams, D. J.; Cooper, A. I. *Adv. Mater.* **2012**, 24, 2357.

[17] Kuhn, P.; Antonietti, M.; Thomas, A. *Angew. Chem. Int. Ed.* **2008**, 47, 3450.

[18] Bojdys, M. J.; Jeromenok, J.; Thomas, A.; Antonietti, M. *Adv. Mater.* **2010**, 22, 2202.

[19] Chandra, S.; Kandambeth, S.; Biswal, B. P.; Lukose, B.; Kunjir, S. M.;

Chaudhary, M.; Babarao, R.; Heine, T.; Banerjee, R. *J. Am. Chem. Soc.* **2013**, 135, 17853.

[20] Biswal, B. P.; Chandra, S.; Kandambeth, S.; Lukose, B.; Heine, T.; Banerjeet, R. Mechanochemical Synthesis of Chemically Stable Isoreticular Covalent Organic Frameworks. *J. Am. Chem. Soc.* **2013**, 135, 5328.

[21] Shinde, D. B.; Aiyappa, H. B.; Bhadra, M.; Biswal, B. P.; Wadge, P.; Kandambeth, S.; Garai, B.; Kundu, T.; Kurungot, S.; Banerjee, R. *J. Mat. Chem. A* **2016**, 4, 2682.

[22] Peng, Y.; Xu, G.; Hu, Z.; Cheng, Y.; Chi, C.; Yuan, D.; Cheng, H.; Zhao, D. *ACS Appl. Mater. Interfaces* **2016**, 8, 18505.

[23] Das, G.; Shinde, D. B.; Kandambeth, S.; Biswal, B. P.; Banerjee, R. *Chem. Commun.* **2014**, 50, 12615.

[24] Colson, J. W.; Woll, A. R.; Mukherjee, A.; Levendorf, M. P.; Spitler, E. L.; Shields, V. B.; Spencer, M. G.; Park, J.; Dichtel, W. R. *Science* **2011**, 332, 228.

[25] Spitler, E. L.; Colson, J. W.; Uribe- Romo, F. J.; Woll, A. R.; Giovino, M. R.; Saldivar, A.; Dichtel, W. R., *Angew. Chem. Int. Ed.* **2012**, 51, 2623.

[26] Dai, W. Y.; Szczerbinski, J.; Mccaffrey, R.; Zenobi, R.; Jin, Y. H.; Schluter, A. D.; Zhang, W. *Angew. Chem., Int. Ed.* **2015**, 55, 213.

[27] Kuhn, P.; Antonietti, M.; Thomas, A. *Angew. Chem. Int. Ed.* **2008**, 47, 3450.

[28] Feng, X.; Ding, X.; Jiang, D. Covalent Organic Frameworks. *Chem. Soc. Rev.* **2012**, *41*, 6010-6022.

[29] Trewin, A.; Cooper, A. I. *CrystEngComm.* **2009**, 11, 1819.

[30] Díaz, U.; Corma, A. *Coord. Chem. Rev.* **2016,** 311, 85.

[31] Dalapati, S.; Addicoat, M.; Jin, S.; Sakurai, T.; Gao, J.; Xu, H.; Irle, S.; Seki, S.; Jiang, D. *Nat. Commun.* **2015**, 6:7786, doi:10.1038/ncomms8786.

[32] Feng, X.; Ding, X.; Jiang, D. *Chem. Soc. Rev.* **2012**, 41, 6010.

[33] Ding, S. Y.; Wang, W. *Chem. Soc. Rev.* **2013**, 42, 548.

[34] Feng, X.; Dong, Y.; Jiang, D. *CrystEngComm.* **2013**, 15, 1508.

[35] Zhu, Y.; Wan, S.; Jin, Y.; Zhang, W. *J. Am. Chem. Soc.* **2015**, 137, 13772.

[36] Pang, Z. F.; Xu, S. Q.; Zhou, T. Y.; Liang, R. R.; Zhan, T. G.; Zhao, X. *J. Am.*

Chem. Soc. **2016**, 4710.

[37] Huang, N.; Wang, P.; Jiang, D. *Nat. Rev. Mater.* **2016**, 1, 16068.

[38] FitzGerald, S. A.; Burkholder, B.; Friedman, M.; Hopkins, J. B.; Pierce, C. J.; Schloss, J. M.; Thompson, B.; Rowsell, J. L. C. *J. Am. Chem. Soc.* **2011**, 133, 20310.

[39] Li, Y.; Yang, R. T. *AlChE J.* **2008**, 54, 269.

[40] Furukawa, H.; Yaghi, O. M. *J. Am. Chem. Soc.* **2009**, 131, 8875.

[41] El-Kaderi, H. M.; Hunt, J. R.; Mendoza-Cortés, J. L.; Côté, A. P.; Taylor, R. E.; O'Keeffe, M.; Yaghi, O. M. *Science* **2007**, 316, 268.

[42] Furukawa, H.; Yaghi, O. M.. *J. Am. Chem. Soc.* **2009**, 131, 8875.

[43] Yu, J.-T.; Chen, Z.; Sun, J.; Huang, Z.-T.; Zheng, Q.-Y. *J. Mater. Chem.* **2012**, *22*, 5369.

[44] Zhang, Y.; Shen, X.; Feng, X.; Xia, H.; Mu, Y.; Liu, X. *Chem. Commun.* **2016**, 52, 11088.

[45] Kahveci, Z.; Islamoglu, T.; Shar, G. A.; Ding, R.; El-Kaderi, H. M. *CrystEngComm.* **2013**, 15, 1524.

[46] Hou, Y.; Zhang, X.; Sun, J.; Lin, S.; Qi, D.; Hong, R.; Li, D.; Xiao, X.; Jiang, J. *Microporous Mesoporous Mater.* **2015**, 214, 108.

[47] Li, Z. P.; Feng, X.; Zou, Y. C.; Zhang, Y. W.; Xia, H.; Liu, X. M.; Mu, Y. *Chem. Commun.* **2014**, 50, 13825.

[48] Li, Z.; Zhi, Y.; Feng, X.; Ding, X.; Zou, Y.; Liu, X.; Mu, Y. *Chem. Eur. J.* **2015**, 21, 12079.

[49] Rabbani, M. G.; Sekizkardes, A. K.; Kahveci, Z.; Reich, T. E.; Ding, R.; El-Kaderi, H. M. *Chem. Eur. J.* **2013**, 19, 3324.

[50] Cavenati, S.; Grande, C. A.; Rodrigues, A. E. *J. Chem. Eng. Data* **2004**, 49, 1095.

[51] Rabbani, M. G.; Sekizkardes, A. K.; Kahveci, Z.; Reich, T. E.; Ding, R.; El-Kaderi, H. M. *Chem. Eur. J.* **2013**, 19, 3324.

[52] Chandra, S.; Kundu, T.; Kandambeth, S.; BabaRao, R.; Marathe, Y.; Kunjir, S. M.; Banerjee, R. *J. Am. Chem. Soc.* **2014**, 136, 6570.

[53] Peng, Y.; Xu, G.; Hu, Z.; Cheng, Y.; Chi, C.; Yuan, D.; Cheng, H.; Zhao, D. *ACS Appl. Mater. Interfaces* **2016**, 8, 18505.

[54] Chandra, S.; Kundu, T.; Dey, K.; Addicoat, M.; Heine, T.; Banerjee, R. *Chem. Mater.* **2016**, 28, 1489.

[55] Chandra, S.; Kundu, T.; Kandambeth, S.; BabaRao, R.; Marathe, Y.; Kunjir, S. M.; Banerjee, R. *J. Am. Chem. Soc.* **2014**, 136, 6570.

[56] Shinde, D. B.; Aiyappa, H. B.; Bhadra, M.; Biswal, B. P.; Wadge, P.; Kandambeth, S.; Garai, B.; Kundu, T.; Kurungot, S.; Banerjee, R. A *J. Mat. Chem. A*. **2016**, 4, 2682.

[57] Ma, H.; Liu, B.; Li, B.; Zhang, L.; Li, Y. G.; Tan, H. Q.; Zang, H. Y.; Zhu, G. *J. Am. Chem. Soc.* **2016**, 138, 5897.

[58] Chandra, S.; Kundu, T.; Dey, K.; Addicoat, M.; Heine, T.; Banerjee, R. *Chem. Mater.* **2016**, 28, 1489.

[59] Peng, Y.; Xu, G.; Hu, Z.; Cheng, Y.; Chi, C.; Yuan, D.; Cheng, H.; Zhao, D. *ACS Appl. Mater. Interfaces* **2016**, 8, 18505.

[60] Du, Y.; Yang, H.; Whiteley, J. M.; Wan, S.; Jin, Y.; Lee, S. H.; Zhang, W. *Angew. Chem. Int. Ed.* **2016**, 55, 1737.

[61] Vazquez-Molina, D. A.; Mohammad-Pour, G. S.; Lee, C.; Logan, M. W.; Duan, X.; Harper, J. K.; Uribe-Romo, F. J. *J. Am. Chem. Soc.* **2016**, 138, 9767.

[62] Wang, S.; Wang, Qi.; Shao, P.; Han, Y.; Gao, X.; Ma, L.; Yuan, S.; Ma, X.; Zhou, J.; Feng , X.; Wang, B. *J. Am. Chem. Soc.* **2017**, 139, 4258.

[63] Sun, Q.; Aguila, B.; Perman, J.; Earl, L. D.; Abney, C. W.; Cheng, Y.; Wei, H.; Nguyen, N.; Wojtas, L.; Ma, S. *J. Am. Chem. Soc.* **2017**, 139, 2786.

[64] Huang, N.; Krishna, R.; Jiang, D. *J. Am. Chem. Soc.* **2015**, 137, 7079.

Chapter 2

Design and Synthesis of Stable Crystalline Porous Covalent Organic Frameworks

Abstract

In this chapter, I prepared the stable, crystalline, porous covalent organic frameworks and named it as TPB-DMTP-COF. The TPB-DMTP-COF was characterized for the crystalline structure using powder X-ray diffraction (PXRD), porosity using nitrogen sorption method, thermal stability using thermogravimetric analysis (TGA). The chemical stability was investigated by measuring the crystallinity and porosity after treatment in different organic solvents, water (25 and 100 °C), and concentrated HCl and aqueous NaOH solutions (14 M) for seven days.

2.1 Introduction.

COFs are porous polymers with long-range structural orderings and built-in porosity.[1–6] The COFs are unique because they enable the predesign of structure and can be experimentally controlled by using various chemical approaches. COFs thus represent a new materials platform for designing new molecular systems that have potential applications in many fields. Despite the fact of structural design ability and diversity, COFs are usually unstable because their linkages are made from reversible reactions, with a possibility of structural deterioration under certain conditions. Designing a COF structure with robust stability remains a chemical challenge.

In this Chapter, TPB-DMTP-COF was designed and synthesized. This COF was stable in organic solvents and aqueous solutions under harsh conditions. I measured the porosity, crystallinity and thermal stability. Boroxine and boronate–ester linked COFs usually have highly crystalline and porosity but they are easy to be destroyed in the presence of water or protic media.[7–12] On the other hand, COFs constructed from other linkages, such as hydrazone, imine, azine, triazine, and phenazine are stable, but they are usually low in crystalllinity and porosity.[13–18] Although rapid progress in the synthesis of COFs over recent years has been achieved, combining stability, crystallinity, and porosity in one COF structure is still a challenging. Theoretically, the chemical stability of COFs is controlled by the combination of two forces. The first one is the bond strength within a covalent layer and the second one is the force from the interlayer interactions. The layered structure is determined from the interlayer interactions and, hence, exerts a great influence on the crystallinity and porosity. For example, in imine-linked COFs, different polarity between the carbon and nitrogen atoms resulted in the partially polarized C=N bond in which the carbon atom tends to carry positive charge while the nitrogen bears a negative charge. In the hexagonal 2D COF, one pore structure consists of as many as 12 polarized C=N units (Fig. 1), so that a large number of repulsive blocks have to stack in the frameworks that result in electrostatic repulsion and reduce the stability of the materials.

2.2 Design and Synthesis of TPB-DMTP-COF.

The introduction of methoxy groups into the edge units of COFs has been shown its great effect on enhancing the structural stability of the resulting COFs.[19]. I have synthesized the imine-linked stable COF, i.e., TPB-DMTP-COF (Fig. 1). In detail, monomers of TAPB (28.1 mg) and DMTA (23.3 mg) were added into a 10-mL vial which contained 1 mL *o*-DCB/*n*-BuOH (1:1) mixture, followed by introducing CH_3COOH (0.1 mL, 6 M). The vial was degassed, sealed, and kept at 120 °C for 72 h. The precipitate was washed by using Soxhlet extraction with THF and dried under vacuum. The COF was isolated in a yield of 81%.[19]

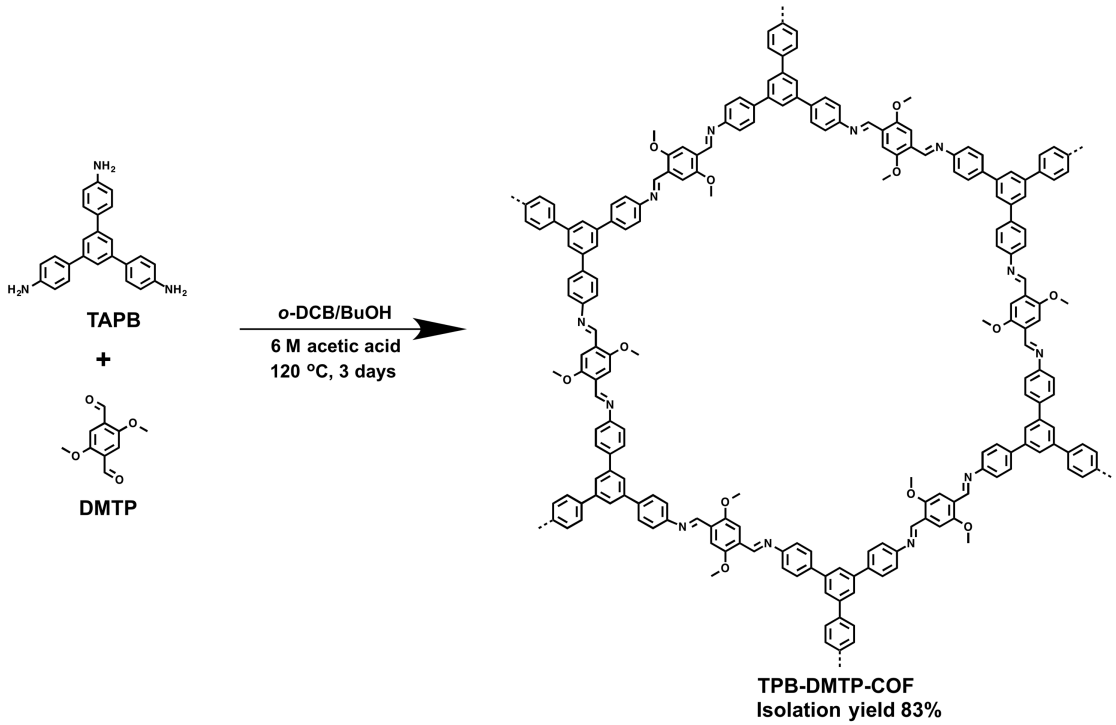

Fig. 1. The design and synthesis of TPB-DMTP-COF.

2.2.1 Characterize of TPB-DMTP-COF[19]

The powder X-ray diffraction (PXRD) profile of TPB-DMTP-COF was shown in figure 2. It demonstrated six diffraction peaks, with the most intensive one at 2.76° and the five other peaks at 4.82, 5.60, 7.42, 9.70 and 25.2°; these peaks were assigned to the (100), (110), (200), (210), (220) and (001) facets, respectively (Figure 2, red curve). In Figure 2, the Pawley refinement (green) confirms the correctness of peak assignment as supported by their small discrepancy (black curve). Structural

simulations based on density function tight bonding (DFTB) method resulted in the eclipsed stacking mode (Figure 2, blue curve).

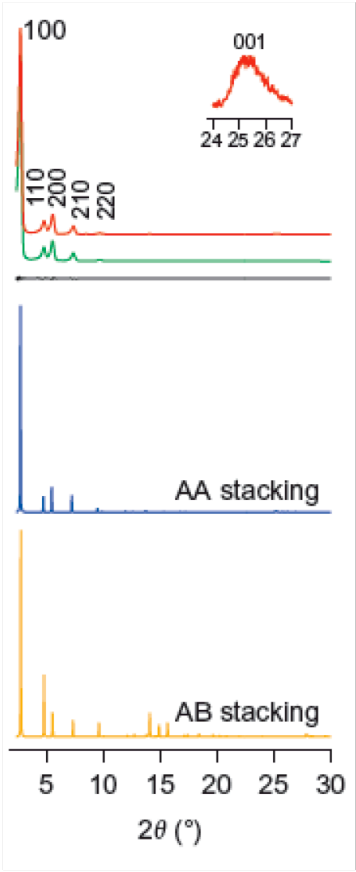

Figure 2. PXRD profiles of TPB-DMTP-COF. Experimentally observed (red), Pawley refined (green) and their difference (black), simulated using the AA stacking mode (blue) and the staggered AB stacking mode (orange).

The chemical stability of TPB-DMTP-COF was investigated by dispersing the COF samples in various kinds of solvents, including dimethylsulfoxide (DMSO), MeOH, dimethylformamide (DMF), cyclohexanone, THF, water (100 and 25 °C), and aqueous NaOH (14 M) and HCl (12 M) solutions for 7 days.[19] The initial crystalline structure of TPB-DMTP-COF was kept, as suggested by the invariable positions and intensities of the peaks in its PXRD profile on dispersion for 7 days in DMSO, MeOH, DMF, cyclohexanone, THF, water (100 and 25 °C), and aqueous NaOH (14 M) solutions and HCl (12 M) solutions.

The remained weight percentages of the COF after treated in different solvents were illustrated in Figure 3. When TPB-DMTP-COF was treated in the common polar and nonpolar organic solvents, there was nearly no decrease of the mass (<0.1 wt%). Even in concentrated HCl and NaOH solution (14 M), it could still retain 85 and 92 wt%, respectively. Surprisingly, TPB-DMTP-COF could keep its initial mass up to 72 wt% in boiling water (100 °C) after 7 days.[19]

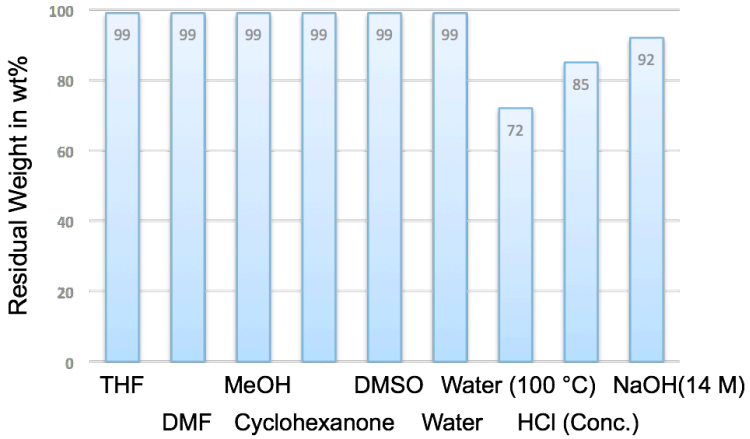

Figure 3. Residue weight percentages of TPB-DMTP-COF after one-week treatment in various solvents.

The porosity of TPB-DMTP-COF was investigated by the N_2 adsorption and desorption analysis and there was a quick arising step between P/P_0 = 0.15 - 0.25 (Fig. 4A, black curve). The isotherm could be best depicted as a type IV isotherm that is representative of mesoporous materials. TPB-DMTP-COF has a surface area of 2130 $m^2\ g^{-1}$. The pore size and pore volume of TPB-DMTP-COF were 3.26 nm (Fig. 4B, black curve) and 1.34 $cm^3\ g^{-1}$ (Fig. 4B, red curve), respectively. The surface area obtained from experiment was quite close to the theoretical value (2098 $m^2\ g^{-1}$), which was calculated from the AA-stacking mode. The surface area of TPB-DMTP-COF was 2081, 2074, and 2020 $m^2\ g^{-1}$ after one-week treatment in boiling water (100 °C) (Fig. 4A, blue curve), concentrated HCl (green curve), and aqueous NaOH solution (red curve).

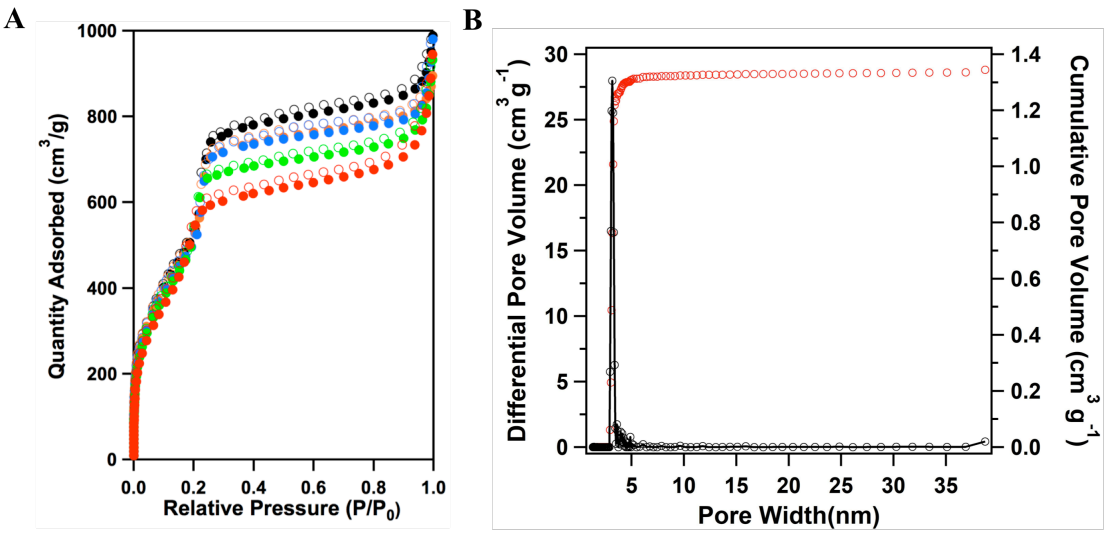

Figure 4. (A) N_2 sorption isotherm curves of TPB-DMTP-COF (black), TPB-DMTP-COF treated with 100 ° C water (blue), 14 M NaOH (red) and concentrated HCl (green) for seven days. Filled and open circles represent adsorption and desorption. (B) Pore size (black) and pore size distribution (red) profiles of TPB-DMTP-COF.

In Figure 5, TGA curve revealed that TPB-DMTP-COF did not show obvious decrease of mass before 400 °C under N_2.

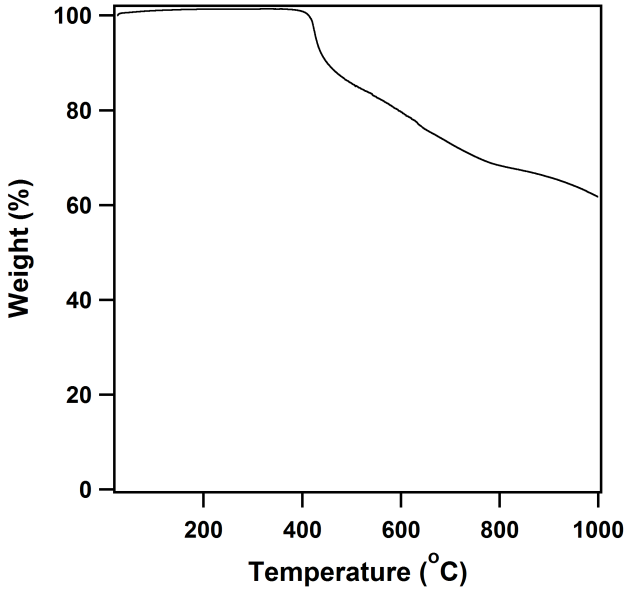

Figure 5. TGA curve of TPB-DMTP-COF under N_2.

In summary, TPB-DMTP-COF has a large porosity, and excellent chemical and thermal stabilities. This stability makes the COF possible as a porous media for developing various proton-conducting properties.

2.3 Experimental Sections

2.3.1 Methods

All the PXRD data were collected from 2θ = 1.0° to 30° by using the Rigaku RINT Ultima III diffractometer with a 0.02° increment step. At 77 K, N_2 sorption isotherms were conducted via a 3Flex surface characterization analyzer with the Micrometrics Instrument Corporation model. The specific surface areas were calculated by the Brunauer-Emmett-Teller (BET) method. The entire TGA measurements were measured with a 10 °C min^{-1} enhancement rate under N_2 on a Mettler-Toledo model TGA/SDTA851e, from 25 to 800 °C.

2.3.2 Materials and Synthetic Procedures

The common solvents such as *o*-dichlorobenzene (*o*-DCB), tetrahydrofuran (THF), and *N, N*-dimethylformide (DMF) were bought from Kanto Chemicals. CH_3COOH, 1-butanol, mesitylene, and dioxane were bought from Wako Chemicals. TAPB and 1,4-dimethoxybenzene were bought from TCI. 2,5-Dimethoxyterephthalaldehyde (DMTA) was prepared by reported methods.[20]

2.4 References

[1] Feng, X.; Ding, X.; Jiang, D. *Chem. Soc. Rev.* **2012**, 41, 6010.

[2] Ding, S. Y.; Wang, W. *Chem. Soc. Rev.* **2013**, 42, 548.

[3] Cote, A. P.; Benin, A. I.; Ockwig, N.W.; O'Keeffe, M.; Matzger, A. J.; Yaghi, O. M. *Science* **2005,** 310, 1166.

[4] Tilford, R.W.; Gemmill,W. R.; zur Loye, H. C.; Lavigne, J. J. *Chem. Mater.* **2006**,18, 5296.

[5] Belowich, M. E.; Stoddart, J. F. *Chem. Soc. Rev.* **2012**, 41, 2003.

[6] Xiang, Z. H.; Cao, D. P.; Dai, L. M. *Polym. Chem.* **2015**, 6, 1896.

[7] Cote, A. P.; El-Kaderi, H. M.; Furukawa, H.; Hunt, J. R.; Yaghi, O. M. *J. Am. Chem. Soc.* **2007**, 129, 12914.

[8] Wan, S.; Guo, J.; Kim, J.; Ihee, H.; Jiang, D. *Angew. Chem. Int. Ed.* **200**8, 47, 8826.

[9] Tilford, R. W.; Mugavero, S. J.; Pellechia, P. J.; Lavigne, J. J. *Adv. Mater.* **2008**, 20, 2741.

[10] Wan, S.; Guo, J.; Kim, J.; Ihee, H.; Jiang, D. *Angew. Chem. Int. Ed.* **2009**, 48, 5439.

[11] Campbell, N. L.; Clowes, R.; Ritchie, L. K.; Cooper, A. I. *Chem. Mater.* **2009**, 21, 204.

[12] Spitler, E. L.; Dichtel,W. R. *Nat. Chem.* **2010**, 2, 672.

[13] Wan, S.; Gandara, F.; Asano, A.; Furukawa, H.; Saeki, A.; Dey, S.K.; Liao, L.; Ambrogio, M.W.; Botros, Y.Y.; Duan, X.; Seki, S.; Stoddart, J.F.; Yaghi, O. M. *Chem. Mater.* **2011**, 23, 4094.

[14] Uribe-Romo, F. J.; Doonan, C. J.; Furukawa, H.; Oisaki, K.; Yaghi, O. M. *J. Am. Chem.Soc.* **2011**, 133, 11478.

[15] Kandambeth, S.; Mallick, A.; Lukose, B.; Mane, M.V.; Heine, Thomas,; Banerjee, R. *J. Am. Chem. Soc.* **2012**, 134, 19524.

[16] Dalapati, S.; Jin S.; Gao, J.; Xu, Y.; Nagai, A.; Jiang, D. *J. Am. Chem. Soc.* **2013**, 135, 17310.

[17] Kuhn, P.; Antonietti, M.; Thomas, A. *Angew. Chem. Int. Ed*. **2008**, 47, 3450.

[18] Guo, J.; Xu, Y.; Jin, S.; Chen, L.; Kaji, T.; Honsho, Y.; Addicoat, M. A.; Kim, J.; Saeki, A.; Ihee, H.; Seki, S.; Irle, St.; Hiramoto, M.; Gao J.; Jiang, D. *Nat. Commun.* **2013**, 4, 2736.

[19] Xu. H.; Gao, J.; Jiang. D. *Nat. Chem.* **2015**, 7, 905.

[20] Kuhnert, N.; Rossignoloa, G. M.; Lopez-Periagoa, A. *Org. Biomol. Chem.* **2003**, 1, 1157.

Chapter 3

Proton Conduction in Crystalline, Mesoporous, Covalent Organic Frameworks with Organic Heterocyclic Proton Carriers

Nat. Mater. **2016**, 15, 722-727.

Hong Xu, Shanshan Tao and Donglin Jiang

Abstract

In this chapter, I utilized the stable COFs to investigate proton conduction. I demonstrated the loading of organic proton carriers of imidazole and triazole into the pores of the COFs and investigated their proton conduction properties over 100 °C. Proton conductivities of these COFs are far superior to those of conventional microporous materials with an enhancement by two orders of magnitude. The activation energy for the proton conduction was evaluated and a conduction mechanism based on proton hopping was proposed.

3.1 Introduction

Polyelectrolytes[1-5] and microporous polymers[6-10] have attracted great attention over the past decades as proton-conducting materials. However, polyelectrolytes without well-defined structures have limited practical implementation. Inspired by the biological ion channels,[11] porous polymers have been developed.[12-14] A typical method is based on bottom-up approach via self-assembly of block copolymers. However, the resulting phase-separation domain structures are hard to yield ordered and steady structure.[1,5] Recently, microporous materials such as metal-organic frameworks (MOFs)[6-10] have been intensively investigated for proton conduction. At 100-130 °C, MOFs have obtained a conductivity of 10^{-5}-10^{-4} S cm^{-1} with the proton carriers of *N*-heterocyclic imidazole (im) or triazole (trz).[15,16] However, the use of mesoporous materials was not encouraged because of a preconception that mesopores would lead to the escape of proton carriers instead of proton conduction.

The author demonstrated proton conduction in COFs with mesoporous structure. COFs are a class of crystalline porous polymer that enables the construction of ordered frameworks.[14,17-25] TPB-DMTP-COF (Fig. 1) with a pore size of 3.26 nm was prepared by polycondensation under solvolthermal conditions as reported.[23]

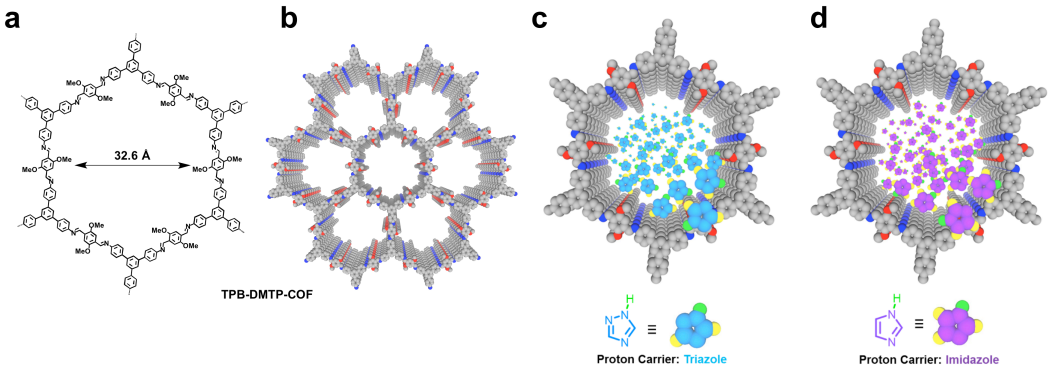

Figure 1. a, Schematics of the stable, crystalline, mesoporous COF (TPB-DMTP-COF) with a pore size of 32.6 Å. **b,** Hexagonal structure of TPB-DMTP-COF, showing ordered one-dimensional open channels. **c, d,** Graphic

representations of (**c**) 1,2,4-triazole and (**d**) imidazole molecules in the channels.

3.2 Results and Discussions

3.2.1 Structural Characterizations of COFs

The crystallinity was investigated using the PXRD method. In Figure 2a, there were seven prominent peaks at 2.76°, 4.82°, 5.60°, 7.42°, 9.70°, 14.08°, and 25.2°, and these peaks could be ascribed to the (100), (110), (200), (210), (220), (500), and (001) facets, respectively (Fig. 2a, black curve). The simulated results were presented in Appendix table 1-4.[23] In adjacent layers, the distance between the layers was 3.52 Å. This lattice structure confirms the formation of hexagonally aligned, dense, and 1D mesopores. The pore size based on the crystal structure is 3.26 nm. TPB-DMTP-COF afforded straight 1D channels, which resembles that of the biological ion channels and is ideal for ion conduction.[11,13]

TPB-DMTP-COF displayed a typical type-IV N_2 sorption isotherm, which is characteristic of a mesoporous material (Fig. 2e). The BET surface area was 2072 m^2 g^{-1} and Langmuir surface area was 3257 m^2 g^{-1}. The pore size is 3.26 nm and the pore volume is 1.34 cm^3 g^{-1}, as revealed by the pore size distribution profile (Fig. 2f). Especially, the experimental BET surface area is very close to the theoretical BET surface area (2098 m^2 g^{-1}), indicating the high structural integrity and porosity of TPB-DMTP-COF.

The chemical stability of TPB-DMPT-COF was investigated in different organic solvents, including dimethylsulfoxide, tetrahydrofuran, *N*,*N*-dimethylformamide, cyclohexanone, and methanol. After treated in the organic solvents for seven days, TPB-DMPT-COF could still retain its crystallinity and porosity. TPB-DMPT-COF was also stable in water (25 and 100 °C) and aqueous NaOH (14 M) and HCl (12 M) solutions for seven days; it kept the crystallinity and porosity under these conditions.[23] Since triazole (trz) was employed as the proton carriers, I investigated the stability of TPB-DMPT-COF by keeping TPB-DMPT-COF in trz for seven days at 120 °C. TPB-DMTP-COF keeps its structural integrity in the melting trz (Fig. 2a and 2e,

green). TGA curve indicated TPB-DMTP-COF had a good thermal stability and did not decompose before 400 °C under N_2 atmosphere.[23]

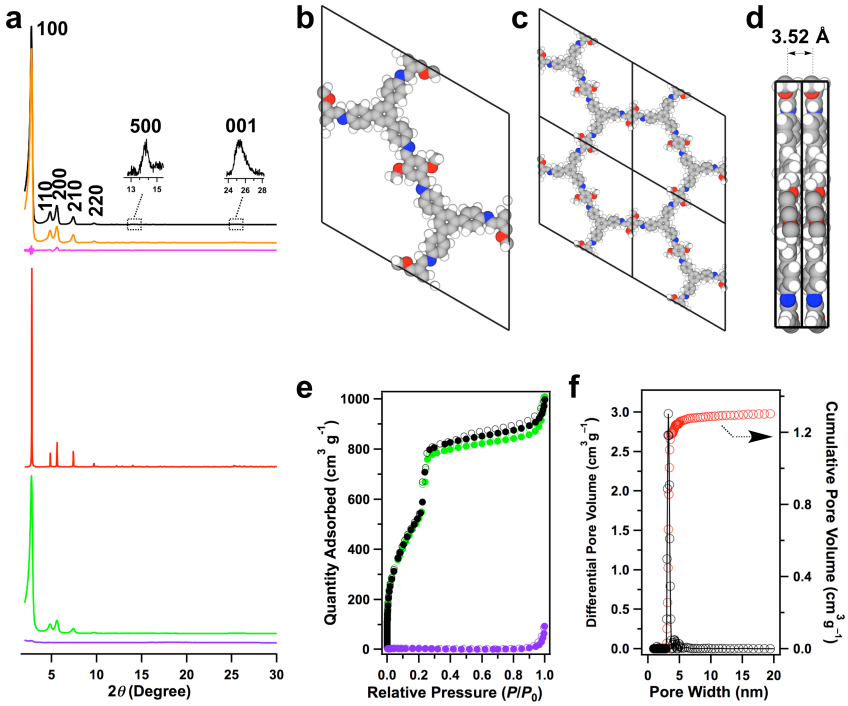

Figure 2. a, PXRD patterns of TPB-DMTP-COF (black curve), the Pawley refinement result (orange curve) and their difference (magenta curve), the AA-stacking mode of the *P6* space group (blue curve), TPB-TP-COF (purple curve), and TPB-DMTP-COF treated in 1,2,4-triazole at 120 °C for a week (green curve). **b,** Unit cell of AA-stacking mode of TPB-DMTP-COF. **c,** Crystal structure of a single pore. **d,** Crystal structure of layers in TPB-DMTP-COF; the inter-layer distance is 3.52 Å. **e,** Nitrogen sorption isotherm profiles of TPB-DMTP-COF (black), TPB-TP-COF (purple), and TPB-DMTP-COF treated with 1,2,4-triazole at 120 °C for one week (green). **f,** Pore size (black) and pore size distribution (red) profiles of TPB-DMTP-COF.

The stability against oxidation was investigated by using an established method with free radicals produced by Fenton reagents and the results show a high stability of of TPB-DMTP-COF (Fig. 3, blue curve). Therefore, TPB-DMPT-COF is a chemical

and thermal stable, crystalline, mesoporous polymer.

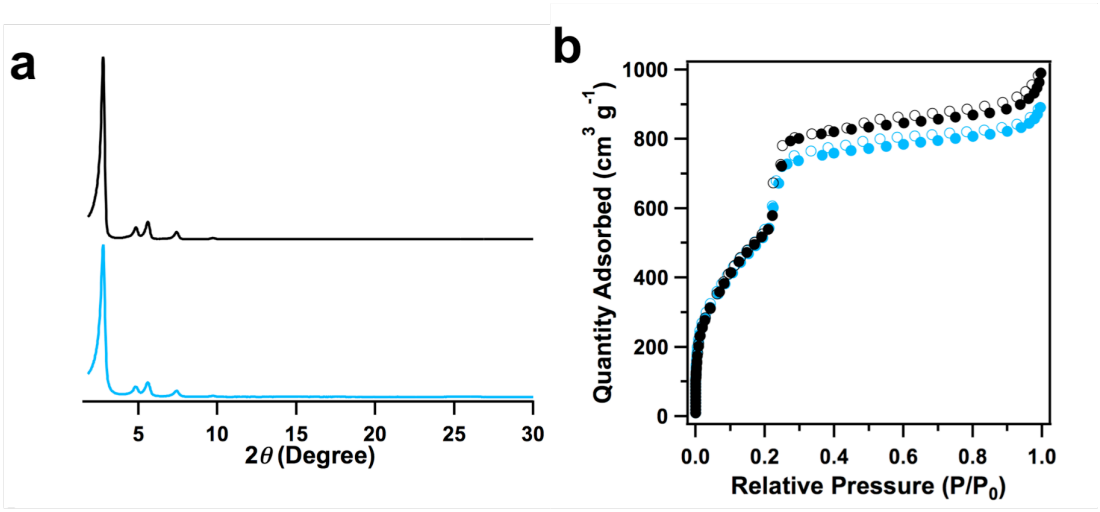

Figure 3. a, PXRD patterns of TPB-DMTP-COF (black curve) and TPB-DMTP-COF treated in Fenton's reagent for 24 h (blue curve). **b,** N_2 sorption isotherm profiles of TPB-DMTP-COF (black curve) and TPB-DMTP-COF treated in Fenton's reagent for 24 h (blue curve).

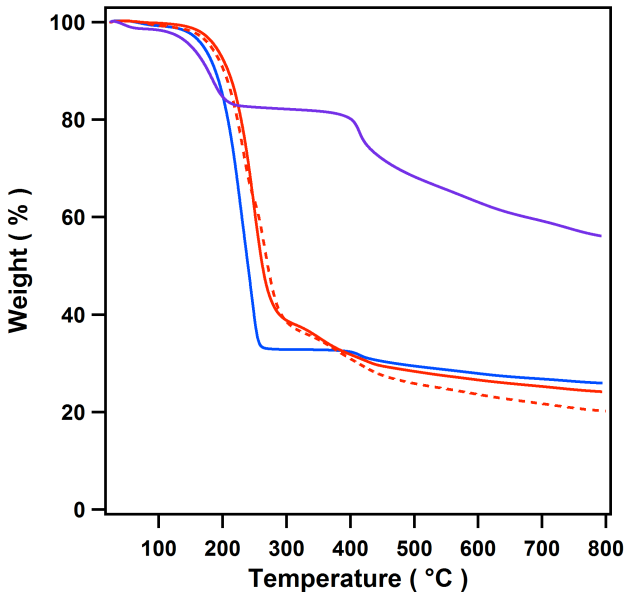

Figure 4. TGA curves of im@TPB-TP-COF (purple), d_4-im@TPB-DMTP-COF (red dash), im@TPB-DMTP-COF (red), and trz@TPB-DMTP-COF (blue) measured under N_2.

TPB-DMTP-COF has a pore volume of 1.34 cm^3 g^{-1} and could accommodate trz into its channels with the highest loading content of 186 wt%. For trz-loaded COFs, the porosity including pore size and pore volume almost disappeared. The results indicate that the channels are filled with trz. From Figure 4, the TGA curve suggested that the trz in the channels began to release from 210 °C and finished around 260 °C under N_2 atmosphere (Fig. 4, blue curve). Collectively, these results suggest that trz@TPB-DMTP-COF has sufficient thermal stability for proton conduction. Because TPB-DMTP-COF was investigated in trz at high temperature, the thermal stability was also investigated. The samples still kept original weights; this result suggests that there is no loss of trz molecules.

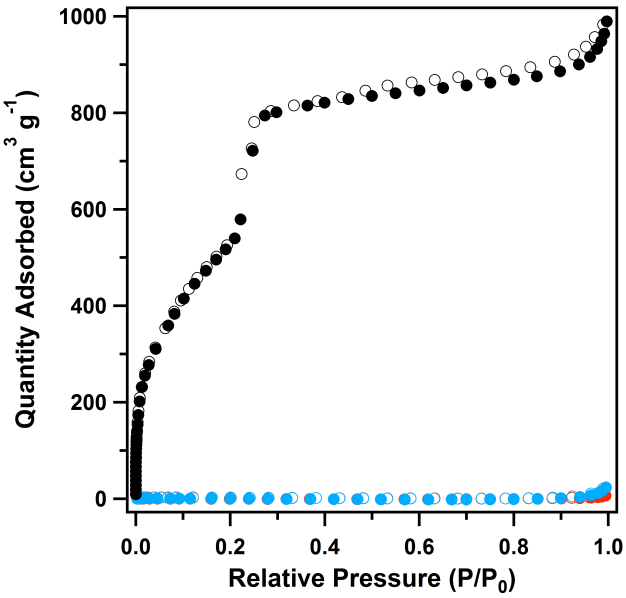

Figure 5. Isotherms of trz@TPB-DMTP-COF (red curve), im@TPB-DMTP-COF (blue curve), and TPB-DMTP-COF (black curve).

3.2.2 Impedance Spectroscopy

The conductivities were measured via alternating-current (AC) impedance spectroscopy, which was an established electrochemical method to characterize intrinsic ion-conducting properties of materials. Figure 6a-d displayed the results at temperatures ranging from 100 to 130 °C. At low frequencies, there existed a tail of

semicircle that suggested the blocked protons at Ag electrodes. The proton conductivities of trz@TPB-DMTP-COF were 7.0×10^{-4} (100 °C), 7.7×10^{-4} (105 °C), 8.2×10^{-4} (110 °C), 8.8×10^{-4} (115 °C), 9.6×10^{-4} (120 °C), 1.0×10^{-3} (125 °C), 1.1×10^{-3} S cm^{-1} (130 °C) (Fig. 6a-d, 7a-c).

The proton conductivity of TPB-DMTP-COF itself could be ignored ($<10^{-12}$ S cm^{-1}); this indicates that TPB-DMTP-COF is an electric insulator. Thus it is suitable as the exchange membrane polymer, which requires the electrically insulating materials that avoid inner current short cut. According to the temperature-dependent conductivity profiles (Fig. 8a), the activation energy was calculated as 0.21 eV. For the proton conduction system, the small activation energy value indicates a Grotthuss-type hopping mechanism in the long-ranged, one-dimensional, mesoporous channels.

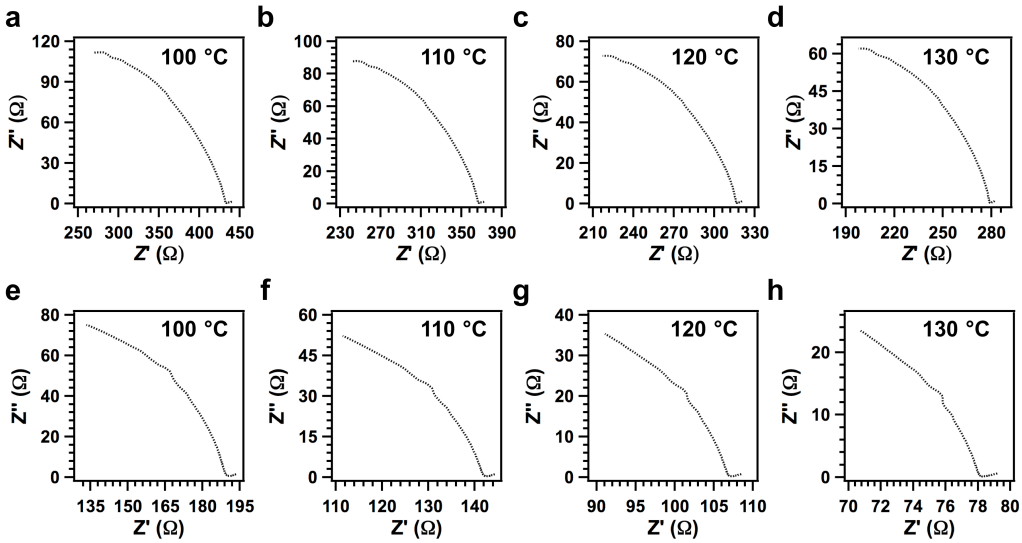

Figure 6. Impedance spectroscopy. Nyquist plots of (**a-d**) trz@TPB-DMTP-COF and (**e-h**) im@TPB-DMTP-COF measured at various temperatures.

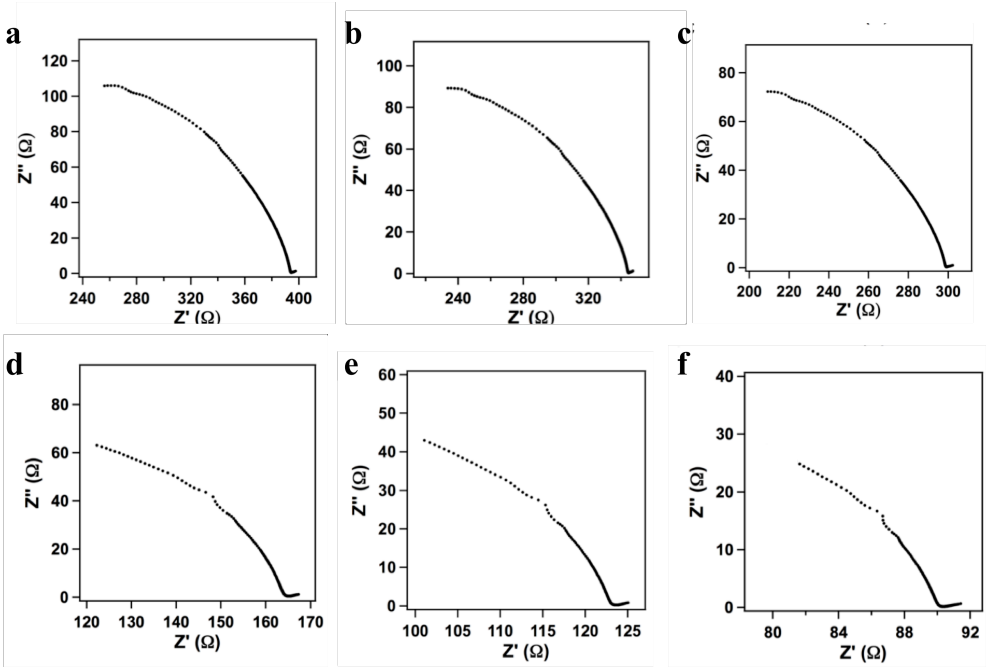

Figure 7. Nyquist plots of trz@TPB-DMTP-COF at various temperatures of (**a**) 105 °C, (**b**) 115 °C, and (**c**) 125 °C, and im@TPB-DMTP-COF (**d**) 105 °C, (**e**) 115 °C, and (**f**) 125 °C.

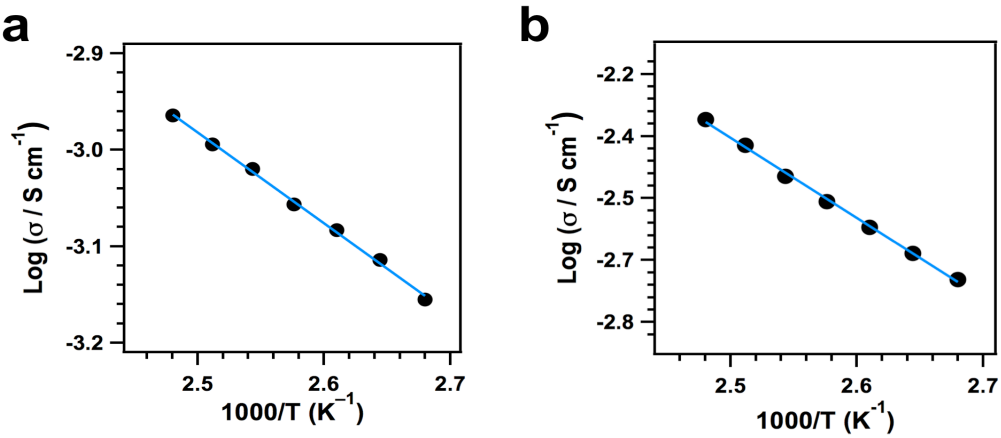

Figure 8. Arrhenius Plots. Temperature dependence of proton conductivities of (**a**) trz@TPB-DMTP-COF and (**b**) im@TPB-DMTP-COF. Black dots are experimental data; blue lines are curve-fitting results.

In order to confirm if the other kinds of proton carriers also displayed proton conductivity in the COFs. Imidazole (im) was introducing into COF and formed the

im@TPB-DMTP-COF through the same route used for the triazole-loaded COF. The TGA curve revealed that there was 155 wt% im in the channels (Fig. 4, red curve), which was quite close to the highest content. The trapped im began to evaporate from the mesopores of TPB-DMTP-COF at 220 °C and complete at 280 °C from the TGA curve under nitrogen flow (Fig. 4, red curve). The im@TPB-DMTP-COF showed almost no porosity (Fig. 5, blue curve). These results suggest that im proton carriers almost fully occupy the COF channels. To value the effect of the humidity on the imidazole in the COF, the powder sample was placed in a tube with 100% humidity for more than 15 days. After this treatment, it could still keep 99.3 wt% of its initial mass.

The curves of proton conductivity of im-loaded COFs were similar to those of the trz-loaded samples. The conductivities were evaluated to be 1.79×10^{-3} (100 °C), 2.07×10^{-3} (105 °C), 2.39×10^{-3} (110 °C), 2.76×10^{-3} (115 °C), 3.19×10^{-3} (120 °C), 3.78×10^{-3} (125 °C), and 4.37×10^{-3} S cm^{-1} (130 °C) (Fig. 6e-h, Fig. 7d-f).

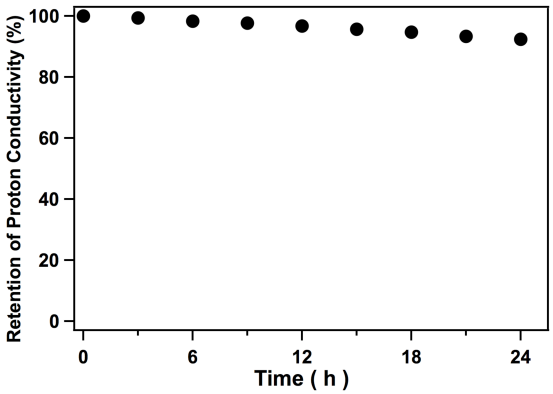

Figure 9. Time-dependent conductivity of im@TPB-DMTP-COF upon continuous run at 130 °C.

Continuous measurements were conducted and revealed that im@TPB-DMPT-COF retained the proton conductivity after 24-h-continuous run at 130 °C (Fig. 9). In order to evaluate the long-term durability, im@TPB-DMTP-COF or trz@TPB-DMTP-COF samples were sealed in vials and kept at 130 °C for 30 days. The im@TPB-DMTP-COF and trz@TPB-DMTP-COF retained 93 wt% and 85 wt%

of their initial weights, respectively, confirming a long-term thermal stability.

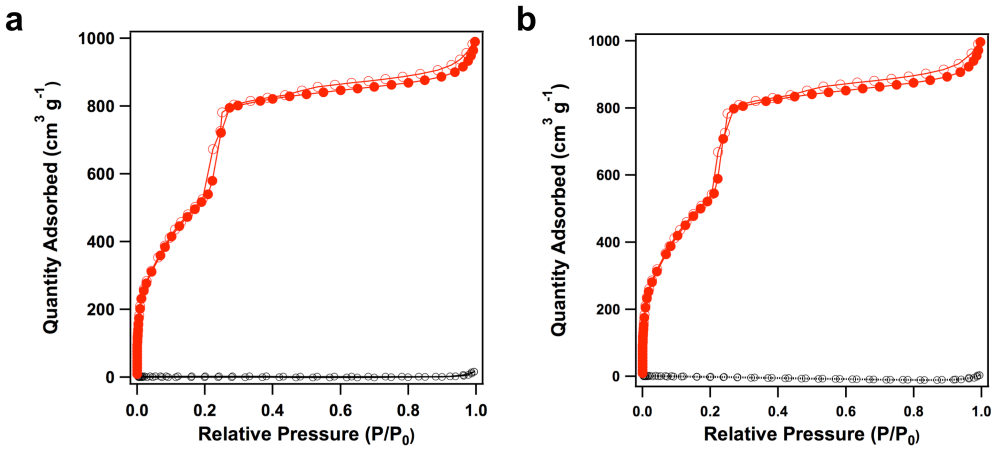

Figure 10. Nitrogen sorption isotherm curves of the im@TPB-DMTP-COF (**a**, black) and trz@TPB-DMTP-COF (**b**, black) upon 24-h-continuous run at 130 °C, in comparison with the curves of TPB-DMTP-COF (red).

The porosity of these samples after 24-h-continuous run at 130 °C was investigated to confirm whether im or trz molecules were leaked from the channels. Interestingly, these two samples still showed poor porosity as those of the samples before measurements (Fig. 10). These results suggest that imidazole and trazole does not leak from the mesopores of the COFs. The im@TPB-DMTP-COF showed a better conductivity than that of trz@TPB-DMTP-COF, as a result of the relatively low proton concentration in the trz@TPB-DMTP-COF system, because there are two lone-paired N atoms in trz. Similar case of difference has been reported for the pure im or trz systems.[26, 27]

According to the temperature-dependent conductivity profiles (Fig. 8b), the activation energy in im@TPB-DMTP-COF was determined to be 0.38 eV, which suggests a Grotthuss hopping mechanism for proton conduction in this mesoporous COF.

In order to confirm the mechanism, the d_4-im was employed and introduced to the channels of TPB-DMTP-COF with a content of 168 wt% (Fig. 4, dashed red

curve). The proton conductivity of d_4-im@TPB-DMTP-COF was 1.01×10^{-3} (100 °C), 1.13×10^{-3} (105 °C), 1.25×10^{-3} (110 °C), 1.38×10^{-3} (115 °C), 1.53×10^{-3} (120 °C), 1.68×10^{-3} (125 °C), and 1.84×10^{-3} (130 °C) S cm^{-1} (Fig. 11). These conductivities were nearly half those of im@TPB-DMTP-COF. The activation energy of ion conduction was calculated to be 0.25 eV (Fig. 12).

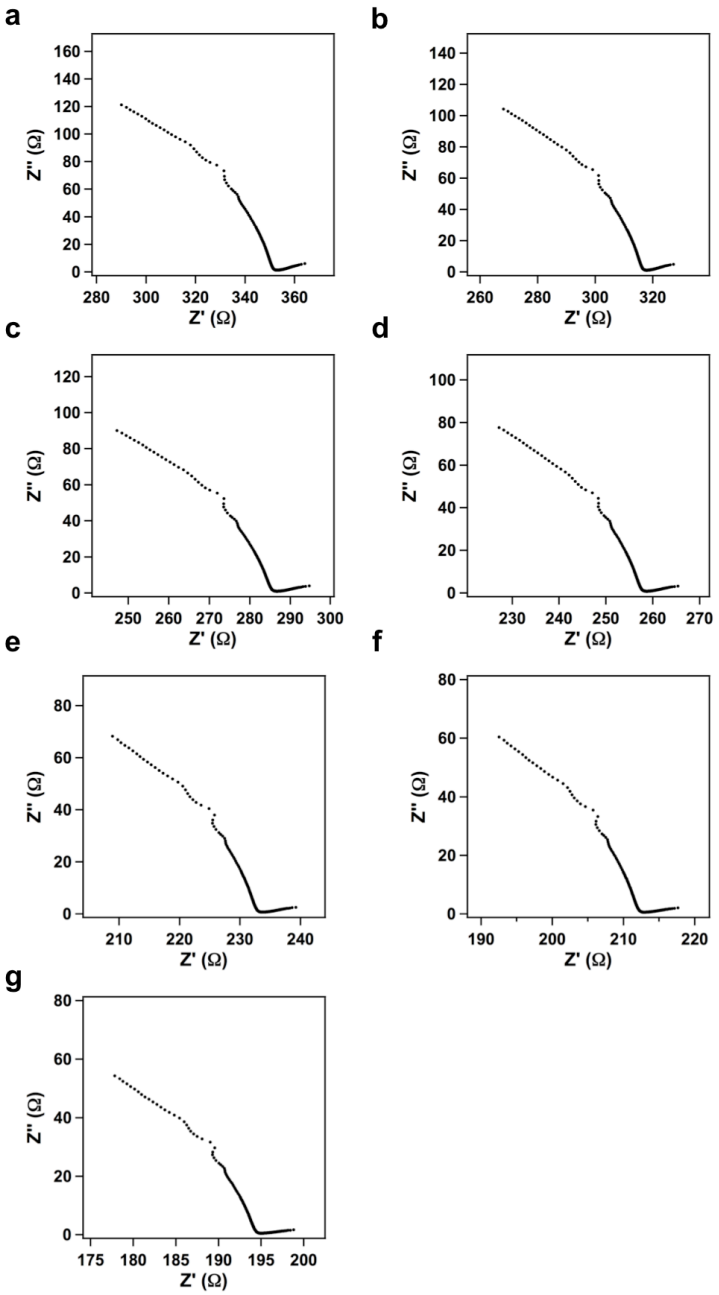

Figure 11. Nyquist plots of d_4-im@TPB-DMTP-COF at different temperatures of (**a**) 100 °C, (**b**) 105 °C, (**c**) 110 °C, (**d**) 115 °C, (**e**) 120 °C, (**f**) 125 °C and (**g**) 130 °C.

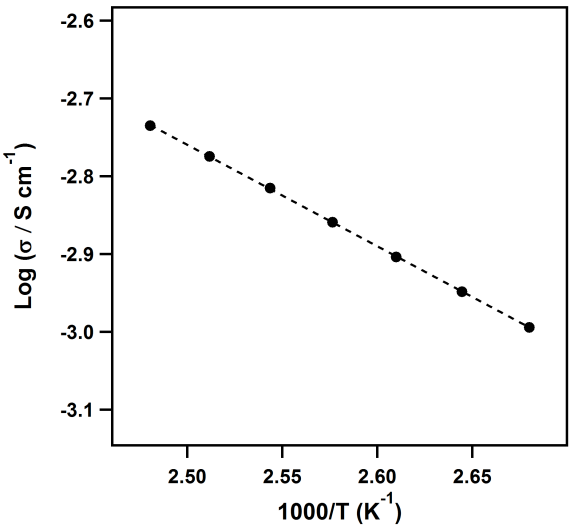

Figure 12. Temperature dependency of proton conductivities of d_4-im@TPB-DMTP-COF. Black dots are experimental data and black line is a curve-fitting plot.

The reduced proton conductivity for d_4-im@TPB-DMTP-COF could be ascribed to the isotopic influence of deuterium; deuterium has a twice fold of proton mass. Combined with the similar low activation energies, the isotopic effect confirms that conduction in the mesoporous channels is relied on the movement of protons other than the transport of imidazole molecules.

When the content of imidazole was reduced from the highest one to a half, the conductivity was decreased significantly. As shown in Figure 13, the proton conductivity of the im@TPB-DMTP-COF sample with a im content of 82 wt% was 2.03×10^{-4} S cm^{-1} at 130 °C. This low conductivity verifies the significance of im in the channels. To confirm the contribution of outer space to conductivity, another experiment was investigated by introducing 1,4-dimethoxybenzene to the COF (Fig. 14). Under the same condition, the conductivity of this COF sample was just 3.3×10^{-7} S cm^{-1} at 130 ˚C (Fig. 14). This result indicates the outside im has an ignored (0.0076%) contribution to the proton conductivity of COFs.

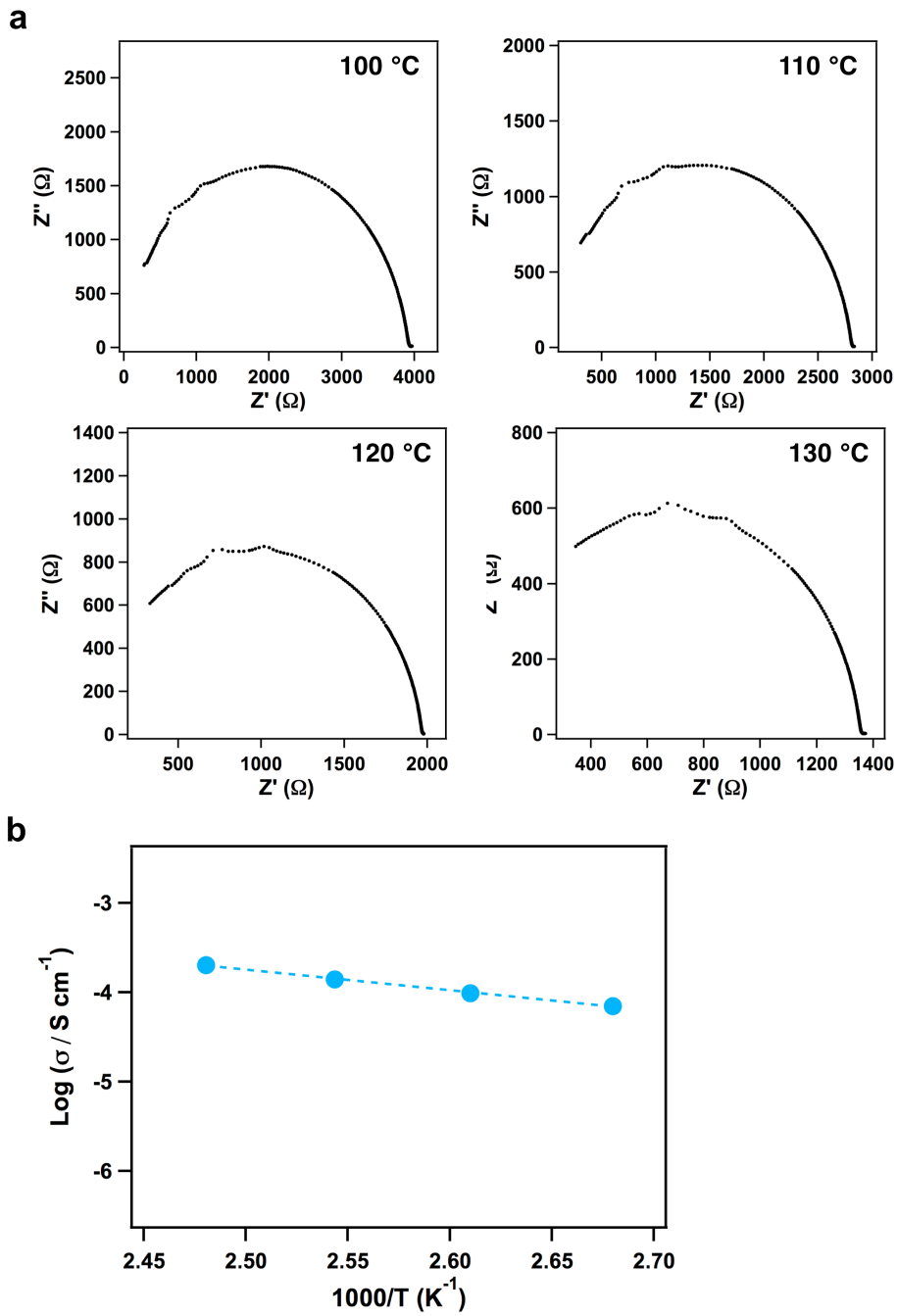

Figure 13. a, Nyquist plots of im@TPB-DMTP-COF with the im content of 84 wt% at different temperatures. **b,** Temperature dependency of proton conductivities of im@TPB-DMTP-COF with im content of 84 wt% (blue).

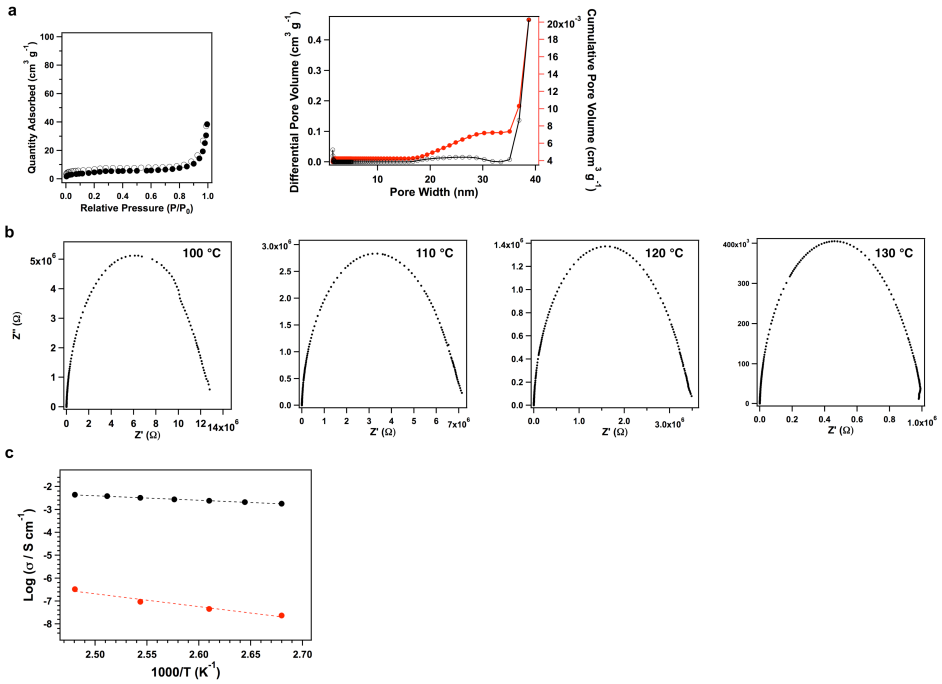

Figure 14. a, Nitrogen sorption curves (left) and pore size distribution profiles (right) of 1,4-dimethoxybenzene loaded TPB-DMTP-COF. **b,** Nyquist plots of the mixture of im with 1,4-dimethoxybenzene loaded TPB-DMTP-COF at different temperatures. **c,** Temperature dependency of proton conductivities of the mixture of im with 1,4-dimethoxybenzene loaded TPB-DMTP-COF (red dots), in comparison with im@TPB-DMTP-COF (black dots).

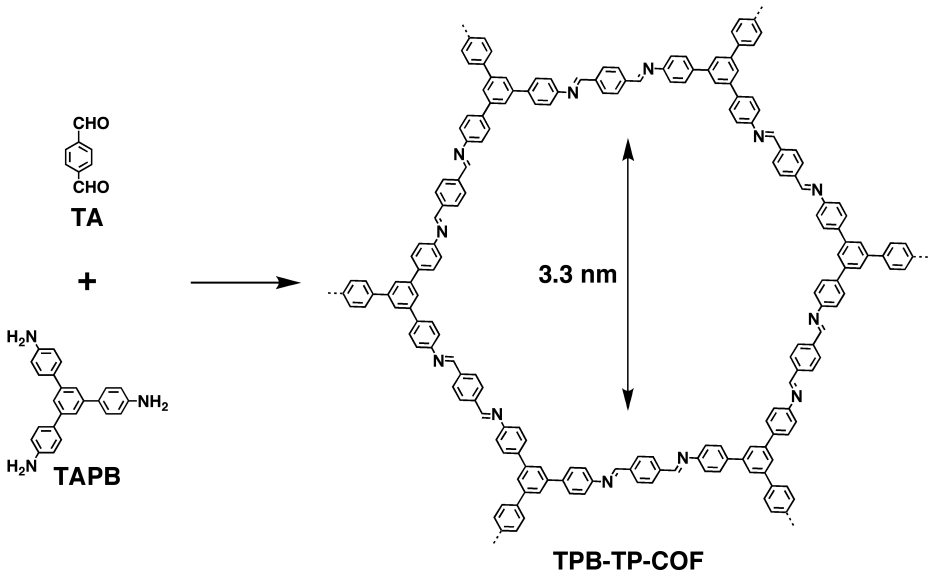

Figure 15. Schematic of TPB-TP-COF.

TPB-TP-COF was synthesized to further confirm the significance of the 1D mesoporous for proton conduction (Fig. 15). TPB-TP-COF has a BET surface area of 13 m^2 g^{-1} and a pore volume of 0.142 cm^3 g^{-1} (Fig. 4, purple curve). At 120 °C, the proton conductivity was only 4.71×10^{-7} S cm^{-1}. Temperature-dependent impedance measurements revealed that the activation energy was 0.91 eV for the proton conduction in im@TPB-TP-COF. The high-energy barrier suggests the proton conduction is largely hindered (Fig. 16 and Fig. 17). These results indicate that the long-range ordered 1D channels facilitate proton conduction.

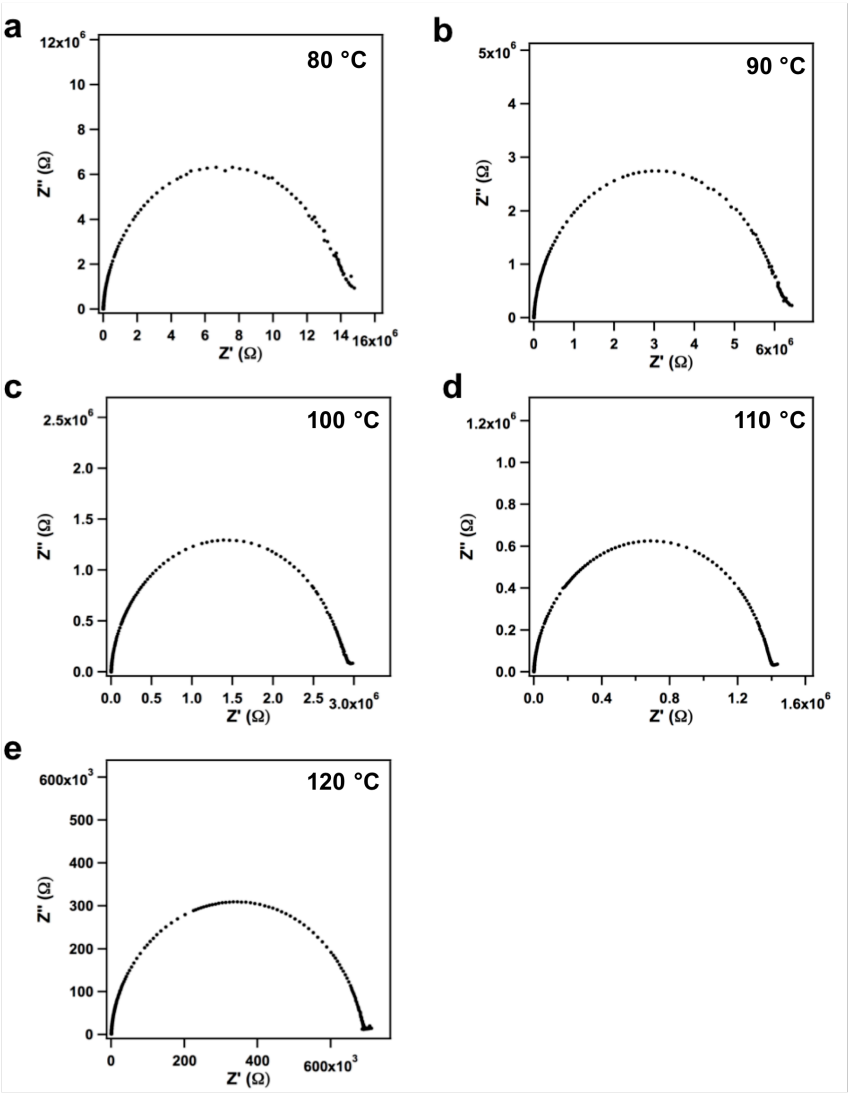

Figure 16. Nyquist plots of im@TPB-TP-COF at different temperatures.

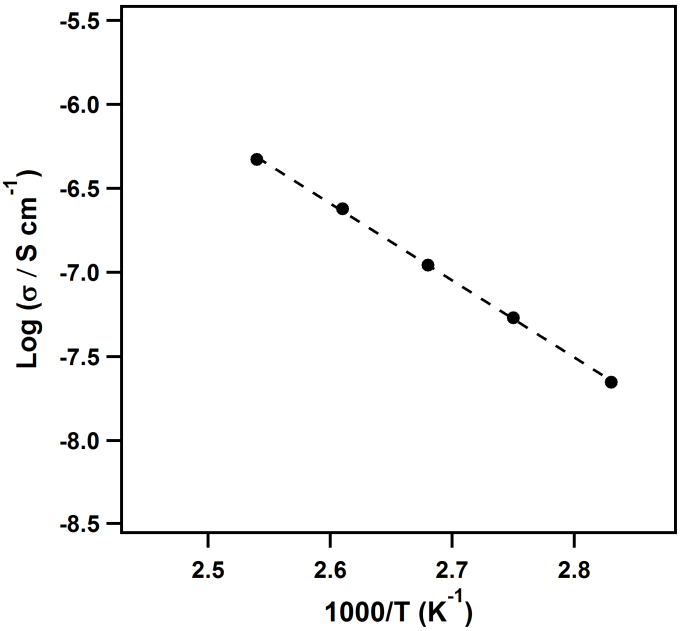

Figure 17. Temperature dependency of proton conductivities of im in TPB-TP-COF.

3.3 Conclusion

By developing COFs with high stability, crystallinity, and porosity, I have successfully demonstrated the strategy for designing COFs for proton conduction by exploring the ordered 1D mesopores. The results revealed that mesopores are key to proton conductions. The mesoporous channels increase the accommodation of proton carriers, facilitate the proton conductivity, and reduce the activation energy. These results suggest that COFs can provide a novel platform for proton conduction.

3.4 Experimental Sections

3.4.1 Methods

All the PXRD data were collected from 2θ = 1.0° to 30° by the Rigaku RINT Ultima III diffractometer with a 0.02° increment step. At 77 K, N_2 sorption isotherms were conducted via a 3Flex surface characterization analyzer with the Micrometrics Instrument Corporation model. The specific surface areas were evaluated using the Brunauer-Emmett-Teller (BET) method. The TGA measurements were performed on a Mettler-Toledo model TGA/SDTA851e, from 25 to 800 °C with a 10 °C min^{-1} enhancement rate under N_2.

3.4.2 Impedance Spectroscopy

Impedance analyses were performed on proton carrier loaded COF powders. All pellets were prepared via grinding the samples into a homogeneous powder with a mortar and pestle. The powders (about 300 mg) were added into a 10 mm standard die and then slowly increased pressure to 100 kN and kept for 30 min. Measurements were performed using an impedance analyzer (IM3570, HIOKI E. E. Co.), with a two-Ag-probe over the frequency range from 4 Hz to 5 MHz and with an input voltage amplitude of 100 mV. The cell was filled with nitrogen before conducting the measurements. The proton conductivities were obtained from equation: $\sigma = L/(Z \times A)$, where conductivity (S cm^{-1}) was represented by σ, thickness of sample (cm) was showed by L, electrode area (cm^2) was represented by A and impedance (Ω) was indicated by Z.

3.4.3 Fenton's Test

The COF sample (50 mg) was kept in 20 mL Fenton's reagent (3% H_2O_2, 3 ppm Fe (II)) for one day. Then the samples were Soxhelt with THF, and dried under vacuum at 120 °C for 12 h.

3.4.4 Materials and Synthetic Procedures

1,3,5-Tri(4-aminophenyl) benzene (TAPB), 1,2,4-triazole, imidazole, and 1,4-dimethoxybenzene were bought from TCI as received. *o*-Dichlorobenzene (*o*-DCB), tetrahydrofuran (THF), and *N, N*-dimethylformide (DMF) were bought from Kanto Chemicals. CH_3COOH, 1-butanol, mesitylene, and dioxane were bought from Wako Chemicals. 2,5-Dimethoxyterephthalaldehyde (DMTA) was synthesized according to the reported methods.[28]

Synthesis of TPB-TP-COF

The monomers of TAPB (0.080 mmol, 28.1 mg) and TA (0.120 mmol, 16.1 mg), a solvent mixture *o*-DCB/BuOH (0.5 mL/0.5 mL), and CH_3COOH catalyst (0.1 mL, 6 M) were added into in a Pyrex tube (10 mL). The tube was degassed through three freeze–pump–thaw cycles and sealed by flame and heated at 120 °C for 72 h. The

precipitate was collected by centrifugation, washed with THF for 6 times and then subjected to Soxhlet extraction with THF for 24 h. The powder was collected and dried at 120 °C under vacuum overnight to give TPB-TP-COF in an isolated yield of 83%.

Synthesis of trz@TPB-DMTP-COF

TPB-DMTP-COF was degassed under vacuum in a 10-mL tube and was added with 1,2,4-triazole (trz). The tube was degassed for 30 min and sealed to keep at 150 °C overnight to yield trz@TPB-DMTP-COF.

Synthesis of im@TPB-DMTP-COF

TPB-DMTP-COF was degassed under vacuum in a 10-mL tube and was added with imidazole (im). The tube was degassed for 30 min and sealed to keep at 150 °C overnight to yield im@TPB-DMTP-COF.

TPB-DMTP-COF introduced with 1,4-Dimethoxybenzene

TPB-DMTP-COF was degassed under vacuum in a 10-mL tube and was added with 1,4-Dimethoxybenzene. The tube was degassed for 30 min and sealed to keep at 150 °C overnight to yield 1,4-dimethoxybenzene@TPB-DMTP-COF.

Preparation of mixture of im and TPB-DMTP-COF

TPB-DMTP-COF (180 mg) was ground with im (9.36 mg) into a homogeneous powder, and the resulted mixture was added to the holder and was pressed under slowly increased pressure and kept at 100 kN for 30 min.

3.5 References

[1] Higashihara, T.; Matsumoto, K.; Ueda, M. *Polymer* **2009**, 50, 5341.

[2] Fang, J.; Guo, X.; Harada, S.; Watari, T.; Tanaka, K.; Kita, H.; Okamoto, K.; *Macromolecules* **2002**, 35, 9022.

[3] Xing, P.; Robertson, G. P.; Guiver, M. D.; Mikhailenko, S. D.; ; Kaliaguine, S. S *Macromolecules* **2004**, 37, 7960.

[4] Mader, J. A.; Benicewicz, B. C. *Macromolecules* **2010**, 43, 6706.

[5] Matsumoto, K.; Higashihara, T.; Ueda, M. *Macromolecules* **2009**, 42, 1161.

[6] Shimizu, G. K.; Taylor, J. M.; ; Kim, S. *Science* **2013**,341, 354.

[7] Horike, S.; Umeyama, D.; Kitagawa, S. *Acc. Chem. Res.* **2013**, 46, 2376.

[8] Yoon, M.; Suh, K.; Natarajan, S.; Kim, K. *Angew. Chem. Int. Ed.* **2013**, 52, 2688.

[9] Xu, G.; Otsubo, K.; Yamada, T.; Sakaida, S.; Kitagawa, H. S *J. Am. Chem. Soc.* **2013**, 135, 7438.

[10] Jeong, N. C.; Samanta, B.; Lee, C. Y.; Farha, O. K.; Hupp, J. T. *J. Am. Chem. Soc.* **2012**, 134, 51.

[11] Maffeo, C.; Bhattacharya, S.; Yoo, J., Wells, D.; Aksimentiev, A. *Chem. Rev.* **2012**, 112, 625.

[12] Mauritz, K. A.; Moore, R. B. *Chem. Rev.* **2004**,104, 4535.

[13] Schmidt-Rohr, K.; Chen, Q. *Nat. Mater.* **2008**, 7, 75.

[14] Xu, H.; Jiang, D. *Nat. Chem.* **2014**, 6, 564.

[15] Bureekaew, S.; Horike, S.; Higuchi, M.; Mizuno, M.; Kawamura, T.; Tanaka, D.; Yanai, N.; Kitagawa, S. *Nat. Mater.* **2009**, 8, 831.

[16] Hurd, J. A.; Vaidhyanathan, R.; Thangadurai, V.; Ratcliffe, C. I.; Moudrakovski, I. L.; Shimizu, G. K. H. *Nat. Chem.* **2009**, 1, 705.

[17] Feng, X.; Ding, X.; Jiang, D. *Chem. Soc. Rev.* **2012**, 41, 6010.

[18] Cote, A. P.; Benin, A.I.; Ockwig, N. W.; O'Keeffe, M.; Matzger, A. J.; Yaghi, O. M. *Science* **2005**, 310, 1166.

[19] Colson, J. W.; Woll, A. R.; Mukherjee, A.; Levendorf, M. P.; Spitler, E. L.;

[20] Chandra, S.; Kundu, T.; Kandambeth, S.; BabaRao, R.; Marathe, Y.; Kunjir, S. M.; Banerjee, R. *J. Am. Chem. Soc.* **2014**, 136, 6570.

[21] Kuhn, P.; Antonietti, M.; Thomas, A. *Angew. Chem. Int. Ed.* **2008**, 47, 3450.

[22] Zhu, X.; Tian, C.; Mahurin, S. M.; Chai, S.H.; Wang, C.; Brown, S.; Veith, G. M.; Luo, H.; Liu, H.; Dai, S. *J. Am. Chem. Soc.* **2012**, 134, 10478.

[23] Xu, H.; Gao, J.; Jiang, D. *Nat. Chem.* **2015**, 7, 905.

[24] DeBlase, C. R.; Hernández-Burgos, K.; Silberstein, K. E.; Rodríguez-Calero, G. G.; Bisbey, R. P.; Abruña, H. D.; Dichtel, W. R. *ACS Nano* **2015**, 9, 3178.

[25] Medina, D. D.; Rotter, J. M.; Hu, Y.; Dogru, M.; Werner, V.; Auras, F.; Markiewicz, J. T.; Knochel, P.; Bein, T. *J. Am. Chem. Soc.* **2015**, 137, 1016.

[26] Kawada, W.; McGhie, A. R.; Labes, M. M. *J. Chem. Phys.* **1970**, 52, 3121.

[27] Li, S.; Zhou, Z.; Zhang, Y.; Liu, M. *Chem. Mater.* **2005**, 17, 5884.

[28] Kuhnert, N.; Rossignoloa, G. M.; Lopez-Periagoa, A. *Org. Biomol.Chem.* **2003**, 1, 1157.

Chapter 4

High Proton Conduction in Crystalline Covalent Organic Frameworks with Phosphoric Acid Proton Carriers

To be Submitted

Shanshan Tao, Hong Xu, Lipeng Zhai, Qiuhong Chen and Donglin Jiang

Abstract

The content of proton carriers in COFs is important for proton conduction. The content of H_3PO_4 (PA) in previous reports was limited; in this chapter I selected PA crystals, increased the PA content to the theoretical loading levels according to the pore volumes of TPB-DMTP-COF and TPB-DMPTA-COF and the density of PA, and prepared PA@TPB-DMTP-COF with a PA content of 225.8 wt% and PA@TPB-DMPTA-COF with a PA content of 269.6 wt%, respectively. I measured the proton conductivity of these COF samples under anhydrous conditions. PA@TPB-DMPTA-COF exhibited a proton conductivity by one order of magnitude up to 10^{-1} S cm^{-1} at 160 °C. These results suggest the potential of COFs for applications in fuel cells.

4.1 Introduction

Fuel cells supply electric energy with high efficiencies compared with those of internal combustion engine systems, which are limited by Carnot cycle.[1] The humidification part is very necessary for the fuel cells which currently used nafion membranes, and the cost is expensive due to the demanding humidification of the inlet gas.[2] Thus the development of high temperature membranes that enable working at higher temperature (between 100 and 200 °C) and at a relative low humidity are highly desired.[2,3] Phosphoric acid (PA) is one of the highest inherent proton conductivity materials (10^{-1} S cm^{-1}). PA with the distinct self-ionization and self-dehydration mechanism for proton conduction makes it possible to achieve excellent proton conductivity under anhydrous conditions. PA-doped PBI membranes have been widely studied for high proton conductivity (10^{-2} S cm^{-1}).[2] The porous PBI with excess PA shows one to two orders of magnitude higher conductivity than those of the nonporous PBI.[4] This result indicates that porous material doped with PA might have better performance in proton conductivity. Porous materials have displayed considerable opportunities for designing new generation proton-conducting materials through exploring their ordered porous structures.[5-11] COFs are a class of unique porous polymer with permanent pores and have demonstrated many properties such as gas adsorption, catalysis, semiconducting, charge carrier transport, photoconduction, sensing, and energy storage.[12,13] However, these porous materials have not been well developed for proton conduction using PA as proton carriers.[15,16]

COFs with imine linkage have excellent crystallinity and robust chemical and thermal stabilities, thus having potential applications in fuel cells. Operations above 100 °C have several advantages. High temperature can create faster kinetics, increase the tolerance of the catalyst palladium to carbon monoxide, and can use the less purity hydrogen. At the same time, there is no need of the humidification system, which can greatly reduce the cost of the fuel cell.

The content of the proton carriers plays a vital role in the proton conductivity in solid-state material. The content of PA in previous reports was quite small; in this

chapter, the PA@TPB-DMTP-COF has a PA content of 225.8 wt% and PA@TPB-DMPTA-COF has a PA content of 269.6 wt%, respectively. PA@TPB-DMTP-COF exhibited a proton conductivity of 10^{-2} S cm^{-1} at 160 °C. The conductivity at 120 °C was two fold as high as that of the best COF system, i.e. PA@TpBpy-Mc.[15] The cycle performance at 160 °C after 48 h revealed that the COFs retained 90% conductivity. PA@TPB-DMPTA-COF exhibited a proton conductivity by one order of magnitude up to 10^{-1} S cm^{-1} at 160 °C. Notably, this conductivity is the highest one among PA-loaded COFs and MOFs.

In this study, I investigated the proton conduction of PA across the mesoporous channels of two different COFs with high crystallinity and large pore volume.

4.2 Results and Discussions

4.2.1 Synthesis and Structural Characterizations

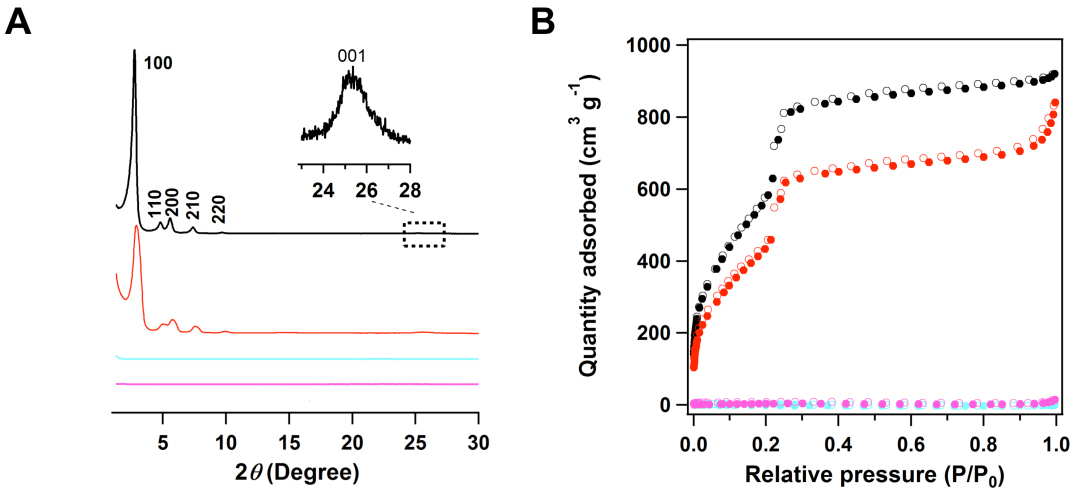

Figure 1. (**A**) Powder XRD figures TPB-DMTP-COF (black curve), PA treated COF and then removed PA (red curve), PA@TPB-DMTP-COF with a PA content of 225.8 wt% (blue curve) and PA@TPB-DMTP-COF with a PA content of 112.9 wt% (magenta curve). (**B**) Isotherm curves of TPB-DMTP-COF (black curve), PA treated TPB-DMTP-COF and then removed PA (red curve), PA@TPB-DMTP-COF with a PA content of 225.8 (blue curve) and PA@TPB-DMTP-COF with a PA content of 112.9 wt% (magenta curve).

The PXRD pattern of TPB-DMTP-COF was described in the previous paper.[14] (Fig. 1A, black curve). The typical-IV isotherm curve of TPB-DMTP-COF indicates the formation of mesoporous channels (Fig. 1B, black curve). The pore size is 3.26 nm. [14]

The chemical and thermal stabilities of TPB-DMTP-COF were reported in previous chapter. It showed excellent chemical stability in different kinds of organic solvents and harsh conditions[14]. As PA was employed as carrier, I investigated the stability by dispersing COFs into a PA solution for seven days. After washing out PA, TPB-DMTP-COF could retain its structure (Fig. 1A and B, red curve).

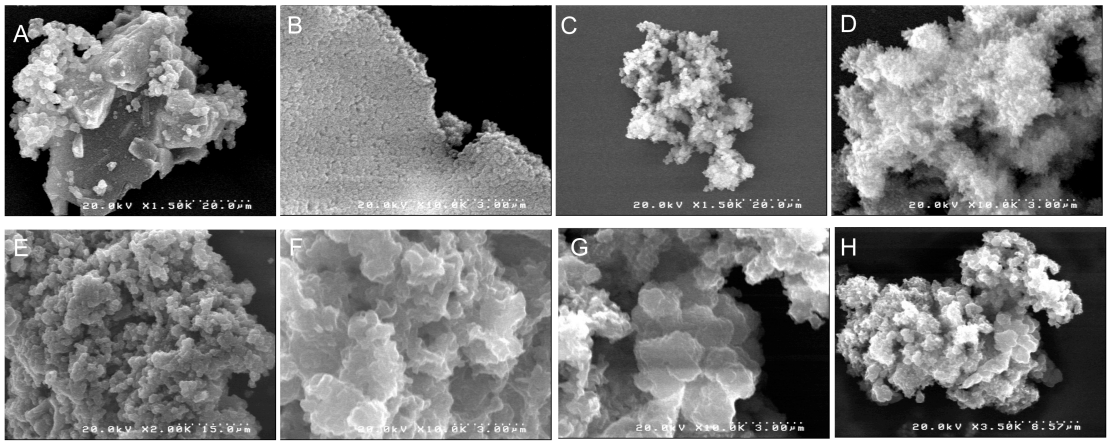

Figure 2. FE SEM images of of TPB-DMTP-COF (**A**, **B**), PA@TPB-DMTP-COF (**C**, **D**) and those after removing PA from PA@TPB-DMTP-COF (E-H).

The FE SEM images indicate that after introducing PA into TPB-DMTP-COF, it could keep its structural integrity (Fig. 2C-D). The morphology of COFs could be retained, while increasing the content of PA results in more flat surface.

4.2.2 Impedance Spectroscopy

TPB-DMTP-COF could introduce PA into channels with the highest content of 225.8 wt% according to the pore volume of COF. The PXRD curve (Fig. 1A blue curve) showed that the intensity of the (110) facet reduced significantly, which indicates the loading of proton carriers PA into the channels of COFs. The BET surface area of TPB-DMTP-COF was 2072 m^2 g^{-1}, however, after loading PA, there

was almost no BET surface area (Fig. 1B blue curve) left. These results manifest that the guest molecules occupy the mesopores of TPB-DMTP-COF. Because PA is highly hydroscopic, it easily adsorbs water. Moreover, PA tends to be self-polymerized. These factors make it hard to evaluate the exact content from TGA curves (Fig. 3, blue curve). The exact content of PA in PA@ TPB-DMTP-COF was checked by using the reaction of PO_4^{-3} as shown below.

$$PO_4^{3-} + 12\ MoO_4^{2-} + 24\ H^+ = (NH_4)_3PO_4 \cdot 12MoO_3\downarrow + 12\ H_2O$$

From the weight of $(NH_4)_3PO_4 \cdot 12MoO_3$, the content of PA was evaluated to be 95% of the initial mass of PA.

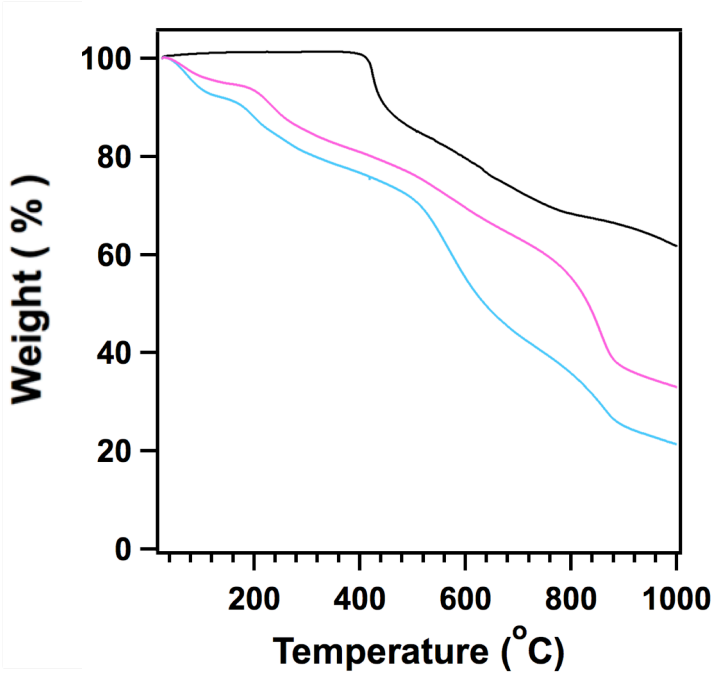

Figure 3. TGA of TPB-DMTP-COF (black curve), PA@TPB-DMTP-COF (blue curve) and PA@TPB-DMTP-COF with a PA content of 112.9 wt% (magenta curve) under N_2 atmosphere.

TPB-DMTP-COF itself possessed inappreciable proton conductivity less than 10^{-12} S cm^{-1}, therefore it could serve as insulators and separators to partition H_2 and O_2.[11] The proton conduction experiments were conducted by the alternating-current impedance spectroscopy. The conductivity of PA@TPB-DMTP-COF was

investigated under anhydrous conditions. These impedance plots are emblematic of primarily ionic conduction. The semicircle with a characteristic spur at lower frequency indicates the blocking of protons at Ag electrodes. The proton conductivity of the sample was calculated from equation $\sigma = L/Z/A$, where σ represented the conductivity (S cm^{-1}), L showed the measured sample thickness (cm), A manifested the electrode area (cm^2), and Z indicated the impedance (Ω).

According to the temperature-dependent profiles, the activation energy for the proton conduction of PA@TPB-DMTP-COF was determined and the value implies a Grotthuss-hopping mechanism. A 50-h-continuous run at 160 °C was also conducted and revealed a slightly decrease in conductivity.

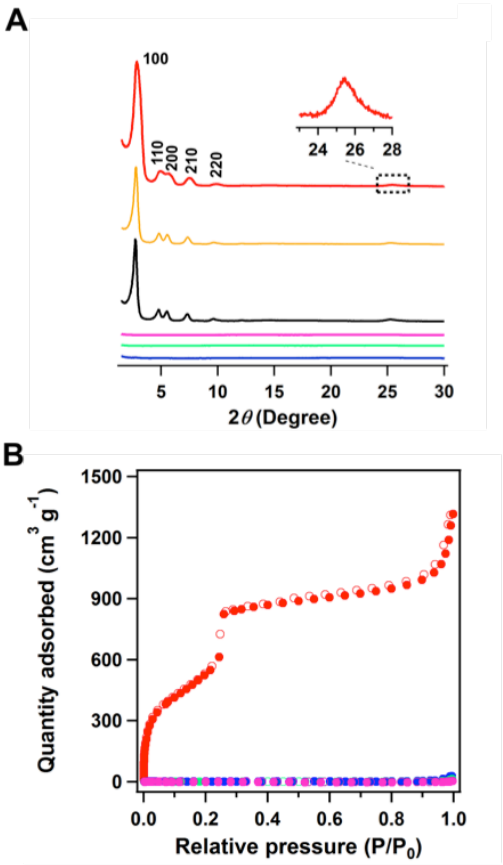

Figure 4. (**A**) PXRD patterns of TPB-DMPTA-COF (red line), PA@TPB-DMPTA-COF with a PA content of 269.6 wt% (magenta line),

PA@TPB-DMPTA-COF with a PA content of 202.2 wt% (green line) and PA@TPB-DMPTA-COF with a PA content of 134.8 wt% (blue line), PA treated TPB-DMPTA-COF and the removed PA (brown curve), Fenton oxidation of TPB-DMPTA-COF (black curve). (**B**) Nitrogen sorption isotherm profiles of TPB-DMPTA-COF (red curve), PA@TPB-DMPTA-COF with a PA content of 269.6 wt% (magenta curve), PA@TPB-DMPTA-COF with a PA content of 202.2 wt% (green curve) and PA@ TPB-DMPTA-COF with a PA content of 134.8 wt% (blue curve).

A newly synthesized TPB-DMPTA-COF was investigated to show the generality of this approach. The characterization of this COF including crystal structure and porosity was described in the thesis of Lipeng Zhai. According to the pore volume, TPB-DMPTA-COF could intake PA to the channels with the highest content of 269.6 wt%. After loading PA, both the crystallinity and porosity vanished, showing a similar tendency as that of PA@TPB-DMPT-COF (Fig. 4). These results showed that the guest molecules occupied the channels of TPB-DMPTA-COF. Because PA was employed as the proton carrier, I dispersed TPB-DMPTA-COF in PA solution for one week and washed out PA, the COF could still retain its crystallinity (Fig. 4A brown curve). The Fenton reagent test results also demonstrated that TPB-DMPTA-COF could retain its crystallinity (Fig. 4A black curve). The morphology of TPB-DMPTA-COF (Fig. 5A) did not have a significant change after removing the PA (Fig. 5F).

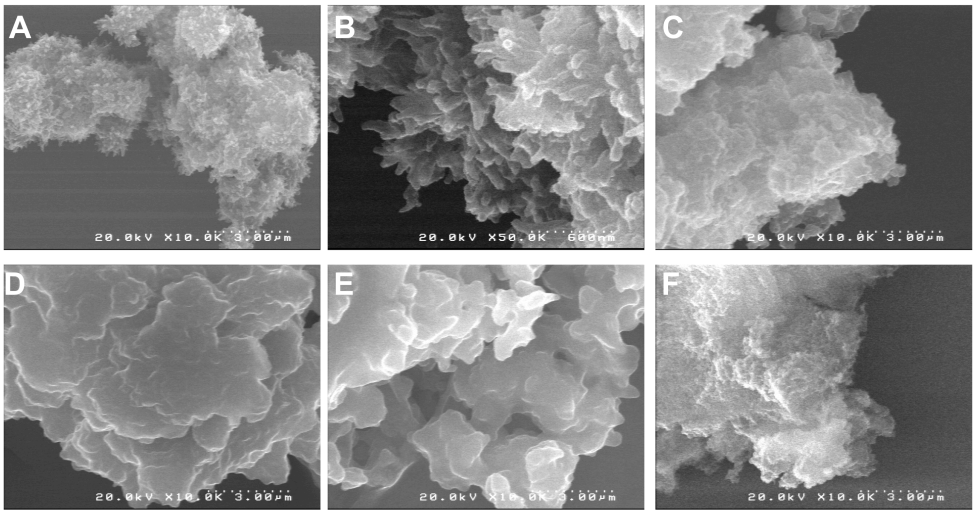

Figure 5. SEM images of TGA of TPB-DMPTA-COF (**A**, **B**), PA@TPB-DMPTA-COF with a PA content of 134.8 wt% (**C**), PA@TPB-DMPTA-COF with a PA content of 202.2 wt% (**D**), PA @TPB-DMPTA-COF with a PA content of 269.6 wt% (**E**), PA treated TPB-DMPTA-COF and the removed PA (**F**).

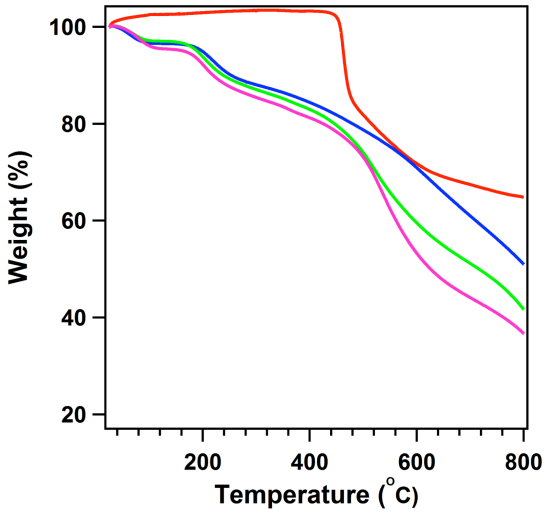

Fig. 6. TGA of TPB-DMPTA-COF (red curve), PA@TPB-DMPTA-COF with a PA content of 269.6 wt% (magenta curve), PA@TPB-DMPTA-COF with a PA content of 202.2 wt% (green curve) and PA@TPB-DMPTA-COF with a PA content of 134.8 wt% (blue curve) under N_2 atmosphere.

The proton conductivities of PA@TPB-DMPTA-COF were investigated in

different conditions. According to the temperature-dependent profiles, the activation energy was determined. And this low energy barrier suggests a Grotthuss-type mechanism for proton conduction in the 1D mesorporous channels of COFs.

To investigate the influence of the content of proton carriers on the conductivity of TPB-DMTP-COF, I reduced the content from the theoretical 225.8 wt% to 112.9 wt%, half of the highest content. The conductivities of PA@TPB- DMTP-COF with a PA content of 112.9 wt% were measured under the same conditions. These conductivities were much smaller than those of COFs with a theory-loading PA content. The activation energy was determined, and the value indicates that the proton motion is governed by a vehicle mechanism.

For TPB-DMPTA-COF, I reduced the PA content from 269.6 to 202.2 and 134.8 wt%. The proton conductivity decreased dramatically. The activation energy was also calculated from the experimental data. The proton conductivities of PA@ TPB-DMPTA-COF with a PA content of 134.8 wt% were also measured at the same condition and the activation energy was estimated. These comparative studies indicate the importance of PA content for proton conduction.

4.3 Conclusion

In summary, the proton conductivity was much higher than reported in which PA serves as the proton carrier in COFs.[15,16] Two reasons may account for the improved proton conductivity. First, the high pore volume allows for a high content of proton carriers and hence increases the conductivity.[17] Second, electrolyte used PA as proton carriers and the operations at high temperature also enhance the proton conductivity. These results suggest that COFs are promising as the polymer exchange materials in the fuel cells for proton conduction.

4.4 Experimental Sections

4.4.1 Materials and Methods

1,4-Dimethoxybenzene, butyllithium, 1,3,5-tri(4-aminophenyl) benzene (TAPB) were bought from TCI without further purification. *o*-Dichlorobenzene (*o*-DCB),

tetrahydrofuran (THF), bromine, and *N, N*-dimethylformide (DMF) were bought from Kanto Chemicals. CH_3COOH, 1-butanol, mesitylene and dioxane were bought from Wako Chemicals. From Sigma-Aldrich, phosphoric acid were bought. DMTA was prepared using the reported method.[18] The PXRD data were collected from $2\theta = 1.0°$ to 30° using the SmartLab diffractometer with a 0.02° increment step. At 77 K, N_2 sorption isotherms were conducted on a 3Flex surface characterization analyzer with the Micrometrics Instrument Corporation model. The specific surface areas were calculated by the Brunauer-Emmett-Teller (BET) method. The TGA measurements were measured on a Mettler-Toledo model TGA/SDTA851e, from 25 to 800 °C at a 10 °C min^{-1} rate under N_2.

4.4.2 Synthetic Procedures

Synthesis of TPB-DMPTA-COF. Firstly, I added monomers of TAPB (0.094 mmol, 32.7mg) and DMPTA (0.141 mmol, 22.8 mg) to 1-mL *o*-DCB/n-BuOH (1:1) mixture in a 10-mL Pyrex vial. Secondly I charged the tube with 0.1 mL 6 M CH_3COOH. Thirdly, I degassed and sealed the vial, then kept it for 72 h at 120 °C. Finally, I collected the precipitate by centrifugation, washed using Soxhlet extraction with THF, and dried the sample to yield TPB-DMPTA-COF.

4.5 References

[1] Hoffert,M. I.; Caldeira, K.; Benford, G.; Criswell, D. R.; Green,C.; Herzog, H.; Jain, A. K.; Kheshgi, H. S.; Lackner, K. S.; Lewis, J. S.; Lightfoot, H. D.; Manheimer, W.; Mankins, J. C.; Mauel, M. E.; Perkins, L. J.; Schlesinger, M. E.; Volk, T.; Wigley , T. M. L. *Science* **2002**, 298, 981.

[2] Zhang, H.; Shen, P. K. *Chem. Rev.* **2012**, 112, 2780.

[3] Gloukhovski, R.; Freger, V.; Tsur, Y. *Fuel Cells* **2016**, 16, 434.

[4] Weber, J.; Kreuer, K.-D.; Maier, J.; Thomas, A. *Adv. Mater.* **2008**, 20, 2595.

[5] Horike, S.; Umeyama, D.; Kitagawa, S. *Acc. Chem. Res.* **2013**, 46, 2376.

[6] Yoon, M.; Suh, K.; Natarajan, S.; Kim, K.*Angew. Chem. Int. Ed.* **2013**, 52, 2688.

[7] Hod, I.; Deria, P.; Bury, W.; Mondloch, J. E.; Kung, C. W.; So, M.; Sampson, M. D.; Peters, A.W.; Kubiak, C. P.; Farha, O. K.; Hupp, J. T. *Nat. Commun.* 2015, 6, 8304.

[8] Taylor, J. M.; Taylor, J. M.; Komatsu, T.; Dekura, S.; Otsubo, K.; Takata, M.; Kitagawa, H. *J. Am. Chem. Soc.* **2015**, 137, 11498.

[9] Liang, X.; Zhang, F.; Feng, W.; Zou, X.; Zhao, C.; Na, H.; Liu, C.; Sun, F.; Zhu, G. *Chem. Sci.* **2013**, 4, 983.

[10] Xu, G.; Otsubo, K.; Yamada, T.; Sakaida, S.; Kitagawa, H. *J. Am. Chem. Soc.* **2013**, 135, 7438.

[11] Xu, H.; Tao, S.; Jiang, D. *Nat. Mater.* **2016**, 15, 722.

[12] Feng, X.; Ding, X.; Jiang, D. *Chem. Soc. Rev.* **2012**, 41, 6010.

[13] Huang, N.; Wang, P.; Jiang, D. *Nat. Rev. Mater.* **2016**, 1, 16068.

[14] Xu, H.; Gao, J.; Jiang, D. *Nat. Chem.* **2015**, 7, 905.

[15] Chandra, S.; Kundu, T.; Kandambeth, S.; BabaRao, R.; Marathe, Y.; Kunjir, S. M.; Banerjee, R. *J. Am. Chem. Soc.* **2014**, 136, 6570.

[16] Shinde, D. B.; Aiyappa, H. B. Bhadra, M.; Biswal, B. P.; Wadge, P.; Kandambeth, S.; Garai, B.; Kundu, T.; Kurungot, S.; Banerjee, R. *J. Mater. Chem. A* **2016**, 4, 2682.

[17] Hurd, J. A.; Vaidhyanathan, R.; Thangadurai, V.; Ratcliffe, C. I.; Moudrakovski, L.; Shimizu, G. K. H. *Nat. Chem.* **2009**, 1, 705.

[18] Kuhnert, N.; Rossignoloa, G. M.; Lopez-Periagoa, A. *Org. Biomol.Chem.* **2003**, 1, 1157.

Chapter 5

Design and Synthesis of Large Pore Covalent Organic Frameworks for Proton Conduction

To be submitted

Shanshan Tao, Hong Xu and Donglin Jiang

Abstract

In this chapter, I explored the scope of COFs by developing different building blocks for the construction of imine-linked large-pore COFs. The COFs with different kinds of pore shapes and pore sizes were investigated for proton conduction. Based on these COFs, I explored the relationship between proton conduction and pore size and pore structures.

5.1 Introduction

Well-organized molecular systems appeal even increasing popularity and are crucial in many applications such as electronic, optoelectronic, and photovoltaic devices. COFs are one of the crystalline porous polymers with structural orderings and permanent pores that permit the atomically pinpoint integration of organic units into extended structure with periodic skeletons and well-organized nanaochannels.[1,8-11] COFs have demonstrated potential in the applications of gas storage and separation, catalyst and photovoltaic devices.[2] However, the potential of COFs in polymer exchange membrane has not been well explored. Over the past fifty years, researchers have paid great attention on polymers for proton condcution.[3-7] However, the intricate polyelectrolyte systems are difficult to achieve ordered structures that have hampered any implementation.

Recently, microporous materials with inherent pores such as MOFs[12-16] have been extensively investigated. For instance, MOFs have shown proton conduction with *N*-heterocyclic proton carriers,[17,18] i.e. imidazole (im) or triazole (trz). However, the use of mesopore is ignored by a prejudice that mesopore will lead to the flow of proton carrier molecules instead of proton itself.

In chapters 3 and 4, I have demonstrated different kinds of COFs for proton conduction. However, the pore size of the previous reported COFs or MOFs are less than 4 nm, the design of large-pore COFs and the relationship between the pore size and proton conduction have not been investigated. In this chapter, the author presents another pathway to the structural control by taking advantage of different linkers and knots to build different COFs with large pores and investigated the relationship between proton conduction and pore structures.

5.2 Design and Synthesis of TPB-TMDPDA-COF

TPB-TMDPDA-COF was synthesized by the polycondensation of TPB and new monomer TMDPDA under solvothermal condition.

5.2.1 Characterize of TPB-TMDPDA-COF

In the PXRD profile, TPB-TMDPDA-COF exhibited six diffraction peaks with positions at 2.26°, 3.96°, 4.62°, 6.10°, 8.10°, 10.10°, and 23.5°; these peaks were ascribed to the (100), (110), (200), (210), (220), and (001) facets (Fig. 1, green curve). Using the optimal monolayer structure, AA and staggered AB stacking modes were generated and optimized. In the stacked frameworks, TPB-TMDPDA-COF adopts AA stacking mode. The simulated data were list in Appendix Table 9-11.

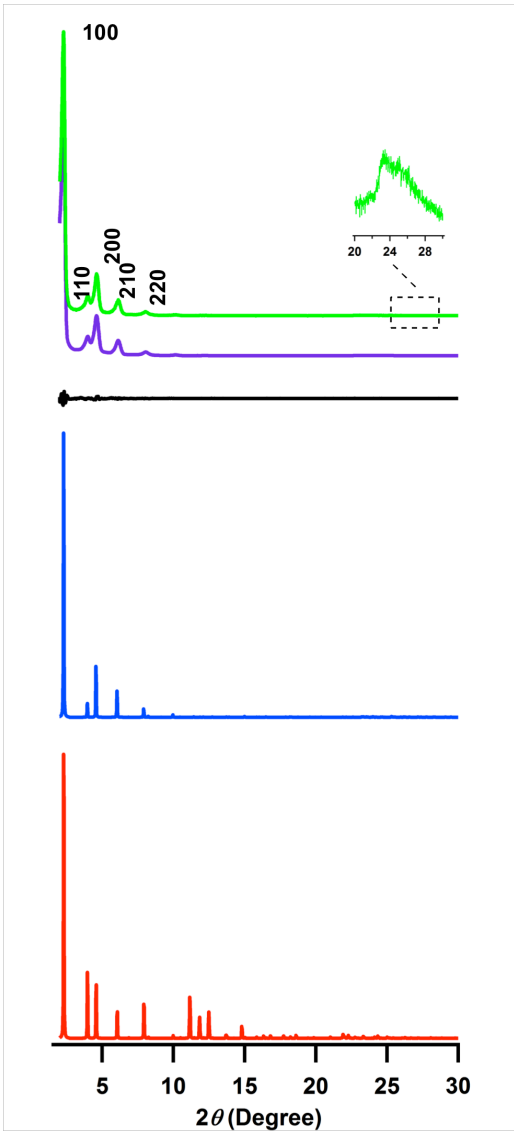

Figure 1. PXRD profiles of TPB-TMDPDA-COF. Experimentally observed (green), Pawley refined (purple) and their difference (black), simulated using the AA stacking mode (blue) and the staggered AB stacking mode (red).

Nitrogen-sorption isotherms of TPB-TMDPDA-COF measured at 77 K and displayed a representative type-IV shape, which is typical of a mesoporous material (Fig. 2a). The BET surface area was 1657 m^2 g^{-1}. From Figure 2b, TPB-TMDPDA-COF has a pore size of 3.85 nm (Fig. 2b, red curve) and a pore volume of 1.31 cm^3 g^{-1} (black curve).

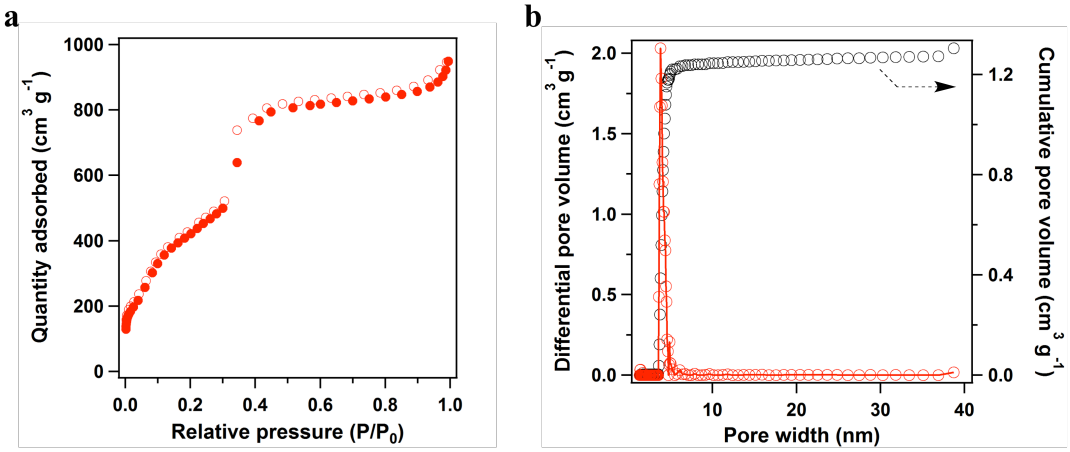

Figure 2. (**a**) Nitrogen isotherm curves of TPB-TMDPDA-COF, (**b**) Pore size (red), TPB-TMDPDA-COF's pre size distribution (black).

TPB-TMDPDA-COF samples were dispersed into harsh conditions for one week to investigate the chemical stability. Redox stability was also studied in Fenton reagents for 24 h. From the small changes in intensities and no variation in positions in its PXRD curves, TPB-TMDPDA-COF keeps its original crystalline structure under such rigorous conditions. The BET surface areas were 1031, 1190, 1598 and 1075 m^2 g^{-1} for the COF samples after treated in water (100 °C) (Fig. 3b, brown curve), strong acid (Fig. 3b, blue curve), strong base (Fig. 3b, purple curve) and Fenton reagents for 24 h (Fig. 3b, black curve), respectively. From Figure 4, the TGA curve indicates that TPB-TMDPDA-COF does not show weight loss under N_2 before 400 °C. The morphology of TPB-TMDPDA-COF assumes pellet aggregates (Fig. 5).

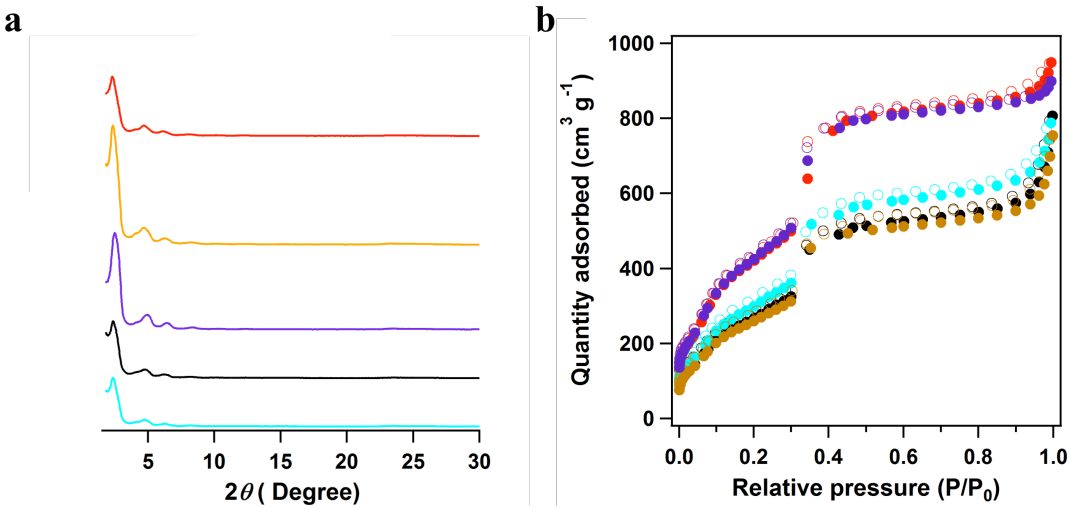

Figure 3. (**a**), PXRD patterns and (**b**), N_2 sorption curves of TPB-TMDPDA-COF upon one week treatment in different solvents: as synthesized (red curve), H_2O (100 °C) (brown curve), NaOH (14 M) (purple curve), HCl (12 M) (blue curve); Fenton reagents (24 h) (black curve). Color in b is the same as that in a.

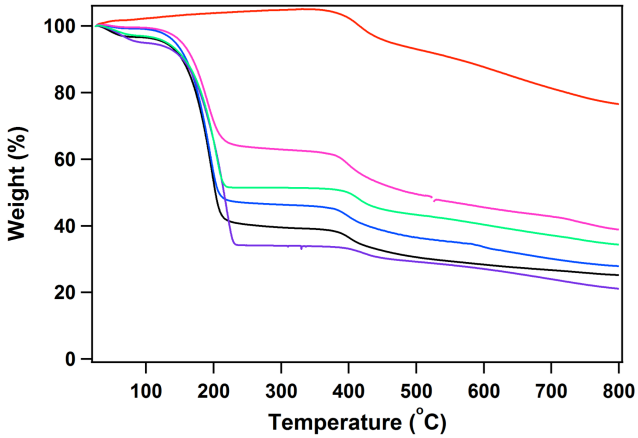

Figure 4. TGA curve of TPB-TMDPDA-COF (red curve), im@TPB-TMDPDA-COF (blue curve), d_4-im@TPB-TMDPDA-COF (black curve), trz@TPB-TMDPDA-COF (purple curve), im@TPB-TMDPDA-COF with the im content of 81 wt% (magenta curve), trz@TPB-TMDPDA-COF with the trz content of 91 wt% (green curve) under N_2.

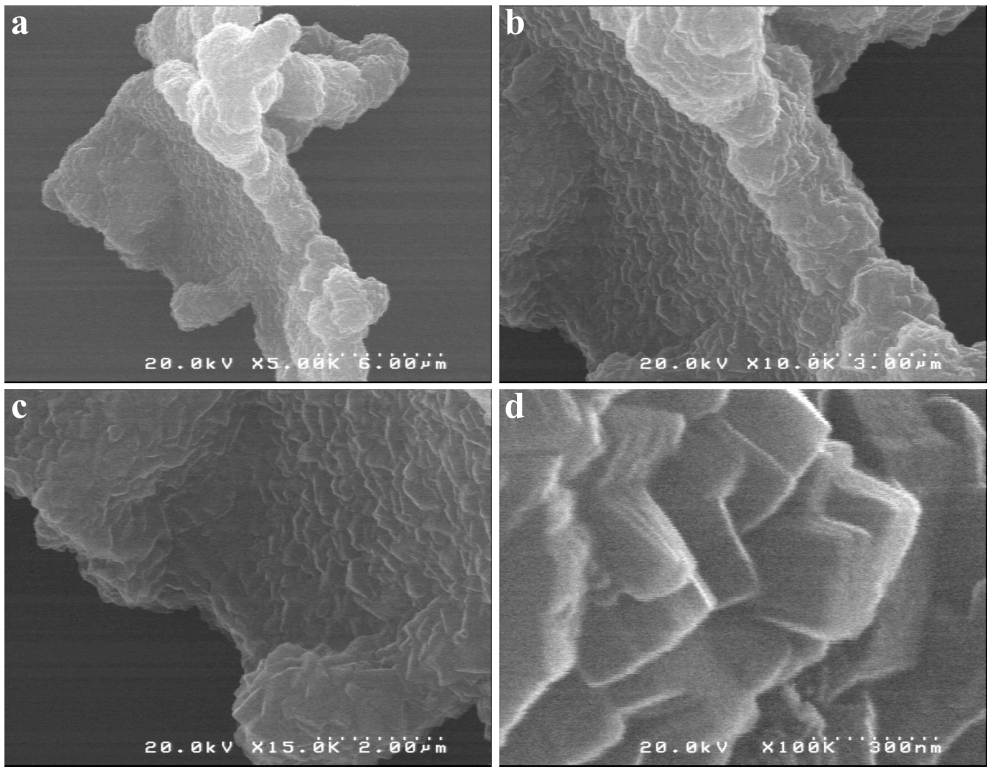

Figure 5. SEM images of TPB-TMDPDA-COF.

According to the pore volume, TPB-TMDPDA-COF could load trz in the pores with the highest content of 182.6 wt%. trz@TPB-TMDPDA-COF displayed almost zero surface area, and exhibited a sharp decrease of the (100) facet in PXRD (Fig. 6, purple curve). These results indicate that the mesochannels are nearly full filled with trz proton conveyers. These results indicate that the trz@TPB-DMTP-COF has sufficient thermal stability for proton conduction.

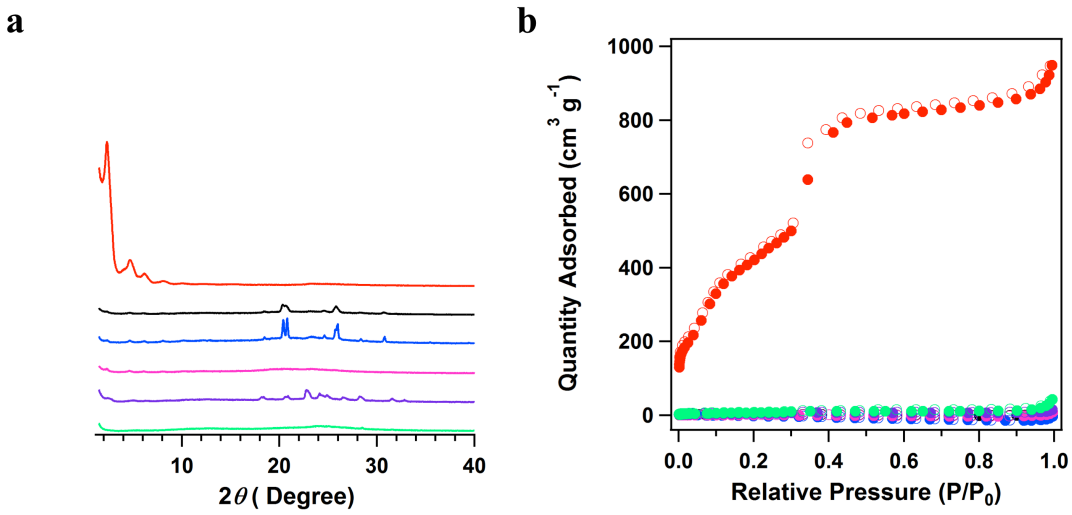

Figure 6. (**a**) PXRD patterns and (**b**) N_2 sorption curves of TPB-TMDPDA-COF (red curve), im@TPB-TMDPDA-COF (blue curve), d_4-im@TPB-TMDPDA-COF (black curve), trz@TPB-TMDPDA-COF (purple curve), im@TPB-TMDPDA-COF with the im content of 81 wt% (magenta curve), trz@TPB-TMDPDA-COF with the trz content of 91 wt% (green curve).

5.2.2 Impedance Spectroscopy

The proton conductivities of trz@TPB-TMDPDA-COF were measured by using alternating-current impedance spectroscopy. The impedance profiles showed a tail at low frequencies that can be ascribed to the blocking of proton at the Ag electrodes, and a semicircle that can be assigned to the charge transfer. The proton conductivity was calculated from equation: $\sigma = L/(Z \times A)$, in the equation A displays the electrode area (cm^2), Z demonstrates the impedance (Ω), L shows the measured sample thickness (cm) and σ represents the conductivity (S cm^{-1}). The proton conductivity of trz@TPB-TMDPDA-COF was measured under different conditions and the low activation energy implies the mechanism of Grotthuss-type hopping for proton conduction in the COFs..

To confirm the generality of this route, imidazole (im) was used as proton carriers. TGA showed that the content of im was up to 148 wt% (Fig. 4, blue curve), which was quite close to the theoretical content (161 wt%). The crystallinity of the im@TPB-TMDPDA-COF samples decreased (Fig. 6, blue curve) and the porosity of im@TPB-TMDPDA-COF was only 0.3 $m^2 g^{-1}$ for the BET surface area. These results manifests that the COF channels are almost fully occupied with the im molecules.

The impedance plots of im@TPB-TMDPDA-COF had a similar shape to the previous one.

Deuterium-substituted imidazole (d_4-im) was employed to act as the proton carriers to prepare d_4-im@TPB-TMDPDA-COF with a d_4-im content of 164 wt% to confirm the hopping mechanism (Fig. 4, black curve). The proton conductivities and the activation energy of ion conduction was calculated from the experimental data.

The decrement of proton conductivity of d_4-im@TPB-TMDPDA-COF could be attributed to the isotope effect, because the mass of deuterium is twice that of a proton. Combine the low activation energy, the isotopic effect confirms the assumption that proton conduction across the channels is based on the movement of protons other than the motion of imidazole molecules.

Then I decreased the content of imidazole from 161 wt% to 80.5 wt% in the channels of TPB-TMDPDA-COF and measured its conductivity. The conductivity of im@TPB-TMDPDA-COF with an im content of 80.5 wt% at 130 °C was much lower. The data was much lower compared with im@TPB-TMDPDA-COF with an im content of 161 wt%. These comparative studies show the significance of im in the channels for proton conduction. A similar decrease tendency was observed for tz@TPB-TMDPDA-COF when the content of tz was decreased from 182.6 wt% to 91.3 wt%. The proton conductivity of trz@TPB-TMDPDA-COF with a tz content of 91.3 wt% at 130 °C was only 1.93×10^{-5} S cm^{-1}. The data was much smaller than that of trz@TPB-TMDPDA-COF.

5.3. Design and Synthesis of TMQPDA-PyTTA-COF

A novel TMQPDA-PyTTA-COF was synthesized by polycondensation of monomers of TMQPDA and TPB under solvothermal conditions. The PXRD pattern displayed peaks at 1.4°, 2.82°, 10.91°, 12.55°, and 23.26°, respectively (Fig. 7a). The nitrogen sorption isotherm curves of TMQPDA-PyTTA-COF are type-IV nitrogen sorption isotherms, which are characteristics of mesoporous materials (Fig. 7b). TMQPDA-PyTTA-COF consists of two pores with pore sizes of 5.6 and 2.5 nm (Fig. 7c and d, red curves), and exhibits a pore volume of 1.22 $cm^3\ g^{-1}$ (Fig. 7c and d, black curves). The BET surface area was 1500 $m^2\ g^{-1}$.

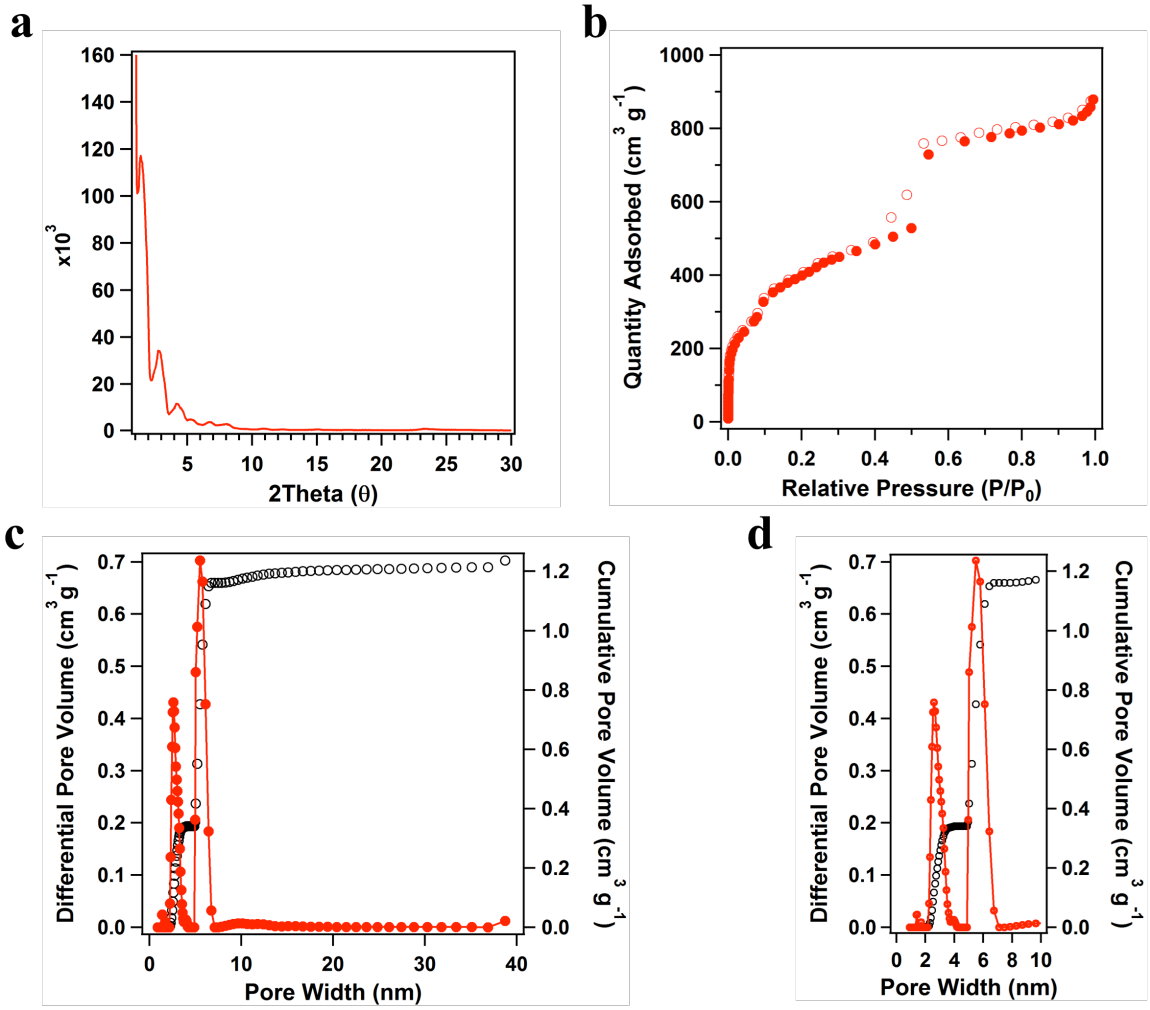

Figure 7. (**a**) PXRD patterns, (**b**) N_2 sorption curves, (**c**) pore size (red) and pore size distribution (black) profiles, and **(d)** enlarged pore size (red) and pore size distribution (black) of TMQPDA-PyTTA-COF.

5.4 Conclusion

In summary, I have explored different building blocks for the construction of imine-linked large-pore COFs with different kinds of pore shape and pore size. And found the relationship between the proton conductivity and the pore environment.

5.5 Experimental Sections

5.6 References

[1] Huang, N.; Wang, P.; Jiang, D. *Nat. Rev. Mater.* **2016**, 1, 106086.

[2] Feng, X.; Ding, X.; Jiang, D. *Chem. Soc. Rev.* **2012**, 41, 6010.

[3] Higashihara, T.; Matsumoto, K.; Ueda, M. *Polymer* **2009**, 50, 5341.

[4] Fang, J.; Guo, X.; Harada, S.; Watari, T.; Tanaka, K.; Kita, H.; Okamoto, K.; *Macromolecules* **2002**, 35, 9022.

[5] Xing, P.; Robertson, G. P.; Guiver, M. D.; Mikhailenko, S. D.; Kaliaguine, S. S *Macromolecules* **2004**, 37, 7960.

[6] Mader, J. A.; Benicewicz, B. C. *Macromolecules* **2010**, 43, 6706.

[7] Matsumoto, K.; Higashihara, T.; Ueda, M. *Macromolecules* **2009**, 42, 1161.

[8] Maffeo, C.; Bhattacharya, S.; Yoo, J., Wells, D.; Aksimentiev, A. *Chem. Rev.* **2012**, 112, 625.

[9] Horike, S.; Umeyama, D.; Kitagawa, S. *Acc. Chem. Res.* **2013**, 46, 2376.

[10] Yoon, M.; Suh, K.; Natarajan, S.; Kim, K. *Angew. Chem. Int. Ed.* **2013**, 52, 2688.

[11] Xu, G.; Otsubo, K.; Yamada, T.; Sakaida, S.; Kitagawa, H. S *J. Am. Chem. Soc.* **2013**, 135, 7438.

[12] Shimizu, G. K.; Taylor, J. M.; Kim, S. *Science* **2013**, 341, 354.

[13] Mauritz, K. A.; Moore, R. B. *Chem. Rev.* **2004**, 104, 4535.

[14] Schmidt-Rohr, K.; Chen, Q. *Nat. Mater.* **2008**, 7, 75.

[15] Xu, H.; Jiang, D. *Nat. Chem.* **2014**, 6, 564.

[16] Jeong, N. C.; Samanta, B.; Lee, C. Y.; Farha, O. K.; Hupp, J. T. *J. Am. Chem. Soc.* **2012**, 134, 51.

[17] Bureekaew, S.; Horike, S.; Higuchi, M.; Mizuno, M.; Kawamura, T.; Tanaka, D.; Yanai, N.; Kitagawa, S. *Nat. Mater.* **2009**, 8, 831.

[18] Xu, H.; Gao, J.; Jiang, D. *Nat. Chem.* **2015**, 7, 905.

[19] Higashino, T.; Yamada, T.; Yamamoto, M.; Furube, A.; Tkachenko, N. V.; Miura, T.; Kobori, Y.; Jono, R.; Yamashita, K.; Imahori, H. *Angew. Chem. Int.*

Ed. **2016**, 11, 629.

Chapter 6

Design and Synthesis of Polyelectrolyte Covalent Organic Frameworks for Anion Transport

Hong Xu, Shanshan Tao, Naohiro Obata, Yuh Hijikata, Stephan Irle, Qiuhong Chen and Donglin Jiang

(Hong Xu and Shanshan Tao contributed equally)

Submitted

Abstract

In this chapter, the author describes the design and synthesis of polyelectrolyte COFs for anion transport. Hydroxide anion, the negative counterpart of proton in water, could serve as an active ion carrier in advanced fuel cells but it suffers from limited mobility because of low diffusion coefficient and 17-fold-high weight compared to protons. I demonstrated that a crystalline porous COF with ordered one-dimensional channels enables high-rate hydroxide anion transport. The frameworks were integrated with imidazolium-hydroxide anion salts on the channel walls in which the conductivity of hydroxide ions along the ordered chains reached 7.7×10^{-4} S cm^{-1}. Hydroxide ion conduction requires low activation energy of 0.16 eV and occurs *via* a mechanism of proton hopping in the hydrogen network. These results suggest a new way based on COFs to anion-conducting materials.

6.1 Introduction

Fuel cells have the higher energy-conversion efficiencies compared with those of internal combustion engine systems limited by the Carnot cycle and are regarded as promising and environmentally-friendly power sources for transportation and stationary applications.[1] Compared to the well-developed proton-conducting materials, the hydroxide anion-conducting materials are less developed.[2,3] The anion-conduction-based fuel cells possess a number of advantages over proton-conduction-based cells, including rapid reaction kinetic, low-cost metal catalysts and broad scope of fuels. The rapid kinetics can even remove the need of expensive platinum catalysts from the fuel cells and enable the use of normal metal catalysts for cathodic oxygen reduction reaction. Moreover, the alkaline polyelectrolyte membrane fuel cells enable the use of methanol, ethanol and propanol as fuels that are easy for storage and transportation and have high volumetric energy density compared to hydrogen.[2,3]

Despite of these splendid advantages, polyelectrolyte materials that enable high-rate hydroxide anion conduction remain a challenge. Hydroxide anions suffer from limited mobility because of low diffusion coefficient and 17-fold-high weight compared to protons. Materials possess crystallinity and porosity such as MOFs and COFs have shown considerable potentials in designing proton-conducting materials by exploring their ordered porous structures.[4-12] However, these porous materials have not been well developed for hydroxide anion conduction.

COFs are a class of the porous polymers that allow the building of 1D channels and demonstrate various promising applications.[11-21] Direct synthesis of anion-functionalized COF materials faces a difficulty because charged skeletons impede π-π stacking that is required the formation of layered channel structures. In this context, pore surface engineering is a powerful tool that allows for predesignable functionalization of pore walls of COFs while retaining their ordered skeletons.[21-23] TPB-DMTP-COF has been used for this purpose because it is stable in boiling water

and even under strong alkaline conditions.[22] This chapter describes the hydroxide anion-conducting COFs via pore-wall engineering of TPB-BPTA-COF with electrolyte units and highlights the achievement of low-energy-barrier, high-rate hydroxide anion conduction through synthetic control over the density of anion-conducting groups anchored to the pore walls.

6.2 Results and Discussions

6.2.1 Synthesis and Characterizations

The author utilized a C_3-symmetric TAPB and C_2-symmetric monomers to prepare $[HC{\equiv}C]_X$-TPB-BPTA-COFs with ethynyl-appended pore walls and synthesized the ionic COFs. The polycondensation reactions were performed under solvothermal conditions for a designated time. IR spectra of $[PF_6^-]_X$-TPB-BPTA-COFs displayed the extinction of the vibration peaks at 2120 and 3290 cm^{-1} that were assigned to the H–C≡C groups (Figure 1). This result indicates that all the ethynyl groups on the pore walls were reacted. The appearance of an intense absorption peak at 558 cm^{-1} that was assigned to PF_6^- indicates the successful integrating of electrolytes to the 1D channels of the COFs. Anion exchange of $[PF_6^-]_X$-TPB-BPTA-COFs with 0.5 M aqueous NaOH solution as eluent replaced PF_6^- with OH^- anions and transformed $[PF_6^-]_X$-TPB-BPTA-COFs into their corresponding $[OH^-]_X$-TPB-BPTA-COFs. IR spectra of $[OH^-]_X$-TPB-BPTA-COFs revealed the extinction of the vibration peaks at 558 cm^{-1}, which suggest that all the PF_6^- ions are quantitatively exchanged with OH^- anions. Therefore, the pore surface engineering approach enables the synthesis of anion-functionalized COFs.

Notably, the density of the OH^- anions in the channels of COFs is different between $[OH^-]_X$-TPB-BPTA-COFs. In $[OH^-]_{50}$-TPB-BPTA-COF, the OH^- anions were anchored to the half of edges of the polygons, whereas the OH^- anions were anchored to all of the edges of $[OH^-]_{100}$-TPB-BPTA-COF. The electrolyte chains are anchored on walls and compose electrolyte monolayer on the pore walls in which the OH^- anions are located at the termini of the electrolyte chains and electrostatically assembled on the surface of the monolayer. From a viewpoint of stacking layer

structure, the OH^- anions between neighboring layers are separated by 8.8 Å on average in $[OH^-]_{50}$-TPB-BPTA-COF and are separated by 4.4 Å in $[OH^-]_{100}$-TPB-BPTA-COF. Therefore, the pore surface engineering method not only enables the alignment of electrolyte chains into monolayers but also allows for the synthetic control over the spatial distance of these electrolyte chains on the pore walls.

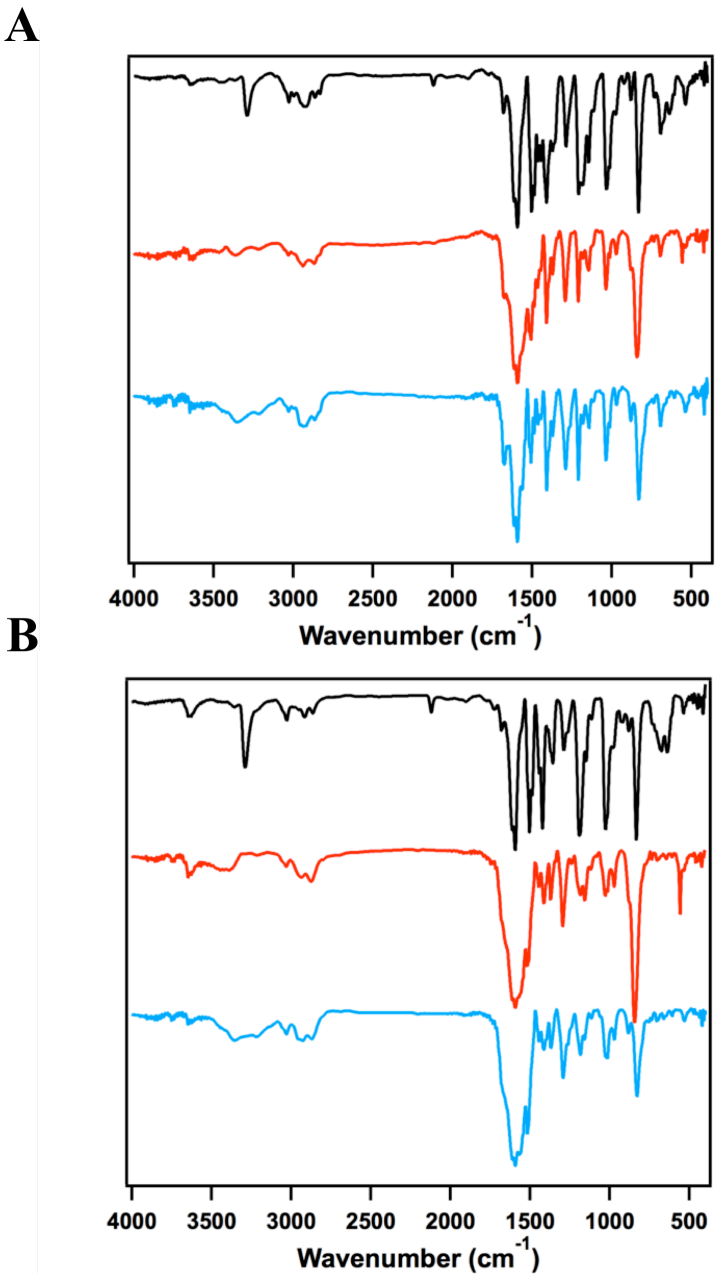

Figure 1. (A) FT-IR spectra of $[HC{\equiv}C]_{50}$-TPB-BPTA-COFs (black), $[PF_6^-]_{50}$-TPB-BPTA-COFs (red) and $[OH^-]_{50}$-TPB-BPTA-COFs (blue). **(B)** FT-IR spectra of $[HC{\equiv}C]_{100}$-TPB-BPTA-COFs (black), $[PF_6^-]_{100}$-TPB-BPTA-COFs (red)

and $[OH^-]_{100}$-TPB-BPTA-COFs (blue).

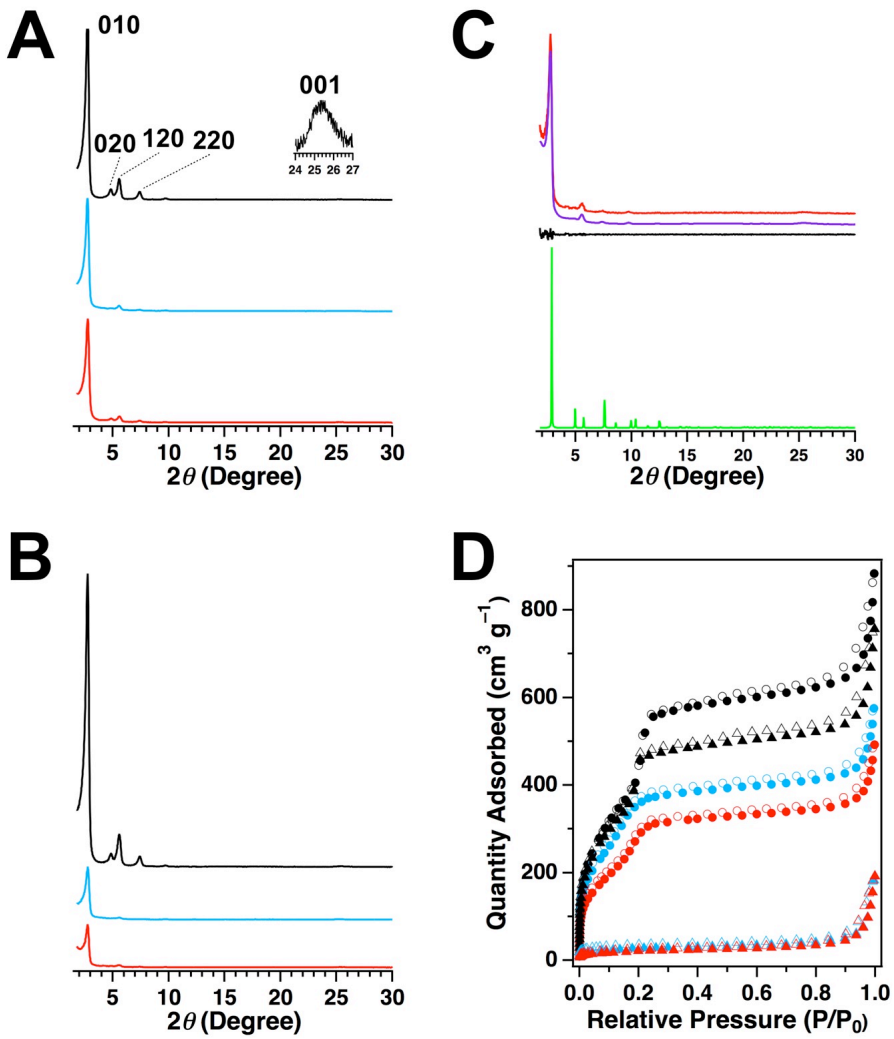

Figure 2. (**A**) PXRD patterns of $[HC{\equiv}C]_{50}$-TPB-BPTA-COF (black curve), $[PF_6^-]_{50}$-TPB-BPTA-COF (blue curve) and $[OH^-]_{50}$-TPB-BPTA-COF (red curve). (**B**) PXRD patterns of $[HC{\equiv}C]_{100}$-TPB-BPTA-COF (black curve), $[PF_6^-]_{100}$-TPB-BPTA-COF (blue curve) and $[OH^-]_{100}$-TPB-BPTA-COF (red curve). (**C**) PXRD profiles of $[OH^-]_{100}$-TPB-BPTA-COF. Experimentally observed (red), Pawley refined (purple), and their difference (black), simulated using AA stacking mode (green). (**D**) Nitrogen sorption isotherm profiles of $[HC{\equiv}C]_{50}$-TPB-BPTA-COF (black circle curve), $[PF_6^-]_{50}$-TPB-BPTA-COF (blue circle curve), $[OH^-]_{50}$-TPB-BPTA-COF (red circle curve), $[HC{\equiv}C]_{100}$-TPB-BPTA-COF (black triangle curve), $[PF_6^-]_{100}$-TPB-BPTA-COF (blue triangle curve), and

$[OH^-]_{100}$-TPB-BPTA-COF (red triangle curve). Filled and open circles represent adsorption and desorption.

Figure 2 summarizes the crystallinity and porosity results. The $[HC{\equiv}C]_X$-TPB-BPTA-COFs samples exhibited PXRD patterns with peaks at 2.75°, 5.59°, 7.43°, 9.77°, and 25.4°, which were assigned to the (010), (020), (120), (220), and (001) facets, respectively (Fig. 2A and B, black curves). The $[PF_6^-]_X$-TPB-BPTA-COFs (blue curves) and $[OH^-]_X$-TPB-BPTA-COFs (red curves) exhibited similar PXRD peaks to their precursors.[22] These PXRD results indicate that surface engineering of the pore walls of TPB-BPTA-COF does not change the crystalline structure of the COFs. The simulated data were shown in Appendix Tables 12-13.

Table 1. Surface area, pore size, and pore volume of COFs

COFs	BET Surface Area ($m^2\ g^{-1}$)	Langmuir Surface Area ($m^2\ g^{-1}$)	Pore Size (nm)	Pore Volume ($cm^3\ g^{-1}$)
$[HC{\equiv}C]_{50}$-TPB-BPTA-COFs	1605	2104	3.09	0.90
$[HC{\equiv}C]_{100}$-TPB-BPTA-COFs	1443	1898	2.89	0.74
$[PF_6^-]_{50}$-TPB-BPTA-COFs	1232	1708	2.60	0.59
$[PF_6^-]_{100}$-TPB-BPTA-COFs	97	139	1.4	0.004
$[OH^-]_{50}$-TPB-BPTA-COFs	1046	1359	2.85	0.48
$[OH^-]_{100}$-TPB-BPTA-COFs	76	119	1.46	0.028

Nitrogen sorption isotherm measurements of $[HC{\equiv}C]_X$-TPB-BPTA-COF-COF at 77 K revealed a rapid uptake followed by a sharp increase at low pressure between P/P_0 = 0.2–0.25 (Fig. 2D, black curves, X = 50; circles, X = 100; triangles). As the

ethynyl content was increased, the porosity of $[HC{\equiv}C]_X$-TPB-BPTA-COFs decreased. $[HC{\equiv}C]_{50}$-TPB-BPTA-COF exhibited a surface area of 1605 $m^2\ g^{-1}$.

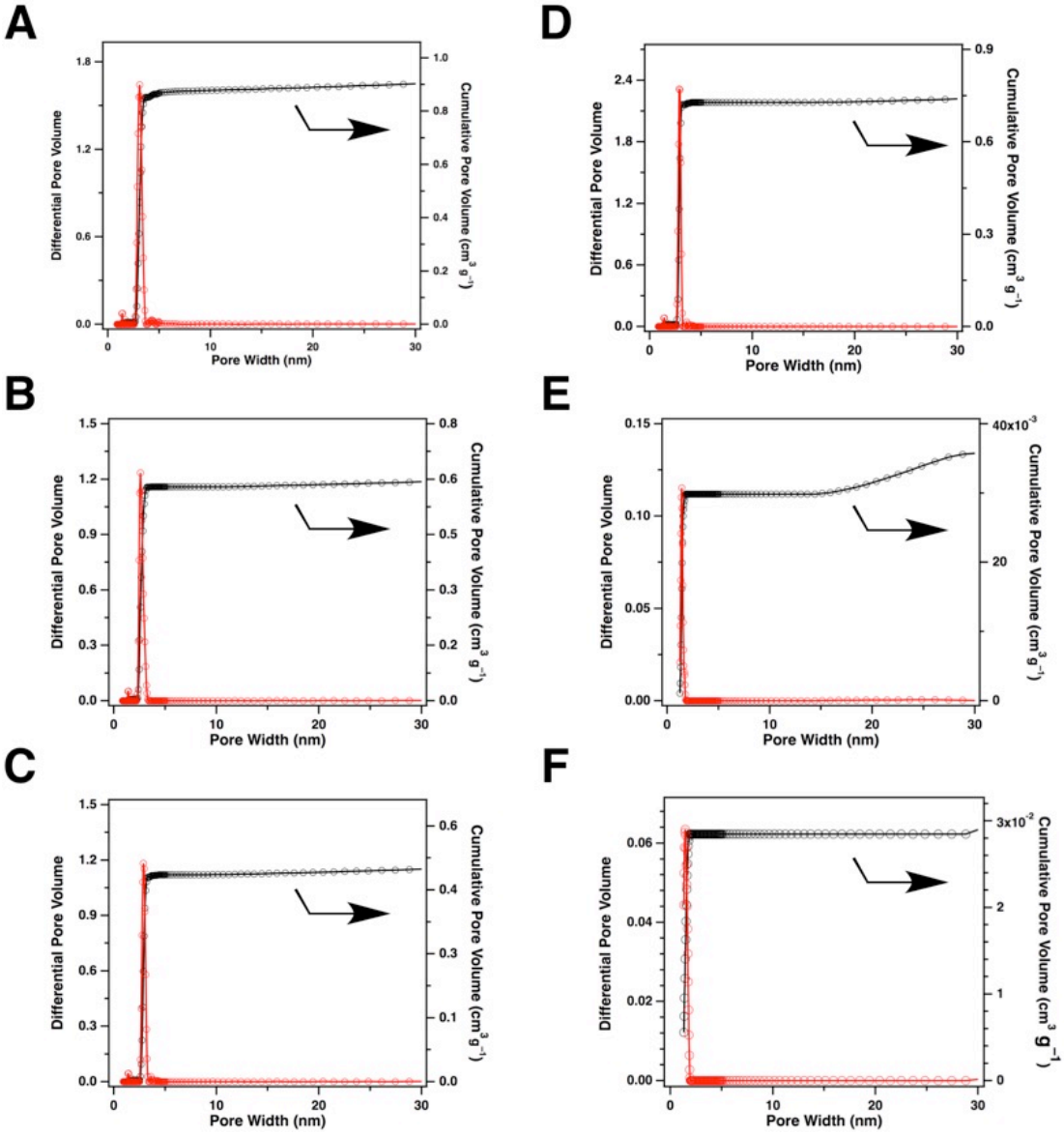

Figure 3. Cumulative pore volume (black circles), pore size distribution (red circles) and profiles of the COFs. (**A**: $[HC{\equiv}C]_{50}$-TPB-BPTA-COF; **B**: $[PF_6^-]_{50}$-TPB-BPTA-COF; **C**: $[OH^-]_{50}$-TPB-BPTA-COF; **D**: $[HC{\equiv}C]_{100}$-TPB-BPTA-COF; **E**: $[PF_6^-]_{100}$-TPB-BPTA-COF; **F**: $[OH^-]_{100}$-TPB-BPTA-COF.)

By using NLDFT method, pore size distribution profile was obtained from the

nitrogen isotherm curves. The pore size was 3.09 and 2.89 nm for $[HC{\equiv}C]_{50}$-TPB-BPTA-COF and $[HC{\equiv}C]_{100}$-TPB-BPTA-COF, respectively (Fig. 3, Table 1). Upon click reactions, more bulky groups were anchored on the pore walls of the 1D channels of COFs. As a result, $[PF_6^-]_{50}$-TPB-BPTA-COF (Fig. 2D, blue circle curve) and $[OH^-]_{50}$-TPB-BPTA-COF (Fig. 2D, red circle curve) exhibited a decrease in the porosity, their pore sizes were 2.60 and 2.85 nm, respectively (Fig. 3, Table 1). This decrease tendency is much profound for the COFs with high load content of electrolyte chains on the pore walls. Indeed, $[PF_6^-]_{100}$-TPB-BPTA-COF (Fig. 2D, blue triangle curve) and $[OH^-]_{100}$-TPB-BPTA-COF (Fig. 2D, red triangle curve) exhibited sharply decreased adsorption of nitrogen. At the same time, their pore size and pore volume decreased to a level of only 1.4 nm and 0.03 $cm^3\ g^{-1}$ (Table 1). The pore size distribution profiles showed the existence of just one type pore, suggesting that the electrolyte groups are uniformly engineered to the pore walls (Fig. 3).

The $[OH^-]_X$-TPB-BPTA-COFs samples were pressed under hydraulic pressure of 100 kN into pellets with the diameter of 1 cm and thickness of 2.3-2.8 mm, which were sandwiched between two Ag electrodes for impedance measurements. And measure the ionic conductivity under different conditions and also calculated the activation energy.

Different methods to exchange PF^{6-} to hydroxide anion resulted in quite different anion conductivity[24]. $[PF^{6-}]_{100}$-TPB-BPTA-COF treated with KOH in ultra pure deionized water exhibited different anion conductivity. $[PF^{6-}]_{100}$-TPB-BPTA-COF treated with KOH in absolute ethanol solution exhibited the highest anion conductivity. At 40 °C, the ionic conductivity is slight lower than that of 2@KOH that is the highest reported under 100% RH.[24] Crystalline microporous MOFs (ZIF-8) has been developed for hydroxide anion conduction with the state-of-the-art conductivity of 2.3×10^{-8} S cm^{-1} at 25 °C.[25]

As shown above, the difference between $[OH^-]_{50}$-TPB-BPTA-COF and $[OH^-]_{100}$-TPB-BPTA-COF in anion conduction is distinct and profound. The high density of electrolyte units of hydroxide anions in $[OH^-]_{100}$-TPB-BPTA-COF not only provides a high concentration of OH^- in the channels but also offers a proximate distance of only 4.4 Å between two OH^- groups of neighboring layers. These two structural features facilitate the OH^- conduction in $[OH^-]_{100}$-TPB-BPTA-COF. The elaborate designability of electrolyte density and functions in the aligned channels enables the disclosure of the two major structural factors that control the anion conduction in COFs.

The EDS analysis and mapping revealed that $[OH^-]_{100}$-TPB-BPTA-COF just contain carbon, nitrogen and oxygen (Figs. 4 and 5). The metal ions have been fully washed out and the ionic conductivity merely originates from OH^-.

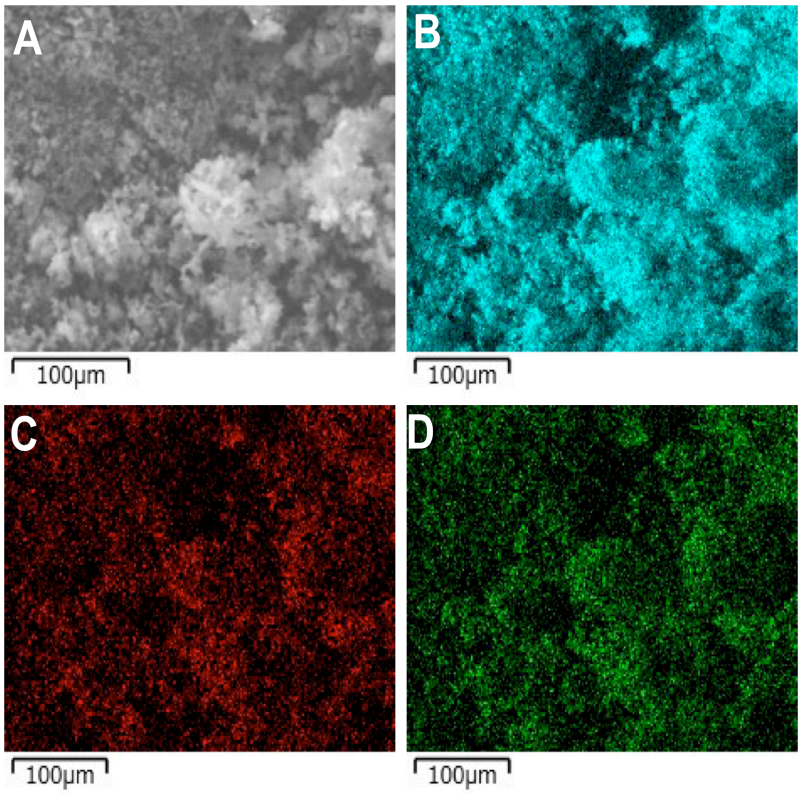

Figure 4. Elemental distribution of $[OH^-]_{100}$-TPB-BPTA-COF: (**A**) SEM image of $[OH^-]_{100}$-TPB-BPTA-COF; (**B**) distribution of C; (**C**) distribution of N and (**D**) distribution of O.

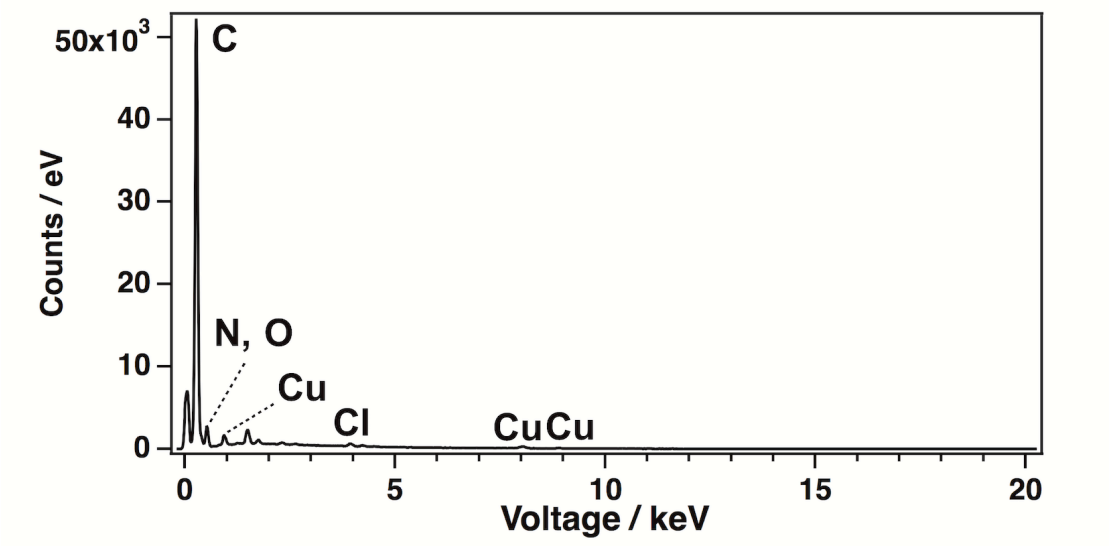

Figure 5. EDS of $[OH^-]_{100}$-TPB-BPTA-COF.

DFTB molecular dynamics (DFTB-MD) simulations revealed the OH^-conduction mechanism. After the layered structure of $[OH^-]_{100}$-TPB-BPTA-COF with water molecules was optimized under the periodic boundary condition, and MD simulations were conducted using the cut-out three layered 1D channel model. Figure 6 shows the snapshots of the OH^- transport from OH^- to the neighboring three H_2O molecules. This conduction process completes within 356 fs, in which each step requires a timescale of only 120 fs on average. During the transport, continuous OH^- transportation takes place *via* proton hopping. Therefore, the OH^- conduction is induced by neither OH^- hopping nor OH^- migration but proton hopping.

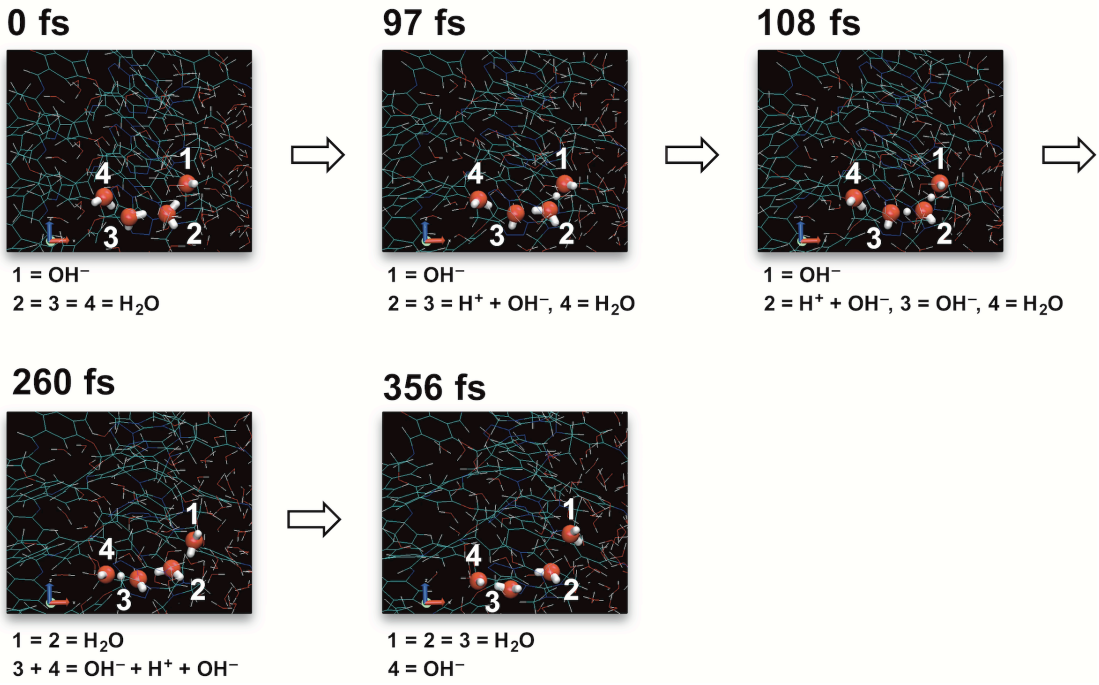

Figure 6. Snapshots of the DFTB-MD simulations of OH^- conduction from OH^- (1) to three neighboring H_2O molecules (2, 3 and 4) in the hydrogen-bonding network at different time. Red and white spheres indicate focused oxygen and hydrogen. The framework and other water molecules and hydroxide ions are represented using wired model.

6.3 Conclusion

In summary, the author has designed and synthesized covalent organic frameworks for hydroxide anion conduction. The low activation energy barriers and molecular dynamics indicate that the conduction of hydroxide anions in the COFs is governed by proton hopping. This insight provides a new mechanistic base for developing high-rate anion-conducting crystalline porous COF materials. With the structural diversity and design ability of both skeletons and electrolyte walls, COFs offer a new molecular platform for exploring anion conduction and chemical-electric energy conversions.

6.4 Experimental Sections

6.4.1 Methods

The equipment needed to analysis the COFs were clearly recorded in Chapter 2.

DFTB+ simulation. The third order density functional tight-binding (DFTB3) method[25-27] implemented in the DFTB+ program package version 1.2.2 was used for optimizations and MD simulations. In all calculations, 3-ob parameters and Hubbard parameters, –0.1492 for C, –0.1535 for N, –0.1575 for O, and –0.1857 for H were used. Lennard-Jones type dispersion was included to depict van der Waals interaction.[28-30]

Preparation for the 1D channel model. The $[OH^-]_{100}$-TPB-BPTA-COF with 50 water molecules per the one hexagonal pore was optimized using the DFTB3 method under the periodic boundary condition. The parameters of $\alpha = \beta = 90.0$ º $\gamma = 60.0$ º, $a = b = 37.5$ Å, $c = 9.0$ Å were changed to $a = 35.7$ Å, $b = 36.2$ Å, $c = 4.5$ Å, $\alpha = 99.5$ º, $\alpha = \beta = 95.9$ º, and $\gamma = 59.7$ º after the optimization. Totally 29 water molecules was added to the pore for the consistency with the impedance measurements condition in the experiments, in which the water density in the pore should be 1 $cm^3\ g^{-1}$. To disperse the water molecules, NVT ensemble MD simulation was performed using Nose-Hoover thermostat for 3 ps with 0.4 time step at 300 K with the fixed cell parameters obtained.

DFTB-MD simulation: MD simulation was performed for 0.6 ps with 0.4 time step at 353 K using the cut-out three layered 1D channel with the fixing the 6 vertex benzene rings in each layer. An external perpendicular electric field of 5.0×10^{11} Hz and $2.57 \times 10^9\ Vm^{-1}$ was applied to the layers.

6.4.2 Materials and Synthetic Procedures

6.5 References

[1] Hoffert, M. I.; Caldeira, K.; Benford, G.; Criswell, D. R.; Green, C.; Herzog, H.; Jain, A. K.; Kheshgi, H. S.; Lackner, K. S.; Lewis, J. S.; Lightfoot, H. D.; Manheimer, W.; Mankins, J. C.; Mauel, M. E.; Perkins, L. J.; Schlesinger, M. E.; Volk, T.; Wigley, T. M. L. *Science* **2002**, 298, 981.

[2] Zhang, H.; Shen, P. K. *Chem. Rev.* **2012**,112, 2780.

[3] Wang, Y. J.; Qiao, J.; Baker, R.; Zhang, J. *Chem. Soc. Rev.* **2013**, 42, 5768.

[4] Shimizu, G. K.; Taylor, J. M.; Kim, S. *Science* **2013**, 341, 354.

[5] Horike, S.; Umeyama, D.; Kitagawa, S. *Acc. Chem. Res.* **2013**, 46, 2376.

[6] Yoon, M.; Suh, K.; Natarajan, S.; Kim, K. *Angew. Chem. Int. Ed.* **2013**, 52, 2688.

[7] Bureekaew, S.; Horike, S.; Higuchi, M.; Mizuno, M.; Kawamura, T.; Tanaka, D.; Yanai, N.; Kitagawa, S. *Nat. Mater.* **2009**, 8, 831.

[8] Hurd, J. A.; Vaidhyanathan, R.; Thangadurai, V.; Ratcliffe, C. I.; Moudrakovski, I. L.; Shimizu, G. K. H. *Nat. Chem.* **2009,** 1, 705.

[9] Xu, G.; Otsubo, K.; Yamada, T.; Sakaida, S.; Kitagawa, H. *J. Am. Chem. Soc.* **2013**, 135, 7438.

[10] Jeong, N. C.; Samanta, B.; Lee, C. Y.; Farha, O. K.; Hupp, J. T. *J. Am. Chem. Soc.* **2012**, 134, 51.

[11] Xu, H.; Jiang, D. *Nat. Chem.* **2014**, 6, 564.

[12] Xu, H.; Tao, S.; Jiang, D. *Nat. Mater.* **2016**, 15, 722.

[13] Feng, X.; Ding, X.; Jiang, D. *Chem. Soc. Rev.* **2012**, 41, 6010.

[14] Côté, A. P.; Benin, A. I.; Ockwig, N. W.; O'Keeffe, M.; Matzger, A. J.; Yaghi, O. M. *Science* **2005**, 310, 1166.

[15] Colson, J. W.; Woll, A. R.; Mukherjee, A.; Levendorf, M. P.; Spitler, E. L.; Shields, V. B.; Spencer, M. G.; Park, J.; Dichtel, W. R. *Science* **2011**, 332, 228.

[16] Chandra, S.; Kundu, T.; Kandambeth, S.; BabaRao, R.; Marathe, Y.; Kunjir, S. M.; Banerjee, R. *J. Am. Chem. Soc.* **2014**, 136, 6570.

[17] Kuhn, P.; Antonietti, M.; Thomas, A. *Angew. Chem. Int. Ed.* **2008**, 47, 3450.

[18] Zhu, X.; Tian, C.; Mahurin, S. M.; Chai, S.; Wang, C.; Brown, S.; Veith, G. M.; Luo, H.; Liu, H.; Dai, S. *J. Am. Chem. Soc.* **2012**, 134, 10478.

[19] Huang, N.; Wang, P.; Jiang, D. *Nat. Rev. Mater.* **2016**, 1, 106086.

[20] Nagai, A.; Guo, Z.; Feng, X.; Jin, S.; Chen, X.; Ding, X.; Jiang, D. *Nat. Commun.* **2011**, 2, 536.

[21] Xu, H.; Chen, X.; Gao, J.; Lin, J.; Addicoat, M.; Irle, S.; Jiang, D. *Chem. Commun.* **2014**, 50, 1292.

[22] Xu, H.; Gao, J.; Jiang, D. *Nat. Chem.* **2015**, 7, 905.

[23] Huang, N.; Krishna, R.; Jiang, D. *J. Am. Chem. Soc.* **2015**, 137, 7079.

[24] Montoro, C.; Ocon, P.; Zamora, F.; Navarro, J. A. R. *Chem. Eur. J.* **2016**, 22, 1646.

[25] Aradi, B.; Hourahine, B.; Frauenheim, T. *J. Phys. Chem. A* **2007**, 111, 5678.

[26] Lukose, B.; Kuc, A.; Heine, T. *J. Mol. Model*. **2013**, 19, 2143.

[27] Gaus, M.; Cui, Q.; Elstner, M. *J. Chem. Theory Comput*. **2011**, 7, 931.

[28] Elstner, M.; Porezag, D.; Jungnickel, G.; Elsner, J.; Haugk, M.; Frauenheim, Th.; Suhai, S.; Seifert, G. *Phys. Rev. B* **1998**, 58, 7260.

[29] Gaus, M.; Goez, A.; Elstner, M. *J. Chem. Theory Comput.* **2013**, 9, 338.

[30] Rappe, A. K.; Casewit, C. J.; Colwell, K. S.; GoddardIII, W. A.; Skiff, W. M. *J. Am. Chem. Soc*. **1992**, 114, 10024.

[31] Kuhnert, N.; Rossignolo, G. M.; Lopez-Periago, A. *Org. Biomol. Chem*. **2003**, 1, 1157.

[32] Lopez-Maya, E.; Montoro, C.; Colombo, V.; Barea, E.; Navarro, J. A. R. *Adv. Funct. Mater.* **2014**, 24, 6130.

Chapter 7

Summary and Perspectives

In chapter 1, I summarized the chemical science of COFs developed in recent years. I illustrated the design principle based on topology diagram, the diversity of building blocks, the variety of linkages and reaction conditions. I further summarized the progress in functional exploration for proton conduction.

In chapter 2, I designed and synthesized the stable, crystalline, and mesoporous COFs. The reaction conditions and their chemical and thermal stabilities were investigated. Their crystal structures and porosities were disclosed by using various analytical methods.

In chapter 3, I developed the COFs for proton conduction using organic heterocycles as proton carriers. Especially, trizaole and imidazole were employed as high-temperature proton carrier and integrated into the mesoporous channels of COFs. I studied the proton conductivity using impedance spectroscopy. As a result, at 130 °C, the proton conductivity for triazole-loaded COF up to 10^{-3} S cm^{-1}.

In chapter 4, I designed mesoporous TPB-DMTP-COF and TAPB-DMPTA-COF for proton conduction based on phosphoric acid. The high pore volume of the two COFs enables the loading of proton carrier PA at high content. The proton conductivity of PA@TPB-DMPT-COF at 100 and 120 °C are the highest among porous materials. Notably, at 160 °C PA@TAPB-DMPTA-COF achieves a high proton conductivity. These results suggest a great potential for COFs for applications in fuel cells.

In chapter 5, I designed and synthesized large-pore TPB-TMDPDA-COF for proton conduction. TPB-TMDPDA-COF has a pore volume of is 1.31 cm^3 g^{-1} and exhibits a proton conductivity of 10^{-3} S cm^{-1} with imidazole and triazole proton carriers.

In chapter 6, I designed and synthesized COFs with polyelectrolyte units on the pore walls by using pore surface engineering method and stable COFs as a precursor. The OH^--appended COFs exhibited high OH^- conduction. The OH^- conduction is facilitated by proton hopping through the hydrogen-bonding networks.

In chapter 7, I summarized the results of this work and show the perspectives of COFs for ion transport.

The tunable skeletons and pore size engineering of COFs control the diversity of functions, such as gas adsorption and separation, catalysis, and photovoltaic applications. However, the proton conduction based on COFs has not been investigated.

High temperature polymer exchange membranes are desired. Because high temperature can create fast kinetics, increases the tolerance of the Pd catalyst to carbon monoxide. There is no need of humidification system, which can greatly reduce the costs of the fuel cells. COFs have shown high thermal stability up to 400 °C without decomposition under N_2 atmosphere.

As an alternative to the traditional Nafion as proton-conducting membrane, porous materials have attracted great attention because of their capability of making small micropores that can interact with protons and have the potential to promote the proton conduction across the pores.

Through the three-year research work, I have demonstrated that 2D mesoporous COFs are promising for proton conduction. Since COFs are insoluble in organic solvents that hider the formation of flexible films. Developing COFs to prepare flexible films is a future direction of research in the proton conduction.

List of Publications

Original Papers

1. Hong Xu, Shanshan Tao, Donglin Jiang, Proton Conduction in Crystalline and Porous Covalent Organic Frameworks. *Nat. Mater.* **2016**, 15, 722–726

2. Hong Xu,[1] Shanshan Tao,[1] Naohiro Obata, Yuh Hijikata, Stephan Irle, Qiuhong Chen and Donglin Jiang, Hydroxide Anion Conduction in Ionic Covalent Organic Frameworks, *submitted* ([1]these authors contributed equally).

3. Shanshan Tao, Hong Xu, Lipeng Zhai and Donglin Jiang, High Proton Conduction in Crystalline Covalent Organic Frameworks with Phosphoric Acid Proton Carriers, *to be submitted*.

4. Shanshan Tao, Hong Xu and Donglin Jiang, Design and Synthesis of Large Pore Covalent Organic Framework for Proton Conduction, *to be submitted*.

Presentations in Symposiums

1. Shanshan Tao, Hong Xu, Donglin Jiang. Designing Covalent Organic Frameworks as Highly Active Asymmetric Catalysts. *The international chemical congress of pacific basin societies 2015 (Pacifichem 2015), Honolulu, December 2015*, Poster Presentation

2. Shanshan Tao, Hong Xu, Donglin Jiang. Proton Conduction in Crystalline and Porous Covalent Organic Frameworks. Japan-China Joint Symposium on Functional Supramolecular Architecture @ *Okazaki, Japan*, *January 2013*, Poster Presentation.

3. Shanshan Tao, Hong Xu, Donglin Jiang. Proton Conduction in Crystalline and Porous Covalent Organic Frameworks. *96nd CSJ Annual Meeting @Kyoto, Japan*, *March 2016*, Oral Presentation

4. Shanshan Tao, Hong Xu, Donglin Jiang. Proton Conduction in Crystalline and Porous Covalent Organic Frameworks. *97nd CSJ Annual Meeting @ Yokohama, Japan*, *March 2017*, Oral Presentation

5. Shanshan Tao, Hong Xu, Donglin Jiang、High-Rate Proton Conduction in Crystalline and Porous Covalent Organic Frameworks. *66st SPSJ Annual Meeting @ Chiba*, *Japan*, *May 2017*, Oral Presentation

Acknowledgements

Times flies quickly, three years of study almost finish. I wrote my thesis with a fully thankful heart. During the past three years at IMS and JAIST, I received countless amounts of help and support from many peoples. I wish I could find a better way to express my thankfulness.

Firstly, I would like to thank my supervisors, Prof. Donglin Jiang and Prof. Hiroshi Yamamoto. Under the guidance of their advices, encouragement and help, in the three year I have learned a lot of things that cannot be obtained form class. First, the attitude, hard working and continuous thinking is the driving force of high product of the science. Previously, I have never been in an organic lab or have the chance to learn basic organic synthesis. Because the major of my master is focus on the inorganic chemistry, and these two majors have a big gap. Organic synthesis for me is a totally new field, at the first three months, Prof. Jiang guided me how to conduct organic synthesis, how to monitor and how to separate the product by chromatography. Under the guidance, now I can do the organic synthesis independently and can design the synthesis route and separate the compounds using different methods. I also learned to be careful to even small detail of experiment. From professors, I saw the attributes of being a great scientist, and learned a lot that can never be obtained. I was extremely fortunate to get the chance under their supervision. The insight, attitude, and enthusiasm have been a never-ending source of inspiration and support. Their encouragement and patience have made my time working here so enjoyable, even in difficulties and failures. I know I can never repay them for what I have received, and I hope I can pass these qualities on when I have opportunities to help others.

The interdisciplinary work presented in this thesis would have not been possible without close collaborations and interactions with experts from various fields and from different universities. In particular, the collaboration with Prof. Stephan Irle and Dr. Matthew Addicoat at Nagoya University enables the large-scale structural calculations. Their results helps me to understand the structure of the COFs. The work

in this thesis could not be completed without the assistance from the technicians at the Instrument Center in IMS and JAIST.

I also owe my sincere gratitude to my friends and my lab mates, Dr. Cheng Gu, Dr. Sasanka Dalapati, Dr. Hong Xu, Dr. Ning Huang, Dr. Yang Wu, Dr. Jia Gao, Dr. Enquan Jin, Dr. Qiuhong Chen, Dr. Yu Feng, Dr. Juan Li, Miss Ping Wang, Mr. Lipeng Zhai, Mr. Qing Xu, Mr. Zhongping Li, Mr. Chao Yang, Mr. Zhanzhao Li, Mr. Weiming Jiang, Miss Yuan Zhao, and secretary Ms. Sayuri Suzuki (IMS), for their kind help and encouragements in not only research but also everyday life. The unforgettable experience, the people and friends here in the IMS and JAIST labs and in Japan will be always in my heart.

Last but not least, I would like to thank my mother, father, brother and sister for all their love, supports and encouragements.

Shanshan TAO

2017

Appendix

Table 1 Atomistic coordinates for the AA-stacking mode of TPB-DMTP-COF optimized by using DFTB+ method (space group *P6, a* = *b* = 37.2718 Å, *c* = 3.5215 Å, $\alpha = \beta = 90°$, and $\gamma = 120°$).

Atom	x/a	y/b	z/c
C1	0.28981	0.64218	0.50948
C2	0.31459	0.62381	0.50941
C3	0.24366	0.61623	0.51129
C4	0.36807	0.58669	0.38149
C5	0.39171	0.56757	0.38659
C6	0.43264	0.5889	0.52061
C7	0.44902	0.63002	0.64034
C8	0.42488	0.64857	0.64092
N9	0.45939	0.5724	0.51985
C10	0.44488	0.53315	0.57564
C11	0.47293	0.51623	0.56578
C12	0.45731	0.47302	0.55581
C13	0.48409	0.45714	0.56395
O14	0.41445	0.44831	0.5392
C15	0.6025	0.59337	0.4059
H16	0.29983	0.59004	0.50963
H17	0.33674	0.5694	0.27378
H18	0.37848	0.53614	0.27277
H19	0.4808	0.647	0.74741
H20	0.43845	0.68015	0.75146
H21	0.41157	0.51089	0.6386
H22	0.47267	0.42382	0.57064

H23	0.58332	0.59569	0.18083
H24	0.63352	0.6031	0.2931
H25	0.60577	0.61504	0.63593

Table 2 Atomistic coordinates for the AB-stacking mode of TPB-DMTP-COF optimized by using DFTB+ method (space group *P-3, a* = *b* = 36.6669 Å, *c* = 6.3984 Å, α = β = 90°, and γ = 120°).

Atom	x/a	y/b	z/c
C1	-0.02536	1.01757	0.28511
C2	-0.04381	0.97412	0.28508
H3	-0.04557	1.03158	0.28509
C4	0.35879	0.6492	0.28354
C5	0.37713	0.69264	0.28352
H6	0.37907	0.63528	0.28346
C7	0.05285	0.96336	0.28479
C8	0.0942	0.98559	0.21462
C9	0.11954	0.96807	0.21466
C10	0.10499	0.92699	0.28403
C11	0.06336	0.90477	0.35495
C12	0.03825	0.92247	0.35504
H13	0.10686	1.01777	0.15817
H14	0.15175	0.98656	0.15776
H15	0.05064	0.87262	0.41222
H16	0.00597	0.90402	0.41211
C17	0.21689	0.79424	0.29372
N18	0.20125	0.75422	0.27727
C19	0.11587	0.87188	0.27054
N20	0.13164	0.91194	0.28544
H21	0.25122	0.81572	0.3123
H22	0.08151	0.85044	0.25343
C23	0.2803	0.70309	0.28308
C24	0.23917	0.68102	0.20965
C25	0.21384	0.69854	0.20837

C26	0.22804	0.73933	0.28129
C27	0.26945	0.7614	0.35537
C28	0.29462	0.74377	0.35583
H29	0.22676	0.64902	0.15086
H30	0.1818	0.68017	0.14896
H31	0.28198	0.79343	0.414
H32	0.32676	0.76213	0.41498
C33	0.19135	0.81387	0.28843
C34	0.14791	0.79004	0.26255
C35	0.12325	0.80502	0.25642
C36	0.14137	0.85218	0.27523
C37	0.1848	0.87596	0.30065
C38	0.20947	0.85753	0.30781
H39	0.13364	0.75607	0.24684
O40	0.07894	0.78522	0.23067
H41	0.19956	0.9101	0.31707
O42	0.25368	0.88062	0.33811
C43	0.06174	0.74011	0.22355
C44	0.27176	0.92592	0.34297
H45	0.07022	0.7287	0.36808
H46	0.0721	0.73056	0.07864
H47	0.02743	0.72616	0.21973
H48	0.2908	0.93945	0.19749
H49	0.29222	0.93804	0.48436
H50	0.24723	0.93489	0.35146

Table 3 Atomistic coordinates for the refined unit cell parameters for TPB-DMTP-COF via Pawley refinement (space group *P6, a* = *b* = 37.1541 Å, *c* = 3.5378 Å, $\alpha = \beta = 90°$, and $\gamma = 120°$).

Atom	x/a	y/b	z/c
C1	0.28981	0.64218	0.50948
C2	0.31459	0.62381	0.50941
C3	0.24366	0.61623	0.51129
C4	0.36807	0.58669	0.38149
C5	0.39171	0.56757	0.38659
C6	0.43264	0.5889	0.52061
C7	0.44902	0.63002	0.64034
C8	0.42488	0.64857	0.64092
N9	0.45939	0.5724	0.51985
C10	0.44488	0.53315	0.57564
C11	0.47293	0.51623	0.56578
C12	0.45731	0.47302	0.55581
C13	0.48409	0.45714	0.56395
O14	0.41445	0.44831	0.5392
C15	0.6025	0.59337	0.4059
H16	0.29983	0.59004	0.50963
H17	0.33674	0.5694	0.27378
H18	0.37848	0.53614	0.27277
H19	0.4808	0.647	0.74741
H20	0.43845	0.68015	0.75146
H21	0.41157	0.51089	0.6386
H22	0.47267	0.42382	0.57064
H23	0.58332	0.59569	0.18083
H24	0.63352	0.6031	0.2931
H25	0.60577	0.61504	0.63593

Table 4 Atomistic coordinates for the refined unit cell parameters for TPB-DMTP-COF via Rietveld refinement (space group *P6, a* = *b* = 36.4594 Å; *c* = 3.5239 Å, $\alpha = \beta = 90°$ and $\gamma = 120°$).

Atom	x/a	y/b	z/c
C1	0.28981	0.64218	0.50948
C2	0.31459	0.62381	0.50941
C3	0.24366	0.61623	0.51129
C4	0.36807	0.58669	0.38149
C5	0.39171	0.56757	0.38659
C6	0.43264	0.5889	0.52061
C7	0.44902	0.63002	0.64034
C8	0.42488	0.64857	0.64092
N9	0.45939	0.5724	0.51985
C10	0.44488	0.53315	0.57564
C11	0.47293	0.51623	0.56578
C12	0.45731	0.47302	0.55581
C13	0.48409	0.45714	0.56395
O14	0.41445	0.44831	0.5392
C15	0.6025	0.59337	0.4059
H16	0.29983	0.59004	0.50963
H17	0.33674	0.5694	0.27378
H18	0.37848	0.53614	0.27277
H19	0.4808	0.647	0.74741
H20	0.43845	0.68015	0.75146
H21	0.41157	0.51089	0.6386
H22	0.47267	0.42382	0.57064
H23	0.58332	0.59569	0.18083
H24	0.63352	0.6031	0.2931
H25	0.60577	0.61504	0.63593

Table 5. Atomistic coordinates for the AA-stacking mode of TPB-DMPTA-COF optimized by using $DFTB^+$ method (space group *P6*, $a = b = 36.9127$ Å, $c = 4.1241$ Å, $\alpha = \beta = 90°$, and $\gamma = 120°$).

Atom	x/a	y/b	z/c
C1	0.28976	0.64139	0.55868
C2	0.31518	0.62343	0.55861
C3	0.24365	0.61467	0.56057
C4	0.37304	0.5916	0.39498
C5	0.39771	0.57323	0.39744
C6	0.43546	0.5919	0.56888
C7	0.44834	0.62976	0.72965
C8	0.4234	0.6478	0.7269
N9	0.46243	0.57524	0.57192
C10	0.44612	0.53497	0.57207
C11	0.47306	0.51647	0.56812
C12	0.45639	0.47284	0.56762
C13	0.48356	0.45722	0.56726
H14	0.30091	0.58941	0.55889
H15	0.34391	0.57707	0.25659
H16	0.38812	0.54461	0.25932
H17	0.4777	0.64432	0.86445
H18	0.43332	0.67687	0.85963
H19	0.41162	0.51332	0.58125
H20	0.4713	0.42344	0.5676
C21	0.58995	0.55686	0.56749
H22	0.60476	0.55232	0.35371
H23	0.60478	0.55238	0.78144
H24	0.59664	0.58914	0.56721

Table 6. Atomistic coordinates for the AB-stacking mode of TPB-DMPTA-COF optimized by using DFTB+ (space group P-3, $a = b = 37.1423$ Å; $c = 6.7783$ Å, $\alpha = \beta = 90°$ and $\gamma = 120°$).

Atom	x/a	y/b	z/c
C1	-0.0243	1.01933	0.24802
C2	-0.04388	0.97556	0.24805
H3	-0.0434	1.03453	0.24838
C4	0.36068	0.6508	0.45455
C5	0.37682	0.6942	0.45425
H6	0.3822	0.63834	0.45271
C7	0.05029	0.95998	0.2507
C8	0.08931	0.97836	0.14996
C9	0.11368	0.95941	0.15587
C10	0.09927	0.92122	0.26096
C11	0.06046	0.90291	0.36412
C12	0.0363	0.92208	0.3578
H13	0.1005	1.00783	0.06419
H14	0.14392	0.97366	0.07502
H15	0.04964	0.87398	0.45383
H16	0.00633	0.90786	0.44154
C17	0.21436	0.7912	0.36616
N18	0.19737	0.75077	0.38514
C19	0.10854	0.86318	0.27576
N20	0.12578	0.90381	0.27052
H21	0.24916	0.81245	0.36229
H22	0.07386	0.84189	0.26295
C23	0.27693	0.69975	0.44525
C24	0.23925	0.67871	0.33345
C25	0.2131	0.69554	0.31651
C26	0.22455	0.73433	0.40875
C27	0.2615	0.75486	0.52697
C28	0.28736	0.73768	0.54402
H29	0.23077	0.64905	0.25522
H30	0.18416	0.67945	0.22511
H31	0.26966	0.78418	0.60792
H32	0.31607	0.75378	0.63736
C33	0.18787	0.81018	0.34359
C34	0.14421	0.78403	0.33454
C35	0.1174	0.80012	0.31127
C36	0.13491	0.84404	0.29756

C37	0.17858	0.87018	0.30695
C38	0.20539	0.8541	0.32908
H39	0.13144	0.75004	0.3459
H40	0.19133	0.90419	0.29603
C41	0.1165	0.36857	0.33823
C42	0.22925	0.29997	0.30205
H43	0.08392	0.34327	0.32483
H44	0.12274	0.39094	0.21153
H45	0.1198	0.38504	0.48548
H46	0.22577	0.28331	0.15524
H47	0.22313	0.27776	0.42934
H48	0.26185	0.32528	0.31437

Table 7. Atomistic coordinates for the refined unit cell parameters for TAPB-DMPTA-COF via Pawley refinement (space group P6, $a = b = 36.5281$ Å, $c = 3.41249$ Å, $\alpha = \beta = 90°$, and $\gamma = 120°$).

Atom	***x/a***	***y/b***	***z/c***
C1	0.29278	0.64806	0.55868
C2	0.31846	0.62991	0.55861
C3	0.24618	0.62106	0.56057
C4	0.37692	0.59776	0.39498
C5	0.40185	0.57919	0.39744
C6	0.43999	0.59806	0.56888
C7	0.453	0.63631	0.72965
C8	0.4278	0.65454	0.7269
N9	0.46724	0.58122	0.57192
C10	0.45077	0.54054	0.57207
C11	0.47798	0.52185	0.56812
C12	0.46114	0.47776	0.56762
C13	0.48859	0.46198	0.56726
H14	0.30404	0.59554	0.55889
H15	0.34749	0.58307	0.25659
H16	0.39216	0.55027	0.25932
H17	0.48267	0.65102	0.86445
H18	0.43783	0.68392	0.85963
H19	0.4159	0.51866	0.58125
H20	0.4762	0.42785	0.5676
C21	0.59609	0.56265	0.56749
H22	0.61105	0.55806	0.35371
H23	0.61107	0.55812	0.78144
H24	0.60285	0.59527	0.56721

Table 8. Atomistic coordinates for the refined unit cell parameters for TAPB-DMPTA-COF via Rietveld refinement (space group P6, $a = b = 37.64976$ Å, $c = 4.1249$ Å, $\alpha = \beta = 90°$, and $\gamma = 120°$).

Atom	***x/a***	***y/b***	***z/c***
C1	0.29302	0.6486	0.55868
C2	0.31873	0.63044	0.55861
C3	0.24639	0.62158	0.56057
C4	0.37723	0.59826	0.39498
C5	0.40218	0.57967	0.39744
C6	0.44036	0.59856	0.56888
C7	0.45338	0.63684	0.72965
C8	0.42816	0.65509	0.7269
N9	0.46763	0.58171	0.57192
C10	0.45114	0.54099	0.57207
C11	0.47838	0.52228	0.56812
C12	0.46152	0.47816	0.56762
C13	0.489	0.46236	0.56726
H14	0.30429	0.59604	0.55889
H15	0.34778	0.58356	0.25659
H16	0.39249	0.55073	0.25932
H17	0.48307	0.65157	0.86445
H18	0.4382	0.68449	0.85963
H19	0.41625	0.51909	0.58125
H20	0.4766	0.42821	0.5676
C21	0.59659	0.56312	0.56749
H22	0.61156	0.55853	0.35371
H23	0.61158	0.55859	0.78144
H24	0.60335	0.59577	0.56721

Table 9. Atomistic coordinates for the AA-stacking mode of TPB-TMDPDA-COF optimized by using DFTB+ method (Space group: *P6; a* = 44.7208 Å, *b* = 44.7208 Å, *c* = 3.8280 Å).

Atom	***x/a***	***y/b***	***z/c***
C	0.01903	0.50795	0.45631
C	0.03432	0.4893	0.32751
C	0.07036	0.50444	0.31511
C	0.09212	0.5386	0.43425
C	0.07677	0.55719	0.56553
C	0.04083	0.54217	0.57546
C	0.12973	0.55449	0.41792
N	0.14966	0.58667	0.49253
C	0.18568	0.60139	0.48715
O	0.08682	0.48718	0.18611
O	0.02444	0.55967	0.70694
H	0.14007	0.53754	0.33036
C	0.04703	0.59274	0.86421
C	0.06463	0.45398	0.02951
C	0.20212	0.58405	0.62421
C	0.23802	0.60014	0.62934
C	0.25877	0.63371	0.49543
C	0.24205	0.65082	0.35971
C	0.20622	0.63526	0.3596
C	0.29687	0.65055	0.4976
C	0.31325	0.63068	0.49773
H	0.01747	0.46314	0.22778
H	0.09401	0.5836	0.65785
H	0.06459	0.61153	0.66779
H	0.06248	0.59034	1.0765
H	0.03055	0.60227	0.97356
H	0.08141	0.44477	-0.07815
H	0.04906	0.45609	-0.18342
H	0.04716	0.43516	0.22638
H	0.18651	0.55806	0.73529
H	0.2502	0.58634	0.74464
H	0.2574	0.67685	0.24882
H	0.19375	0.64895	0.24899
H	0.29744	0.60238	0.49748

Table 10. Atomistic coordinates for the refined unit cell parameters for TPB-TMDPDA-COF via Pawley refinement. (Space group: *P6; a* = 44.4556 Å, *b* = 44.4556 Å, and *c* = 3.9215 Å).

Atom	*x/a*	*y/b*	*z/c*
C	0.01903	0.50795	0.45631
C	0.03432	0.4893	0.32751
C	0.07036	0.50444	0.31511
C	0.09212	0.5386	0.43425
C	0.07677	0.55719	0.56553
C	0.04083	0.54217	0.57546
C	0.12973	0.55449	0.41792
N	0.14966	0.58667	0.49253
C	0.18568	0.60139	0.48715
O	0.08682	0.48718	0.18611
O	0.02444	0.55967	0.70694
H	0.14007	0.53754	0.33036
C	0.04703	0.59274	0.86421
C	0.06463	0.45398	0.02951
C	0.20212	0.58405	0.62421
C	0.23802	0.60014	0.62934
C	0.25877	0.63371	0.49543
C	0.24205	0.65082	0.35971
C	0.20622	0.63526	0.3596
C	0.29687	0.65055	0.4976
C	0.31325	0.63068	0.49773
H	0.01747	0.46314	0.22778
H	0.09401	0.5836	0.65785
H	0.06459	0.61153	0.66779
H	0.06248	0.59034	1.0765
H	0.03055	0.60227	0.97356
H	0.08141	0.44477	-0.07815
H	0.04906	0.45609	-0.18342
H	0.04716	0.43516	0.22638
H	0.18651	0.55806	0.73529
H	0.2502	0.58634	0.74464
H	0.2574	0.67685	0.24882
H	0.19375	0.64895	0.24899
H	0.29744	0.60238	0.49748

Table 11. Atomistic coordinates for the AB-stacking mode of TPB-TMDPDA-COF optimized by using DFTB+ method (Space group: *P63; a* = 44.6006 Å, *b* = 44.6006 Å, and *c* = 8.1072 Å).

Atom	x/a	y/b	z/c
C	1.3525	0.17476	0.2233
C	1.36789	0.15565	0.16881
C	1.404	0.17074	0.1647
C	1.42566	0.20549	0.21428
C	1.41027	0.22462	0.26973
C	1.37427	0.20953	0.27435
C	1.46329	0.2215	0.20833
N	1.48297	0.25401	0.24016
C	1.51903	0.2688	0.24064
O	1.4207	0.15313	0.11106
O	1.35787	0.22728	0.33226
H	1.47398	0.20449	0.17213
C	1.38045	0.26147	0.39653
C	1.39852	0.11783	0.0593
C	1.5352	0.25148	0.30958
C	1.57116	0.26747	0.31362
C	1.59207	0.30091	0.24832
C	1.57565	0.31811	0.18087
C	1.53974	0.30259	0.17873
C	1.63018	0.3175	0.25016
C	1.64625	0.29726	0.25025
H	1.35113	0.12895	0.12746
H	1.42756	0.25149	0.30799
H	1.39759	0.27907	0.29905
H	1.39644	0.26075	0.499
H	1.36383	0.27137	0.44299
H	1.41543	0.10763	0.02191
H	1.38231	0.11647	-0.04691
H	1.38161	0.10188	0.16141
H	1.51936	0.22557	0.36314
H	1.58326	0.25377	0.37052
H	1.59129	0.34408	0.12759
H	1.52737	0.31623	0.12414
H	1.6302	0.26891	0.25001
C	1.3144	0.15878	0.22276

C	1.29907	0.17774	0.1651
C	1.26298	0.16268	0.16003
C	1.24124	0.12811	0.2121
C	1.25655	0.10915	0.27063
C	1.29256	0.12419	0.27588
C	1.20359	0.11212	0.20562
N	1.18393	0.07991	0.24329
C	1.14785	0.06505	0.24308
O	1.24637	0.18018	0.10337
O	1.30888	0.10655	0.33653
H	1.19297	0.12888	0.16416
C	1.28621	0.07258	0.40275
C	1.26866	0.21527	0.04937
C	1.13154	0.08328	0.29898
C	1.09558	0.0672	0.30257
C	1.07467	0.03271	0.24956
C	1.09128	0.01466	0.19518
C	1.12719	0.03029	0.19384
C	1.03653	0.01598	0.25101
C	1.02028	0.03606	0.25108
H	1.3159	0.20431	0.12205
H	1.23921	0.08242	0.31067
H	1.26908	0.05471	0.30596
H	1.27019	0.07365	0.5042
H	1.30275	0.06276	0.45111
H	1.25184	0.22542	0.0096
H	1.28494	0.21626	-0.05582
H	1.28552	0.23155	0.1509
H	1.14727	0.11005	0.34297
H	1.08356	0.08183	0.34929
H	1.07584	0.98781	0.15202
H	1.13961	0.01585	0.14981
H	1.03623	0.0644	0.2509

Table 12. Atomistic coordinates for the AA mode of $[OH^-]_{100}$-TPB-BPTA-COF optimized by using DFTB+ method (Space group: *P1; a* = 35.7312 Å, *b* = 36.1632 Å, *c* = 4.4425 Å, α = 100.275°, β = 96.694°, and γ = 59.700°).

Atom	*x/a*	*y/b*	*z/c*
C	0.5168	0.9349	0.3382
C	0.5671	0.928	0.9784
C	0.555	0.9084	0.1631
C	0.5792	0.8624	0.21
C	0.5817	0.8156	0.5452
C	0.5603	0.8084	0.7418
C	0.6232	0.7794	0.4317
C	0.5775	0.7665	0.8483
C	0.6422	0.7403	0.5539
C	0.6188	0.7318	0.7516
C	0.6387	0.6872	0.8503
C	0.6118	0.6675	0.8086
C	0.6833	0.6611	0.9308
C	0.6281	0.6246	0.8802
C	0.7006	0.6194	0.0133
C	0.6736	0.6007	0.9639
C	0.746	0.598	0.1251
C	0.7591	0.5682	0.3318
C	0.7792	0.6068	0.0602
C	0.8023	0.5465	0.4629
C	0.8227	0.5846	0.174
C	0.8357	0.5517	0.3518
C	0.5979	0.6078	0.8329
C	0.6007	0.5801	0.0333
C	0.5608	0.6233	0.6303
C	0.5718	0.5638	0.0008
C	0.5303	0.6099	0.6227
C	0.5373	0.5765	0.7833
C	0.4978	0.5465	0.4811
C	0.467	0.5275	0.431
C	0.4315	0.5396	0.2058
C	0.4748	0.4946	0.607
C	0.408	0.517	0.166
C	0.4486	0.4757	0.5785
C	0.4133	0.4882	0.3641
C	0.0114	0.4214	0.8303

C	0.0242	0.4663	0.2711
C	0.0401	0.4301	0.0308
C	0.0835	0.4112	0.9397
C	0.387	0.4664	0.3335
C	0.1492	0.3582	0.6869
C	0.1566	0.3802	0.4988
C	0.1848	0.3206	0.7907
C	0.1964	0.3612	0.3416
C	0.2245	0.3032	0.6445
C	0.2317	0.3234	0.4324
C	0.3554	0.4252	0.0878
C	0.3248	0.4329	0.2936
C	0.3712	0.3872	0.8685
C	0.3158	0.3997	0.3042
C	0.3618	0.3544	0.8763
C	0.3342	0.3602	0.1008
C	0.2751	0.3071	0.3239
C	0.2878	0.336	0.262
C	0.3041	0.2639	0.2528
C	0.3249	0.3255	0.1242
C	0.3458	0.2499	0.1287
C	0.3541	0.2804	0.0524
C	0.3751	0.2037	0.0697
C	0.4092	0.1841	0.861
C	0.3718	0.1749	0.227
C	0.4384	0.1404	0.8173
C	0.3978	0.1307	0.174
C	0.4344	0.1131	0.9852
C	0.4985	0.4202	0.9029
C	0.6242	0.9191	0.6677
C	0.3726	0.5988	0.9408
C	0.047	0.5131	0.6069
C	0.3642	0.6415	0.8574
C	0.3335	0.6832	0.9861
C	0.0817	0.5263	0.6161
C	0.0925	0.5517	0.8564
C	0.2096	0.0262	0.5736
C	0.3196	0.7529	0.8279
C	0.2744	0.8239	0.0032
C	0.3022	0.8219	0.7717
C	0.1519	0.5703	0.8092
C	0.2124	0.5783	0.7779

C	0.2809	0.9779	0.8596
C	0.3697	0.7617	0.5068
C	0.254	0.7749	0.1528
C	0.2134	0.5153	0.4302
C	0.4775	0.0461	0.1662
C	0.9022	0.5055	0.1519
C	0.5048	0.9981	0.1457
C	0.4911	0.9785	0.3288
C	0.5432	0.9727	0.9898
C	0.9503	0.4808	0.1316
C	0.9643	0.4489	0.8826
C	0.9786	0.4925	0.3293
C	0.9176	0.2213	0.305
C	0.971	0.2362	0.0993
C	0.4342	0.9869	0.6213
C	0.9428	0.4059	0.4546
C	0.3846	0.0104	0.6356
C	0.352	0.0074	0.4329
C	0.2719	0.0342	0.5732
C	0.1997	0.0604	0.4179
C	0.5275	0.3772	0.7237
C	0.5688	0.344	0.7855
C	0.9286	0.3795	0.5717
C	0.9374	0.34	0.4019
C	0.2386	0.0986	0.2787
C	0.6217	0.2735	0.4799
C	0.6706	0.2032	0.292
C	0.6871	0.2187	0.5815
C	0.7405	0.0359	0.1044
C	0.9133	0.2885	0.5082
C	0.8845	0.2454	0.5495
C	0.6722	0.2866	0.8948
C	0.8463	0.3186	0.8464
C	0.5993	0.2348	0.0106
C	0.6708	0.0473	0.8233
C	0.654	0.9337	0.8434
C	0.6654	0.9646	0.7976
C	0.1824	0.6139	0.0141
C	0.7164	0.9869	0.1145
C	0.7665	0.0084	0.3057
C	0.7726	0.9431	0.4882
C	0.1111	0.6355	0.2265

H	0.5027	0.9174	0.4114
H	0.6127	0.8391	0.1185
H	0.526	0.8339	0.8014
H	0.6387	0.7837	0.2608
H	0.5617	0.7599	0.0156
H	0.6739	0.7137	0.4716
H	0.5779	0.6904	0.7481
H	0.7045	0.6765	0.9694
H	0.6855	0.5666	0.9879
H	0.7356	0.5614	0.3924
H	0.7701	0.6307	0.9103
H	0.8119	0.5211	0.6062
H	0.8432	0.5953	0.0906
H	0.6226	0.5731	0.2369
H	0.5554	0.6476	0.4892
H	0.5751	0.5441	0.1622
H	0.503	0.62	0.4817
H	0.5035	0.5558	0.2736
H	0.5056	0.4793	0.7344
H	0.3882	0.517	0.9601
H	0.0237	0.3959	0.6323
H	0.0959	0.4342	0.0169
H	0.3819	0.4598	0.5644
H	0.1365	0.4126	0.4457
H	0.1797	0.302	0.9317
H	0.1985	0.3841	0.2137
H	0.2533	0.2773	0.7483
H	0.3093	0.4649	0.4486
H	0.3966	0.3781	0.7222
H	0.2961	0.4025	0.487
H	0.3717	0.3278	0.6945
H	0.2679	0.3686	0.3718
H	0.2978	0.2395	0.2742
H	0.3824	0.2711	0.9342
H	0.4109	0.2036	0.7043
H	0.3491	0.1873	0.4108
H	0.4638	0.1241	0.6383
H	0.3995	0.1099	0.3324
H	0.9247	0.412	0.2441
H	0.9784	0.3846	0.3831
H	0.5152	0.4384	0.9806
H	0.4937	0.4149	0.1292

H	0.4443	0.9517	0.565
H	0.4428	0.9931	0.8179
H	0.3634	0.5823	0.7573
H	0.3521	0.606	0.1343
H	0.3077	0.6905	0.1344
H	0.355	0.9834	0.2131
H	0.1971	0.0352	0.8171
H	0.2033	0.0006	0.4948
H	0.2849	0.8299	0.2505
H	0.241	0.8506	0.9954
H	0.2827	0.8318	0.5488
H	0.3131	0.844	0.8098
H	0.2082	0.5961	0.5736
H	0.2476	0.56	0.8386
H	0.2728	0.9526	0.8443
H	0.3182	0.9632	0.8562
H	0.2689	0.9984	0.0955
H	0.4001	0.7323	0.5384
H	0.3557	0.7551	0.2603
H	0.3772	0.788	0.5113
H	0.2467	0.7508	0.0358
H	0.2696	0.7675	0.3907
H	0.2222	0.8054	0.1961
H	0.2076	0.4896	0.4419
H	0.2009	0.5305	0.2047
H	0.2462	0.5054	0.434
H	0.4669	0.0633	0.4006
H	0.886	0.5155	0.9254
H	0.555	0.9912	0.8976
H	0.962	0.5229	0.4821
H	0.9575	0.3189	0.2006
H	0.9051	0.2187	0.0737
H	0.9412	0.1868	0.3415
H	0.957	0.2449	0.8683
H	0.9906	0.2484	0.1866
H	0.9916	0.2012	0.0738
H	0.6452	0.8913	0.4936
H	0.6003	0.9455	0.583
H	0.0163	0.5406	0.517
H	0.0367	0.5146	0.8375
H	0.1698	0.0909	0.484
H	0.1954	0.0504	0.1652

H	0.5908	0.3443	0.9684
H	0.6554	0.9857	0.6627
H	0.2077	0.129	0.2954
H	0.2633	0.1076	0.3431
H	0.2441	0.0849	0.0205
H	0.6731	0.1718	0.2691
H	0.6844	0.202	0.0773
H	0.7219	0.209	0.5882
H	0.6866	0.2012	0.7573
H	0.7602	0.0241	0.8938
H	0.7264	0.072	0.1809
H	0.8965	0.231	0.7753
H	0.8524	0.2485	0.4944
H	0.6554	0.3216	0.8803
H	0.6636	0.2843	0.1266
H	0.7071	0.2746	0.8977
H	0.8331	0.351	0.8003
H	0.8192	0.3123	0.7857
H	0.8578	0.3191	0.0926
H	0.5652	0.2501	0.0401
H	0.6078	0.2419	0.8055
H	0.6107	0.2007	0.9399
H	0.6832	0.031	0.5922
H	0.6399	0.0495	0.8535
H	0.6653	0.0799	0.8319
H	0.0718	0.5755	0.0441
H	0.1692	0.6487	0.9987
H	0.1985	0.6103	0.2412
H	0.7597	0.026	0.5481
H	0.8016	0.996	0.2828
H	0.8085	0.93	0.5083
H	0.7594	0.9543	0.7279
H	0.7642	0.9184	0.3843
H	0.0812	0.6358	0.144
H	0.12	0.6233	0.4482
H	0.1051	0.6698	0.2767
H	0.0993	0.2008	0.6385
H	0.1526	0.7865	0.41
H	0.5801	0.1399	0.5936
H	0.8004	0.1443	0.7048
H	0.688	0.3642	0.0949
H	0.6881	0.369	0.7316

H	0.2012	0.9156	0.7884
N	0.5627	0.8547	0.4256
N	0.5125	0.5564	0.7527
N	0.1063	0.3733	0.7812
N	0.3735	0.4522	0.0769
N	0.3368	0.7087	0.7986
N	0.1256	0.5516	0.7157
N	0.3703	0.6816	0.5811
N	0.1052	0.5149	0.3626
N	0.1322	0.5297	0.4232
N	0.1939	0.5492	0.6857
N	0.2816	0.7806	0.9551
N	0.338	0.7743	0.7285
N	0.2576	0.0077	0.6323
N	0.4632	0.0678	0.9371
N	0.881	0.5237	0.4051
N	0.938	0.2483	0.3102
N	0.3688	0.0294	0.9101
N	0.3285	0.0384	0.9142
N	0.3165	0.0249	0.6392
N	0.2389	0.0669	0.4518
N	0.5834	0.3154	0.5176
N	0.5487	0.3287	0.3021
N	0.516	0.3662	0.4209
N	0.9044	0.3875	0.8098
N	0.8991	0.355	0.8214
N	0.9194	0.3243	0.5587
N	0.6257	0.2402	0.2722
N	0.659	0.2645	0.6482
N	0.8796	0.2874	0.6299
N	0.7063	0.0243	0.0383
N	0.1441	0.6091	0.0036
N	0.6763	0.9144	0.0943
N	0.6975	0.934	0.2209
N	0.6936	0.9626	0.0378
N	0.7559	0.9733	0.2747
N	0.3827	0.642	0.6099
O	0.6079	0.9049	0.8654
O	0.0568	0.474	0.4183
O	0.4205	0.574	0.0419
O	0.4596	0.4418	0.7316
O	0.4479	0.0001	0.4025

O	0.9336	0.4452	0.6835
O	0.1225	0.1929	0.5052
O	0.1586	0.7646	0.5408
O	0.5898	0.1359	0.3825
O	0.813	0.1492	0.9143
O	0.6718	0.3841	0.9415
O	0.2203	0.9272	0.8235

Table 13. Atomistic coordinates for the refined unit cell parameters for $[OH^-]_{100}$-TPB-BPTA-COF via Pawley refinement (Space group: *P1; a* = 35.5864 Å, *b* = 36.1309 Å, *c* = 4.4624 Å, α = 88.8652°, β = 88.3074°, and γ = 61.1397°).

Atom	x/a	y/b	z/c
C	0.5168	0.9349	0.3382
C	0.5671	0.928	0.9784
C	0.555	0.9084	0.1631
C	0.5792	0.8624	0.21
C	0.5817	0.8156	0.5452
C	0.5603	0.8084	0.7418
C	0.6232	0.7794	0.4317
C	0.5775	0.7665	0.8483
C	0.6422	0.7403	0.5539
C	0.6188	0.7318	0.7516
C	0.6387	0.6872	0.8503
C	0.6118	0.6675	0.8086
C	0.6833	0.6611	0.9308
C	0.6281	0.6246	0.8802
C	0.7006	0.6194	0.0133
C	0.6736	0.6007	0.9639
C	0.746	0.598	0.1251
C	0.7591	0.5682	0.3318
C	0.7792	0.6068	0.0602
C	0.8023	0.5465	0.4629
C	0.8227	0.5846	0.174
C	0.8357	0.5517	0.3518
C	0.5979	0.6078	0.8329
C	0.6007	0.5801	0.0333
C	0.5608	0.6233	0.6303
C	0.5718	0.5638	0.0008
C	0.5303	0.6099	0.6227
C	0.5373	0.5765	0.7833
C	0.4978	0.5465	0.4811
C	0.467	0.5275	0.431
C	0.4315	0.5396	0.2058
C	0.4748	0.4946	0.607
C	0.408	0.517	0.166
C	0.4486	0.4757	0.5785
C	0.4133	0.4882	0.3641
C	0.0114	0.4214	0.8303

C	0.0242	0.4663	0.2711
C	0.0401	0.4301	0.0308
C	0.0835	0.4112	0.9397
C	0.387	0.4664	0.3335
C	0.1492	0.3582	0.6869
C	0.1566	0.3802	0.4988
C	0.1848	0.3206	0.7907
C	0.1964	0.3612	0.3416
C	0.2245	0.3032	0.6445
C	0.2317	0.3234	0.4324
C	0.3554	0.4252	0.0878
C	0.3248	0.4329	0.2936
C	0.3712	0.3872	0.8685
C	0.3158	0.3997	0.3042
C	0.3618	0.3544	0.8763
C	0.3342	0.3602	0.1008
C	0.2751	0.3071	0.3239
C	0.2878	0.336	0.262
C	0.3041	0.2639	0.2528
C	0.3249	0.3255	0.1242
C	0.3458	0.2499	0.1287
C	0.3541	0.2804	0.0524
C	0.3751	0.2037	0.0697
C	0.4092	0.1841	0.861
C	0.3718	0.1749	0.227
C	0.4384	0.1404	0.8173
C	0.3978	0.1307	0.174
C	0.4344	0.1131	0.9852
C	0.4985	0.4202	0.9029
C	0.6242	0.9191	0.6677
C	0.3726	0.5988	0.9408
C	0.047	0.5131	0.6069
C	0.3642	0.6415	0.8574
C	0.3335	0.6832	0.9861
C	0.0817	0.5263	0.6161
C	0.0925	0.5517	0.8564
C	0.2096	0.0262	0.5736
C	0.3196	0.7529	0.8279
C	0.2744	0.8239	0.0032
C	0.3022	0.8219	0.7717
C	0.1519	0.5703	0.8092
C	0.2124	0.5783	0.7779

C	0.2809	0.9779	0.8596
C	0.3697	0.7617	0.5068
C	0.254	0.7749	0.1528
C	0.2134	0.5153	0.4302
C	0.4775	0.0461	0.1662
C	0.9022	0.5055	0.1519
C	0.5048	0.9981	0.1457
C	0.4911	0.9785	0.3288
C	0.5432	0.9727	0.9898
C	0.9503	0.4808	0.1316
C	0.9643	0.4489	0.8826
C	0.9786	0.4925	0.3293
C	0.9176	0.2213	0.305
C	0.971	0.2362	0.0993
C	0.4342	0.9869	0.6213
C	0.9428	0.4059	0.4546
C	0.3846	0.0104	0.6356
C	0.352	0.0074	0.4329
C	0.2719	0.0342	0.5732
C	0.1997	0.0604	0.4179
C	0.5275	0.3772	0.7237
C	0.5688	0.344	0.7855
C	0.9286	0.3795	0.5717
C	0.9374	0.34	0.4019
C	0.2386	0.0986	0.2787
C	0.6217	0.2735	0.4799
C	0.6706	0.2032	0.292
C	0.6871	0.2187	0.5815
C	0.7405	0.0359	0.1044
C	0.9133	0.2885	0.5082
C	0.8845	0.2454	0.5495
C	0.6722	0.2866	0.8948
C	0.8463	0.3186	0.8464
C	0.5993	0.2348	0.0106
C	0.6708	0.0473	0.8233
C	0.654	0.9337	0.8434
C	0.6654	0.9646	0.7976
C	0.1824	0.6139	0.0141
C	0.7164	0.9869	0.1145
C	0.7665	0.0084	0.3057
C	0.7726	0.9431	0.4882
C	0.1111	0.6355	0.2265

H	0.5027	0.9174	0.4114
H	0.6127	0.8391	0.1185
H	0.526	0.8339	0.8014
H	0.6387	0.7837	0.2608
H	0.5617	0.7599	0.0156
H	0.6739	0.7137	0.4716
H	0.5779	0.6904	0.7481
H	0.7045	0.6765	0.9694
H	0.6855	0.5666	0.9879
H	0.7356	0.5614	0.3924
H	0.7701	0.6307	0.9103
H	0.8119	0.5211	0.6062
H	0.8432	0.5953	0.0906
H	0.6226	0.5731	0.2369
H	0.5554	0.6476	0.4892
H	0.5751	0.5441	0.1622
H	0.503	0.62	0.4817
H	0.5035	0.5558	0.2736
H	0.5056	0.4793	0.7344
H	0.3882	0.517	0.9601
H	0.0237	0.3959	0.6323
H	0.0959	0.4342	0.0169
H	0.3819	0.4598	0.5644
H	0.1365	0.4126	0.4457
H	0.1797	0.302	0.9317
H	0.1985	0.3841	0.2137
H	0.2533	0.2773	0.7483
H	0.3093	0.4649	0.4486
H	0.3966	0.3781	0.7222
H	0.2961	0.4025	0.487
H	0.3717	0.3278	0.6945
H	0.2679	0.3686	0.3718
H	0.2978	0.2395	0.2742
H	0.3824	0.2711	0.9342
H	0.4109	0.2036	0.7043
H	0.3491	0.1873	0.4108
H	0.4638	0.1241	0.6383
H	0.3995	0.1099	0.3324
H	0.9247	0.412	0.2441
H	0.9784	0.3846	0.3831
H	0.5152	0.4384	0.9806
H	0.4937	0.4149	0.1292

H	0.4443	0.9517	0.565
H	0.4428	0.9931	0.8179
H	0.3634	0.5823	0.7573
H	0.3521	0.606	0.1343
H	0.3077	0.6905	0.1344
H	0.355	0.9834	0.2131
H	0.1971	0.0352	0.8171
H	0.2033	0.0006	0.4948
H	0.2849	0.8299	0.2505
H	0.241	0.8506	0.9954
H	0.2827	0.8318	0.5488
H	0.3131	0.844	0.8098
H	0.2082	0.5961	0.5736
H	0.2476	0.56	0.8386
H	0.2728	0.9526	0.8443
H	0.3182	0.9632	0.8562
H	0.2689	0.9984	0.0955
H	0.4001	0.7323	0.5384
H	0.3557	0.7551	0.2603
H	0.3772	0.788	0.5113
H	0.2467	0.7508	0.0358
H	0.2696	0.7675	0.3907
H	0.2222	0.8054	0.1961
H	0.2076	0.4896	0.4419
H	0.2009	0.5305	0.2047
H	0.2462	0.5054	0.434
H	0.4669	0.0633	0.4006
H	0.886	0.5155	0.9254
H	0.555	0.9912	0.8976
H	0.962	0.5229	0.4821
H	0.9575	0.3189	0.2006
H	0.9051	0.2187	0.0737
H	0.9412	0.1868	0.3415
H	0.957	0.2449	0.8683
H	0.9906	0.2484	0.1866
H	0.9916	0.2012	0.0738
H	0.6452	0.8913	0.4936
H	0.6003	0.9455	0.583
H	0.0163	0.5406	0.517
H	0.0367	0.5146	0.8375
H	0.1698	0.0909	0.484
H	0.1954	0.0504	0.1652

H	0.5908	0.3443	0.9684
H	0.6554	0.9857	0.6627
H	0.2077	0.129	0.2954
H	0.2633	0.1076	0.3431
H	0.2441	0.0849	0.0205
H	0.6731	0.1718	0.2691
H	0.6844	0.202	0.0773
H	0.7219	0.209	0.5882
H	0.6866	0.2012	0.7573
H	0.7602	0.0241	0.8938
H	0.7264	0.072	0.1809
H	0.8965	0.231	0.7753
H	0.8524	0.2485	0.4944
H	0.6554	0.3216	0.8803
H	0.6636	0.2843	0.1266
H	0.7071	0.2746	0.8977
H	0.8331	0.351	0.8003
H	0.8192	0.3123	0.7857
H	0.8578	0.3191	0.0926
H	0.5652	0.2501	0.0401
H	0.6078	0.2419	0.8055
H	0.6107	0.2007	0.9399
H	0.6832	0.031	0.5922
H	0.6399	0.0495	0.8535
H	0.6653	0.0799	0.8319
H	0.0718	0.5755	0.0441
H	0.1692	0.6487	0.9987
H	0.1985	0.6103	0.2412
H	0.7597	0.026	0.5481
H	0.8016	0.996	0.2828
H	0.8085	0.93	0.5083
H	0.7594	0.9543	0.7279
H	0.7642	0.9184	0.3843
H	0.0812	0.6358	0.144
H	0.12	0.6233	0.4482
H	0.1051	0.6698	0.2767
H	0.0993	0.2008	0.6385
H	0.1526	0.7865	0.41
H	0.5801	0.1399	0.5936
H	0.8004	0.1443	0.7048
H	0.688	0.3642	0.0949
H	0.6881	0.369	0.7316

H	0.2012	0.9156	0.7884
N	0.5627	0.8547	0.4256
N	0.5125	0.5564	0.7527
N	0.1063	0.3733	0.7812
N	0.3735	0.4522	0.0769
N	0.3368	0.7087	0.7986
N	0.1256	0.5516	0.7157
N	0.3703	0.6816	0.5811
N	0.1052	0.5149	0.3626
N	0.1322	0.5297	0.4232
N	0.1939	0.5492	0.6857
N	0.2816	0.7806	0.9551
N	0.338	0.7743	0.7285
N	0.2576	0.0077	0.6323
N	0.4632	0.0678	0.9371
N	0.881	0.5237	0.4051
N	0.938	0.2483	0.3102
N	0.3688	0.0294	0.9101
N	0.3285	0.0384	0.9142
N	0.3165	0.0249	0.6392
N	0.2389	0.0669	0.4518
N	0.5834	0.3154	0.5176
N	0.5487	0.3287	0.3021
N	0.516	0.3662	0.4209
N	0.9044	0.3875	0.8098
N	0.8991	0.355	0.8214
N	0.9194	0.3243	0.5587
N	0.6257	0.2402	0.2722
N	0.659	0.2645	0.6482
N	0.8796	0.2874	0.6299
N	0.7063	0.0243	0.0383
N	0.1441	0.6091	0.0036
N	0.6763	0.9144	0.0943
N	0.6975	0.934	0.2209
N	0.6936	0.9626	0.0378
N	0.7559	0.9733	0.2747
N	0.3827	0.642	0.6099
O	0.6079	0.9049	0.8654
O	0.0568	0.474	0.4183
O	0.4205	0.574	0.0419
O	0.4596	0.4418	0.7316
O	0.4479	0.0001	0.4025

O	0.9336	0.4452	0.6835
O	0.1225	0.1929	0.5052
O	0.1586	0.7646	0.5408
O	0.5898	0.1359	0.3825
O	0.813	0.1492	0.9143
O	0.6718	0.3841	0.9415
O	0.2203	0.9272	0.8235